

NON-STOICHIOMETRIC MAGNESIUM ALUMINATE SPINEL:
MICROSTRUCTURE EVOLUTION AND
ITS EFFECT ON PROPERTIES

by

J. Aaron Miller

A thesis submitted to the Faculty and the Board of Trustees of the Colorado School of Mines in partial fulfillment of the requirements for the degree of Doctor of Philosophy (Materials Science).

Golden, Colorado

Date _____

Signed: _____

J. Aaron Miller

Signed: _____

Ivar E. Reimanis
Thesis Advisor

Golden, Colorado

Date _____

Signed: _____

Dr. Angus Rockett
Professor and Head
Department of Metallurgical and Materials Engineering

ABSTRACT

Magnesium aluminate spinel is a material of interest for transparent armor applications. Owing to its unique combination of transparency to large portions of the electromagnetic spectrum and mechanical robustness, spinel is among the front runners for applications including transparent armor windows for military vehicles and space craft windows, missile radomes, and infrared windows. However, failure in such applications may lead to severe outcomes, creating motivation to further improve the mechanical reliability of the materials used. In this thesis, potential toughening mechanisms that utilize unique control over the evolution of second phase particles are explored.

Al-rich spinel ($\text{MgO} \cdot n\text{Al}_2\text{O}_3$) with a composition of $n = 2$ is investigated. First, it is demonstrated that precipitation of second phase Al_2O_3 from single phase spinel can be achieved by modifying the densification routines typically used to produce transparent spinel. Subsequent heat treatments in air and in vacuum result in varying amounts of precipitation, demonstrating that the single phase is stabilized by the creation of oxygen vacancies during densification, and a modified defect reaction for precipitation is proposed. The location of precipitation can be varied by controlling the reintroduction of oxygen, which is beneficial for toughening specific locations of material with complex shapes, such as toughening the surface of a curved missile radome.

The fracture toughness ranges from $0.88 - 2.47 \text{ MPa}\sqrt{\text{m}}$ depending on the local microstructure. Improved toughness within precipitated regions is due to increased crack tortuosity at phase boundaries. However, precipitation from the spinel matrix causes local volume contraction, creating porosity and residual tensile stresses in regions immediately adjacent to precipitated regions. The light scatter caused by porosity is detrimental to the

transmission properties of the material, especially for precipitation layers greater than 60 μm .

The dissolution of second phase Al_2O_3 particles into a stoichiometric spinel matrix is also investigated. Complete dissolution of all Al_2O_3 demonstrates the capability to control the size of the second phase particles, limiting light scatter at phase boundaries. Furthermore, dissolution results in compressive, rather than tensile, stresses within the composite material. A maximum toughness of 4.34 $\text{MPa}\sqrt{\text{m}}$ was measured in the two-phase composite compared to 2.26 $\text{MPa}\sqrt{\text{m}}$ once complete dissolution had occurred. However, the toughness of the dissolved specimen is still an improvement from 1.72 $\text{MPa}\sqrt{\text{m}}$ measured for single-phase, Al-rich spinel of the same overall composition as densified by traditional methods. The observed enhancement in toughness is attributed to a combination of residual stresses that arise from the coefficient of thermal expansion mismatch between particle and matrix, crack deflection caused by second phase particles, and the volume expansion as Al_2O_3 dissolves into the spinel matrix.

TABLE OF CONTENTS

ABSTRACT.....	iii
LIST OF FIGURES	ix
LIST OF TABLES.....	xv
ACKNOWLEDGEMENTS	xvi
CHAPTER 1 INTRODUCTION	1
1.1 Thesis outline	2
1.2 Research Statement	4
CHAPTER 2 BACKGROUND AND LITERATURE REVIEW	5
2.1 Potential materials for transparent armor applications	5
2.2 Properties of spinel	8
2.3 Fracture mechanics of brittle materials.....	12
2.3.1 Modes of crack loading.....	12
2.3.2 R-Curve Behavior	13
2.4 Second phase toughening in ceramics	14
2.4.1 Transformation toughening.....	15
2.4.2 Crack bridging	15
2.4.3 Crack bowing	16
2.4.4 Crack deflection	17
2.4.5 Second phase particles and light scattering	20
2.5 Structure of constituent phases	21
2.6 Microstructural evolution.....	23
2.6.1 Precipitation	24
2.6.2 Nucleation and rate limiting mechanisms	24
2.6.3 Dissolution	26

2.7	Proposed scope of research	28
2.8	References	29
CHAPTER 3	DIFFUSION LIMITED PRECIPITATION OF ALUMINA IN MAGNESIUM ALUMINATE SPINEL	36
3.1	Abstract	36
3.2	Introduction	36
3.3	Experimental procedure	38
3.4	Results	41
3.5	Discussion	44
3.6	Conclusions	50
3.7	Acknowledgements	51
3.8	References	51
CHAPTER 4	MECHANICAL AND OPTICAL PROPERTIES IN PRECIPITATED REGIONS OF ALUMINA-RICH MAGNESIUM ALUMINATE SPINEL	54
4.1	Abstract	54
4.2	Introduction	55
4.3	Experimental procedure	58
4.4	Results and discussion	61
	4.4.1 Precipitation	61
	4.4.2 Mechanical properties	63
	4.4.3 Optical properties	70
4.5	Conclusions	71
4.6	Acknowledgements	72
4.7	References	72

CHAPTER 5	ENHANCED FRACTURE TOUGHNESS IN NON-STOICHIOMETRIC MAGNESIUM ALUMINATE SPINEL THROUGH CONTROLLED DISSOLUTION OF SECOND PHASE ALUMINA.....	77
5.1	Abstract	77
5.2	Introduction.....	78
5.3	Experimental procedure	79
5.4	Results and discussion	81
	5.4.1 Structural evolution.....	81
	5.4.2 Mechanical properties.....	88
5.5	Conclusions.....	93
5.6	Acknowledgements.....	94
5.7	References.....	94
CHAPTER 6	SUMMARY AND CONCLUSIONS	98
6.1	Toughened magnesium aluminate spinel.....	100
6.2	Controlled evolution of second phase particles	100
6.3	Future research.....	101
	6.3.1 Varied processing conditions.....	101
	6.3.2 Controlling impurities and porosity	103
APPENDIX A	THEORETICAL DENSITY OF AL-RICH MAGNESIUM ALUMINATE SPINEL	105
	A.1 Lattice parameters.....	105
	A.2 Unit cells of constituent phases.....	106
	A.3 Molecular volumes and theoretical densities	107
	A.4 References.....	108
APPENDIX B	INDENTATION DATA	109

B.1 Precipitation of Al_2O_3	109
B.2 Dissolution of Al_2O_3	123

LIST OF FIGURES

Figure 2.1	Transmission windows of various materials are shown, listing the cutoff edge due to electron excitation (lower bound) and lattice vibrations (upper bound). The cutoff edge is approximate, and is defined as the wavelength at which transmission drops below 10% for a specimen that is 2 mm thick. Adapted from Harris ² with supplemental information ³⁻⁵	6
Figure 2.2	Reported hardness values for single phase magnesium aluminate spinel of various compositions are shown.	10
Figure 2.3	Reported fracture toughness values for single phase magnesium aluminate spinel of various compositions are shown.	10
Figure 2.4	Loading modes for a half penny crack are shown. Mode I (left) demonstrates uniaxial tension, or crack opening. Mode II (middle) demonstrates in-plane shear loading, and mode III (right) demonstrates out-of-plane shearing, or tearing. The white and dark circles represent a loading direction into the page and out of the page, respectively.....	13
Figure 2.5	Transformation toughening is shown. The opening of the propagating crack introduces a stress to the dispersed metastable particles. The stress induces a phase transformation, resulting in a volume expansion that introduces compressive stresses which act to close the crack.	15
Figure 2.6	Crack bridging is shown. For further crack opening to occur, the traction forces between the fibers and the matrix must be overcome. This debonding increases energy dissipation until the fiber breaks. The unbroken fibers in the wake of the crack constitute the active bridging zone.	16
Figure 2.7	Crack bowing is shown where the arrow indicates the direction of propagation (the crack wake is shown in grey). As the front encounters second phase particles, it is pinned. Further propagation causes the front to curve outward, increasing the length of the active front and therefore increasing the rate of energy dissipation.....	17
Figure 2.8	Crack deflection at interfacial layers is shown. Propagation is initially due to mode I loading, but is redirected into a mixed loading condition.	18
Figure 2.9	Crack deflection at second phase particles is shown where the arrow indicates the direction of propagation. Similar to Figure 2.8, the crack is redirected, resulting in mixed loading modes.....	18

Figure 2.10	Crack deflection due to residual stresses is illustrated for the case when the thermal expansion coefficient of the second phase particle is greater than that for the matrix ($\alpha_p > \alpha_m$). During cooling, the particle shrinks faster than the surrounding matrix, resulting in radial tensile stress and compressive tangential (hoop) stress in the matrix. The propagating crack is first deflected away by compressive stresses, then attracted by tensile stresses.	19
Figure 2.11	Conventional unit cells for are shown for α -Al ₂ O ₃ (top), stoichiometric, n = 1 spinel (middle), and Al-rich, n = 2 spinel (bottom). The left column is the cell as viewed down [001] and the right column is an off-axis view (approximately [1, -0.15, -0.25]). The red, grey, and orange colors denote the site fractions of O, Al, and Mg ions, respectively. White in the n = 2 structure denotes the site fraction of vacancies, as evident in the mixed tetrahedral sites. These structures were created using VESTA Visualization Software (Ver. 3.3.2)	22
Figure 2.12	The MgO-Al ₂ O ₃ phase diagram is shown ⁶⁷	23
Figure 2.13	Precipitation of Al ₂ O ₃ at a grain boundary in polycrystalline spinel is shown schematically	26
Figure 3.1	A spinel test specimen on high purity Al ₂ O ₃ kiln furniture used for heat treatments is shown. The bottom and end surface of the specimen were in intimate contact with the furniture, while the remaining surfaces are exposed to the atmosphere of the furnace. These are referred to as covered and exposed surfaces, respectively (A). Post heat treatment the specimen was cross sectioned perpendicular to the top and bottom and polished to reveal the depth of Al ₂ O ₃ precipitation where arrows indicated the direction of material removal (B).	40
Figure 3.2	XRD spectra for n = 2 material after hot pressing, HIPing, and heat treating for 10 hours in air are shown. After hot pressing and HIPing, only spinel (S) was present. The heat treatment led to the appearance of α -Al ₂ O ₃ peaks (a).	41
Figure 3.3	SEM and corresponding EDS mapping of Al, Mg, and O is shown for a cross section of n = 2 material heat treated for 10 hours in air. The right side is the surface that was exposed to air. A growth front of Al ₂ O ₃ is apparent.	42

Figure 3.4	Optical micrographs showing the progression of precipitation of α -Al ₂ O ₃ from the surface inwards in n = 2 spinel during heat treatment in air are shown. Isolated surface precipitation was first observed after heat treating for 5 hours. After 20 hours, a uniform precipitation front had reached a depth of approximately 820 μ m.43	43
Figure 3.5	Optical micrographs showing the progression of precipitation of α -Al ₂ O ₃ from the surface in towards the bulk in n = 2 spinel during heat treatment in vacuum are shown. After 20 hours, the precipitation front had reached a depth of approximately 120 μ m. Note that the magnification is increased when compared to Figure 3.4 to better show the precipitated region.43	43
Figure 3.6	The depth of the Al ₂ O ₃ precipitation front in n = 2 material from various surfaces is shown as a function of heat treatment time and atmosphere. Precipitation appeared to follow a linear trend with time after a uniform surface layer was developed after 10 hours heat treatment. The as-HIPed material is shown as 0 hours heat treatment. Covered surface refers to the faces of the specimen in direct contact with the kiln furniture, while exposed surface refers to the faces of the specimen open to the atmosphere of the heat treatment.44	44
Figure 3.7	Polished cross sections of two specimens are shown. Material that was HIPed, then heat treated in air at 1573 K for 10 hours (left) is compared to material that was HIPed, then heat treated in air at 1873 K for 24 hours, then heat treated in vacuum at 1573 K for 10 hours (right), demonstrating that precipitation can occur at the surface or at the core depending on processing conditions.45	45
Figure 3.8	SEM micrograph of precipitated region displaying porosity formed as a result of volume contraction during precipitation. This porosity and enhanced disorder at phase boundaries help to explain the rapid diffusion and linear trend observed in the advancement of the precipitation front.48	48
Figure 4.1	Experimental hardness values for single phase magnesium aluminate spinel are shown for varied compositions. Values from Vickers hardness are shown in black while other techniques are shown in grey.56	56
Figure 4.2	Experimental toughness values for single phase magnesium aluminate spinel are shown for varied compositions. Values from indentation toughness are shown in black while other techniques are shown in grey.56	56

Figure 4.3	The MgO-Al ₂ O ₃ phase diagram is shown with vertical lines marked A and B to denote stoichiometric (n = 1) and Al-rich (n = 2) compositions, respectively. The intersection of these lines with the horizontal dotted lines show the thermodynamically favored phases for each composition at the hot pressing, hot isostatic pressing, and heat treatment temperatures used in this study.....	59
Figure 4.4	A polished cross section of n = 2 spinel after 15 hours of heat treatment in air is shown, illustrating the advance of the Al ₂ O ₃ precipitation front from the surface shown at right (Top). Higher magnification reveals that porosity forms at spinel-Al ₂ O ₃ phase boundaries to compensate for the volume contraction that occurs when Al ₂ O ₃ precipitates (Bottom).....	62
Figure 4.5	A Vickers indent in the spinel matrix just beyond the precipitation front after 20 hours (Top) is compared to an indent made within the precipitated region after 20 hours (Middle) and an indent made in the as-HIPed material (Bottom) where the emanating cracks are enhanced in white. Compared to the indent in the as-HIPed specimen, the cracks did not propagate as far in the precipitated region. However, longer cracks were observed in the single-phase region immediately preceding the precipitation front.....	64
Figure 4.6	SEM micrographs of cracks created from Vickers indents within the matrix (Top) and precipitated region (Bottom) are shown, revealing that second phase Al ₂ O ₃ precipitates greatly enhanced crack tortuosity. In both cases, the indent is out of view to the left of the image.	66
Figure 4.7	Vickers hardness under 100gf load is shown for n = 2 spinel heat treated for 10 hours where the leading edge of the precipitation front is designated as the origin for the x-axis. The 3 regions of different hardness values are shown where the average and standard deviation is shown as solid and dashed lines, respectively.....	68
Figure 4.8	Hardness measured by nanoindentation is overlaid onto the specimen from which it was measured. Black dots represent the location of the indent, each spaced 50 μm from other indents. The lowest hardness measured occurred in material immediately adjacent to the precipitation front.	69
Figure 4.9	FTIR transmission spectra for n = 2 spinel heat treated in air for 5, 10, 15, and 20 hours is shown. Transmission decreases with increasing heat treatment time as the thickness of the precipitation front and the amount of porosity increases.....	71

Figure 5.1	XRD patterns of α -Al ₂ O ₃ and γ -Al ₂ O ₃ powders mixed with stoichiometric (n = 1) spinel powder are shown. For reference, pure n = 1 powder is also shown where all peaks are identified as spinel (S). Because of the lack of crystallinity in the starting powder, γ -Al ₂ O ₃ peaks (γ) at 39.34, 45.36, and 66.62 deg. (inset) were overwhelmed when mixed with spinel powder, while peaks from α -Al ₂ O ₃ (α) were clearly identifiable when mixed.....	82
Figure 5.2	XRD patterns are shown for powders hot pressed for 5 hours at 1600°C. Regardless of whether α -Al ₂ O ₃ or γ -Al ₂ O ₃ powder was mixed with n = 1 powder, all peaks were identified as spinel (S) or α -Al ₂ O ₃ (α) post hot pressing.	83
Figure 5.3	XRD patterns are shown for various hot pressing temperatures. In all cases, α -Al ₂ O ₃ and stoichiometric (n = 1) spinel powders were mixed to form an overall composition of MgO•2Al ₂ O ₃	83
Figure 5.4	XRD patterns from Figure 5.3 are shown from 34° to 38°, showing the 104 α -Al ₂ O ₃ peak at approximately 35° and the 311 spinel peak at approximately 37°. With the exception of the specimen heat treated at 1600°C for 10 hours, all patterns show that both peaks shift to the right with increased hot pressing, indicating a decrease in lattice parameter.....	84
Figure 5.5	Polished surfaces are shown for α -Al ₂ O ₃ .spinel hot pressed at 1600°C for 5, 10, 20, and 30 hours (A-D), 1650°C for 10 hours (E), and 1700°C for 10 hours (F). γ -Al ₂ O ₃ -spinel hot pressed at 1600°C for 5 hours is also shown (G).....	86
Figure 5.6	SEM and corresponding energy dispersive spectroscopy mapping of Al, Mg, O, and C is shown for α -Al ₂ O ₃ .spinel powders hot pressed at 1650°C for 10 hours. Lack of Mg and increased concentration of Al signifies an Al ₂ O ₃ particle within the spinel matrix. During hot pressing, C from the die diffuses into the material where it is concentrated at the interface between the two phases.....	87
Figure 5.7	SEM and corresponding energy dispersive spectroscopy mapping of Al, Mg, O, and C is shown for α -Al ₂ O ₃ .spinel powders hot pressed at 1700°C for 10 hours. All second phase Al ₂ O ₃ has dissolved into the spinel matrix, but residual C at internal pores remains where second phase particles once were.....	87
Figure 5.8	Scanning electron micrographs of lighter Al ₂ O ₃ particles within a dark spinel matrix are shown for material hot pressed at 1600°C for 5 (left), 20 (middle), and 30 (right) hours.	87

Figure 5.9	Vickers indents are shown in material hot pressed at 1600°C for 5, 10, 20, and 30 hours (A-D), 1650°C for 10 hours (E), and 1700°C for 10 hours (F). γ -Al ₂ O ₃ -spinel hot pressed at 1600°C for 5 hours is also shown (G). Images are enhanced to show cracks from indentation in white.89	89
Figure 5.10	The measured indentation toughness is shown as a function of the mean free path between second phase Al ₂ O ₃ particles. Combined CTE mismatch and crack deflection mechanisms are expected to produce toughness values modeled by the solid line.89	89
Figure 5.11	Black Al ₂ O ₃ particles are shown dissolving into the spinel matrix, creating grey regions of Al-rich spinel (left). Continued dissolution results in smaller particles spread farther apart (middle), until complete dissolution and a uniform stoichiometry and stress distribution is achieved (right). The dissipation of stress concentrations results in increased crack propagation and lower fracture toughness.93	93
Figure 6.1	The varied microstructures possible through precipitation of Al ₂ O ₃ are shown schematically. Oxygen vacancies are present after HIPing in reducing environments, stabilizing the single phase structure. Heat treatment in vacuum will not result in precipitation. Heat treatment in air below the solvus temperature promotes precipitation as oxygen diffuses from the atmosphere into the surface. Heat treatment in air above the solvus temperature also results in diffusion of oxygen and restores oxygen vacancies, but no precipitation occurs. Subsequent heat treatment of this restored structure will result in uniform precipitation if the material is heat treated in air. If the material is heat treated in vacuum instead, oxygen vacancies are again created at the surface, stabilizing the single phase spinel as precipitation occurs in the bulk.102	102

LIST OF TABLES

Table 2-1	Knoop hardness and fracture toughness are shown for materials possessing a transmission window acceptable for both transparent armor and missile radome applications. Values here are reported by Harris.	7
Table 4-1	The Indentation toughness and Chevron notch toughness of n = 2 spinel as-HIPed and after 1 hour of heat treatment is compared.	63
Table 4-2	The indentation toughness of spinel is summarized for varied compositions and processing conditions. The single-phase matrix and precipitated region of the material heat treated for 20 hours correspond to Region II and Region I, respectively, in Figure 4.7 All indents for all specimens were performed under ambient lab conditions (21°C, 50% relative humidity).	67
Table 5-1	The particle size and purities of the starting powders is summarized.	79
Table 5-2	The vol. % Al ₂ O ₃ , mean free path between particles, measured indentation toughness, and calculated residual compressive stresses are summarized for hot pressing times and temperatures investigated. The mean free path for material hot pressed at 1700°C is the distance between carbon concentrations, as no Al ₂ O ₃ was observed. The calculated residual compressive stress is determined after contributions from the Taya and Faber & Evans models have been subtracted	86
Table B-1	All measurements of indents used to calculate indentation fracture toughness during the precipitation study are shown.	109
Table B-2	Hardness values determined using a load of 1 kgf are shown for each hot pressing routine investigated. These values were used to calculate the indentation toughness for an applied load of 3 kgf.	123
Table B-3	All measurements of indents used to calculate indentation fracture toughness during the dissolution study are shown.	123

ACKNOWLEDGEMENTS

It's funny how the acknowledgements section is left until the very end of the writing process when so many of the thoughts contained within are known from the very beginning. Before any papers were accepted and published, before any meaningful data was collected, before I even really knew what questions I was trying to answer, I knew most of the names that would be found within these pages.

I would like to thank my parents for supporting my many interests from the beginning. You dared me to try new things, to pursue my talents, and to learn from failure. Without your never-ending encouragement, there would be no thesis to contain this acknowledgement section. To my older sister, Audrey, thank you for showing me there is value in forging your own path and becoming your own person. To my younger brother, Austin, thank you for reminding me that the destination isn't always as important as having fun along the way. To my wife, Heidi, thank you so much for your love and support throughout this endeavor. I would not have had the confidence to start this thesis, nor the sanity to finish it, without you as my anchor.

To the swim team at Mines, thank you for showing me that truly anything is possible through hard work and a strong support network. To the water polo team, thank you for making it fun to compete again. Most of all, thank you to both of these groups for forcing me to take time away from school to pursue my other passions.

I would also like to thank the students in our research group, past and present. Thank you Badri, Subra, and Amy, for setting a standard of excellence to be followed, and for your willingness to drop everything to answer my questions. Thank you, Ivar, for your support from day one; your confidence in me and this project was instrumental, especially during the times

when I did not have that confidence in myself. To the next generation of students in the group; I wish you the best of luck!

Adam, Fritz, and Yachao; thank you for deciding to come to Mines for your PhD degree. It was privilege to start the program with you, even if it did mean taking kinetics, thermo, and bonding all the first semester. Thank you, Mike Sanders, for showing me that you must eat wings at least once a week in order to be productive. Thank you to my office mates, Deborah, Dan, Stephan, and Chuan Chen, for being human beings. Conversations with you throughout the day made the long nights and early mornings bearable.

I know there are more people that deserve to be mentioned here. I have been very fortunate to have so many positive influences in my life, and I am grateful to all of you.

CHAPTER 1

INTRODUCTION

The ability to transmit or receive electromagnetic signals through a protective barrier is paramount to many aspects of modern technology. Conventional materials may satisfy this requirement for many applications; for example, traditional window glass transmits visible light while shielding from moderate temperature changes, and polymer covers can protect infrared or radio antennas from modest impacts or other environmental hazards without disrupting incoming or outgoing signals. However, more extreme environments require the development of new materials that can adequately protect people and equipment without disrupting such signals. This is of particular interest for certain defense applications because communication and information processing are critical and must often occur in harsh environments where signal loss is not tolerable; missile radomes and transparent armor for vehicles are two examples.

For missile radomes, it is critical that the dome protects the sensitive guidance equipment from factors such as rapid heating at the time of firing or long term damage incurred from water or dust particulates during routine flight as the missile is stored beneath the aircraft wing. In addition, the radome must be transparent to the infrared signal of a target exhaust signature. In the case of transparent armor for military vehicle windows, an acceptable material must be able to withstand high energy impacts from projectiles. The window must also be fully transparent to the visible portion of the electromagnetic spectrum so as not to obstruct the view the driver or passengers.

Magnesium aluminate spinel is a material that shows great potential for these applications because of its unique combination of properties. It is transparent to a large portion of the electromagnetic spectrum, chemically inert, thermally stable, and mechanically robust. Spinel is

also attractive because it is possible to produce shaped parts from powders composed of relatively inexpensive magnesia and alumina precursors. While this combination makes spinel an attractive option, further improvements to the material are still desirable. One particular area of interest to the scientific community, and the focus of this thesis, is in further enhancing the mechanical properties of spinel, particularly for windows and domes.

In traditional ceramic systems, the mechanical properties can be altered by modifying the microstructure through techniques such as fiber reinforcement, grain texturing, transformation toughening, or creating multilayer composites. However, these structural alterations cause light scattering, rendering the material opaque and unusable for transmission applications. Therefore, an innovative processing technique is needed in order to introduce toughening mechanisms to transparent materials without altering the optical properties. The work presented in this thesis explores the structural evolution of second phase Al_2O_3 within an Al-rich spinel matrix in order to create a two-phase material that is more mechanically robust, yet still transparent. This system is of particular interest because of the wide range of solubility of Al_2O_3 within spinel; a characteristic that can be controlled by altering conditions during densification and subsequent heat treatments.

1.1 Thesis outline

The body of this thesis contains six chapters, as follows:

- Chapter 2 is a literature review covering research pertinent to this thesis. The current state of research regarding magnesium aluminate spinel for transparent armor is presented and the shortcomings of existing technology are discussed. Toughening mechanisms employed in other material systems are explored. The kinetics of

precipitation and dissolution of non-stoichiometric spinel are then presented, illuminating the unique control over second phase evolution that might lead to toughening spinel with minimal loss to transparency.

- Chapter 3 explores the feasibility of controlling precipitation of second phase Al_2O_3 from Al-rich spinel utilizing temperatures and oxygen partial pressures achievable in industrial processing. The stability of single phase, non-stoichiometric spinel and the precipitation of Al_2O_3 from said spinel are investigated and results are discussed. This chapter is modified from a paper published in the Journal of the American Ceramic Society and is reproduced here with permission.
- Chapter 4 investigates the mechanical and optical properties resulting from the precipitation experiments discussed in Chapter 3, demonstrating that toughness is increased where precipitation is permitted. It was also discovered that residual tensile regions are formed immediately adjacent to precipitated regions as a result of volume contraction during precipitation, and the implications are discussed. This chapter has been published in The International Journal of Applied Ceramic Technology and is reproduced here with permission.
- Chapter 5 investigates mechanical properties that can be achieved if second phase Al_2O_3 is dissolved into spinel, rather than precipitated out as explored in Chapters 3 and 4. Instead of residual tensile stresses, residual compressive stresses are observed, leading to substantial increase in toughness. Existing models do not explain the enhanced toughness observed, and the implications are discussed. This chapter has been submitted to The Journal of the American Ceramic Society for publication.
- Chapter 6 summarizes the scientific contributions made in the previous chapters and ties

the individual papers together through overarching conclusions for the thesis. New questions that have been brought to light through this research are also discussed. While initial results indicate that greater toughness can be achieved, refinement of the processing technique is needed to repeatedly produce material with acceptable transparency. Potential solutions are explored.

- Appendix A provides calculations used to determine the theoretical density of non-stoichiometric spinel derived from the defect reactions proposed in literature.
- Appendix B includes experimental data collected to determine the indentation fracture toughness discussed in chapters 4 and 5.

1.2 Research Statement

The research presented in this thesis is the result of a collaborative effort, and the individuals involved deserve recognition for their contributions. J. Aaron Miller was the primary author and researcher in charge of conducting experiments and analysis. Professor Ivar E. Reimanis guided the design of the experiments, assisted with data analysis, and provided invaluable insight during the editing and publishing process of each chapter. He is also the author for correspondence for the papers presented in chapters 3, 4, and 5. Weigo Mia assisted with interpretation of the results presented in chapters 3, 4, and 5. Anthony C. Sutorik synthesized the materials investigated in chapters 3 and 4 and assisted with interpreting the results observed in these chapters. Jonathan A. Salem assisted with Chevron notch toughness measurements presented in chapter 4. Discussions with Marc Rubat du Merac led to the Reitveld refinement work that confirmed the presence of compressive stresses discussed in chapter 5. Marc also provided assistance in interpretation of the XRD data and editing the manuscript submitted for publication.

CHAPTER 2

BACKGROUND AND LITERATURE REVIEW

Transparent magnesium aluminate spinel was first developed in 1960¹ and has been a material of interest for many applications ever since. Much research has been conducted over the last several decades, leading to a comprehensive literature base. This chapter summarizes much of the previous literature, starting with a review of candidate materials for transparent armor applications. Next, the mechanical and optical properties for spinel will be presented. While these previous works illustrate why spinel has been the material of choice for niche applications, they also highlight where further improvements are needed. In particular, previous literature indicates that further improvement of the mechanical properties, namely fracture toughness, is desirable. After a brief review of fracture mechanics pertinent to understanding toughness in brittle materials, the following section this chapter will explore potential toughening mechanisms that have been successful in non-transparent ceramic systems. Finally, studies of the structural evolution of non-stoichiometric spinel will provide evidence on how such mechanisms might be employed in the spinel system to improve toughness without detracting from transparency.

2.1 Potential materials for transparent armor applications

A wide variety of material systems have been considered for transparent armor applications. At a minimum, the material under consideration must demonstrate a combination of high transparency and mechanical robustness, but natural abundance, ease of manufacturing, and process scalability are also important considerations. Starting with the requirement of transparency, Harris² has summarized a list of numerous optical materials which has been

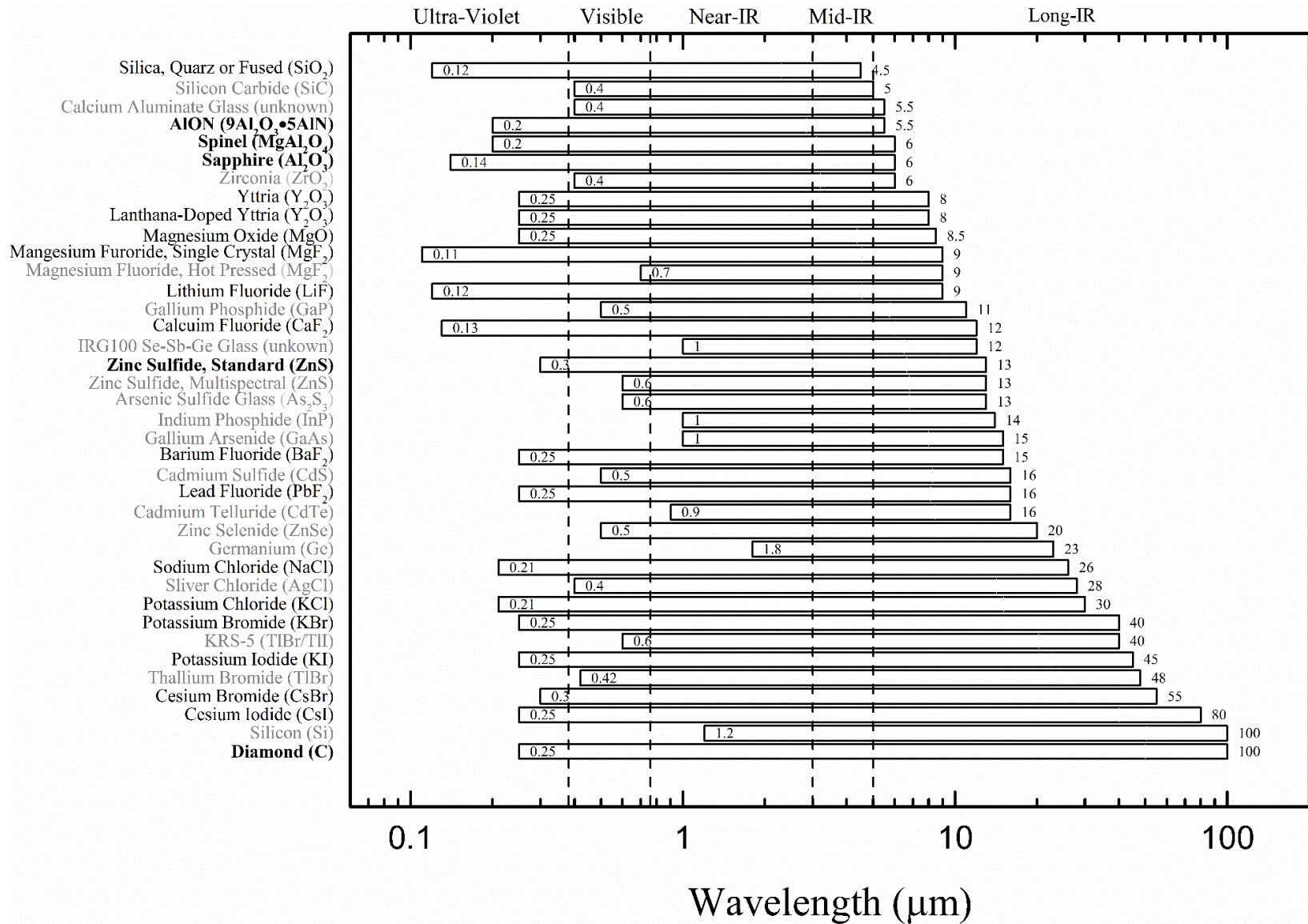


Figure 2.1. Transmission windows of various materials are shown, listing the cutoff edge due to electron excitation (lower bound) and lattice vibrations (upper bound). The cutoff edge is approximate, and is defined as the wavelength at which transmission drops below 10% for a specimen that is 2 mm thick. Adapted from Harris² with supplemental information³⁻⁵.

reproduced in Figure 2.1. For transparent armor applications, transmission through the entire portion of the visible spectrum is needed, while missile radomes require high transmission at wavelengths typical of target exhaust signatures (approximately 4.8 μm). A single material with a transmission window from the edge of the ultraviolet spectrum through the majority the mid-infrared spectrum (0.38 – 5 μm) could therefore satisfy both applications. Materials in Figure 2.1 that do not possess such a transmission window are shown in grey, revealing that there is still a substantial amount of potential materials to choose from. As mentioned earlier, mechanical properties are also a necessity for the above applications, so materials that possess an acceptable transmission window as well as a fracture toughness greater than 1.0 $\text{MPa}\sqrt{\text{m}}$ are shown in bold. This shortened list contains materials that demonstrate the greatest potential for window and dome applications and include Sapphire, AlON, magnesium aluminate spinel, zinc sulfide, and diamond. The fracture toughness and Knoop hardness of these materials, according to Harris, is shown in Table 2-1.

Table 2-1 Knoop hardness and fracture toughness are shown for materials possessing a transmission window acceptable for both transparent armor and missile radome applications. Values here are reported by Harris.

Material	Knoop Hardness (GPa)	Toughness ($\text{MPa}\sqrt{\text{m}}$)
AlON	180	1.4
Spinel	160	1.9
Sapphire	220	2.0
Zinc Sulfide	25	1.0
Diamond (Single Crystal)	880	3.4

Al_2O_3 has demonstrated excellent mechanical properties^{6,7} and can be transparent⁸, but the hexagonal crystal structure causes birefringence at grain boundaries^{2,9}. The use of single crystal material (sapphire) eliminates the problem with grain boundaries, but costs are increased because pieces must be cut and polished from single crystal boules¹⁰. Birefringence can be

reduced in polycrystalline Al_2O_3 if the grains are at least an order of magnitude smaller in size than the wavelength of interest because the wavelength is effectively too large to interact with single boundaries^{2, 6, 11}. However, this implies that grains sizes must be less than 30 nm to be transparent to a large portion of the visible spectrum, and maintaining such small grains while producing a completely dense material has proven to be complicated^{6, 11}. Cubic aluminum oxynitride (AlON) does not suffer from optical birefringence and has also demonstrated acceptable mechanical properties for armor applications¹², but has a lower infrared absorption edge than either sapphire or spinel and lower in-line transmission (ILT) at wavelengths of interest for missile radome applications². Similarly, transparent zinc sulfide^{2, 13} (and other non-oxides such as silicon nitride¹⁴ and silicon carbide¹⁵) have been produced, but demonstrate low ILT through the visible portion of the spectrum. While diamond exhibits excellent mechanical properties and the widest transmission window of all materials considered, the cost of attaining and machining pieces for even the smallest dimensions is impractical. It should also be mentioned that a composite material not included in the figure above, $\text{MgO}\cdot\text{Y}_2\text{O}_3$, has shown great potential because high transmission is retained¹⁶ while the separate phases greatly improve the mechanical properties by preventing grain growth due to pinning¹⁷⁻¹⁹. However, access to Y_2O_3 ultimately limits the possibility of industrial scale production of such a composite.

2.2 Properties of spinel

Magnesium aluminate spinel has the optimal combination of properties compared to the other materials considered thus far. The cubic structure of spinel²⁰ eliminates the problem of birefringence in polycrystalline material. Furthermore, relatively inexpensive powders can be used to form parts near net shape²¹, which provides the best chance for a scalable manufacturing process²². Spinel also demonstrates high ILT, approximately 75-85%, for wavelengths of 0.2 –

5.5 $\mu\text{m}^{1, 2, 23}$ (Figure 2.1). Reported hardness values^{24–26} for stoichiometric spinel, up to 15.2 GPa, are as high as any other candidate material, but toughness values range from 1.1 to 2.2 $\text{MPa}\sqrt{\text{m}}$ and improvement is desirable¹³. Varying the stoichiometry has resulted in both superior and inferior mechanical performance, as summarized in Figure 2.2 and Figure 2.3^{23, 24, 26–33} and discussed below.

Often written as $\text{MgO}\cdot n\text{Al}_2\text{O}_3$, single phase polycrystalline spinel has been synthesized with compositions ranging from $n = 0.80$ (Mg-rich) to $n = 3.05$ (Al-rich)³⁴ and single crystals of compositions up to $n = 3.5$ have been investigated^{35, 36}. Improved mechanical performance with varied stoichiometry has been observed in other material systems due to imposed lattice strains as larger substitute ions are incorporated into the matrix structure^{37–39}. Work by Huang³⁰ demonstrated that Vickers hardness increased from approximately 90 to 110 GPa and indentation fracture toughness increased from 2.22 to 2.54 $\text{MPa}\sqrt{\text{m}}$ as the composition increased from $n = 1$ (stoichiometric) to $n = 1.8$ (Figure 2.2 and Figure 2.3). The improved properties are attributed to formation of second phase Al_2O_3 during cooling post densification, but no quantitative correlation to the second phase is attempted, nor any demonstration that a uniform single phase was achieved for the stoichiometric control specimen.

Works by Sutorik^{25, 26, 28} concluded that Knoop hardness (measured at load of 2 kgf) was independent of stoichiometry for modest amounts of excess alumina before decreasing for compositions greater than $n = 2$; values of 12.2, 12.3 and 12.1 GPa for compositions of $n = 1$, $n = 1.2$, and $n = 1.5$, respectively, were measured, compared to 11.2, then 11.0 GPa for $n = 2$ and $n = 2.5$ compositions. Solid solution spinel was achieved for all the compositions investigated, indicating stoichiometry can alter the mechanical properties of single phase spinel. However, it should be noted that LiF was used as a densification aid in these studies, and its effects on the

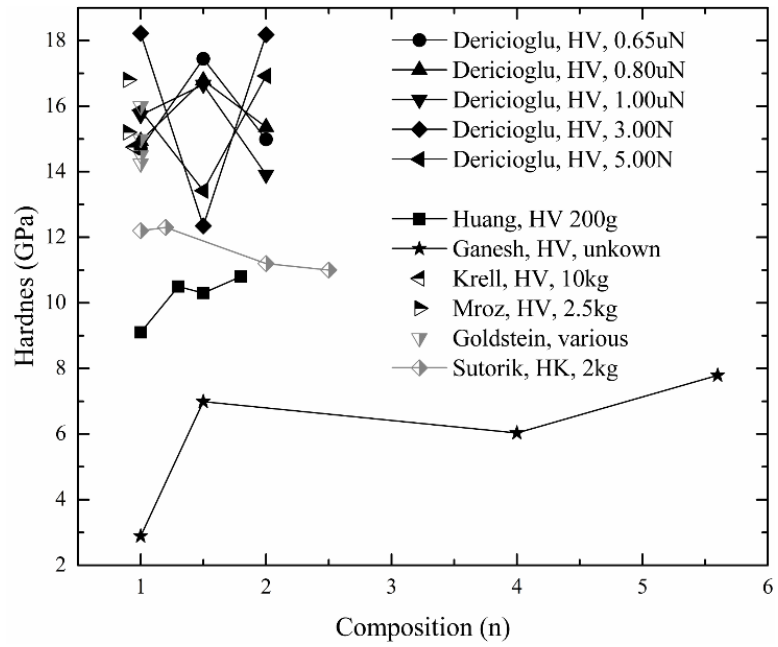


Figure 2.2 Reported hardness values for single phase magnesium aluminate spinel of various compositions are shown.

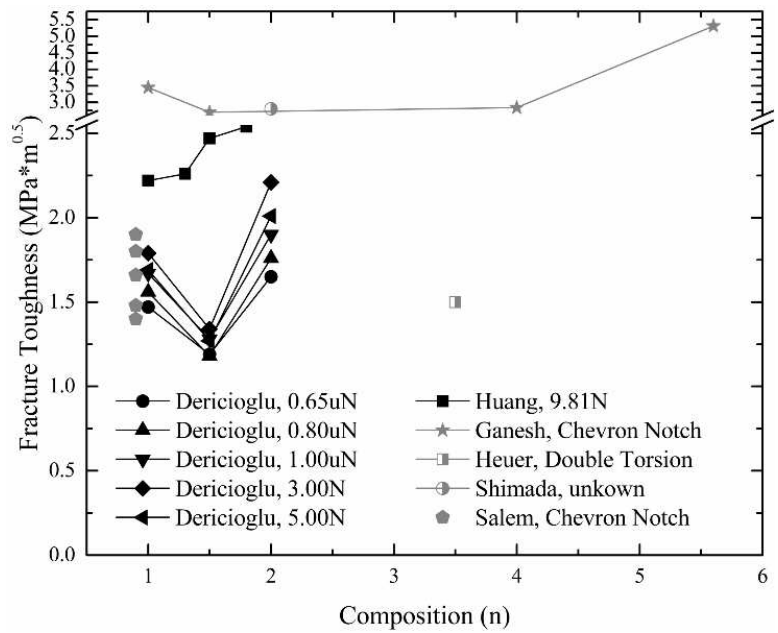


Figure 2.3 Reported fracture toughness values for single phase magnesium aluminate spinel of various compositions are shown.

mechanical properties of spinel is still not fully understood. Therefore, isolating the effects of LiF and Al-content on the hardness is difficult.

Work by Krell²⁴ investigated the Knoop and Vickers hardnesses for compositions ranging from $n = 1$ to $n = 2.5$ and for grain sizes ranging from approximately $0.2 \mu\text{m}$ up to single crystal materials. Similar to the studies by Sutorik, all materials were confirmed to be single phase spinel, and hardness values were significantly lower for material with a composition of $n > 2$, all other variables held constant. In addition, this work demonstrated that the hardness for a given composition was relatively independent of grain size from $5 \mu\text{m}$ grains up to single crystal materials. Hardness increased by $1.0 - 1.5 \text{ GPa}$ for a given composition (up to 15.5 GPa for $n = 1$ material) if a grain size less than $1.0 \mu\text{m}$ was maintained.

Salem²⁷ demonstrated that grain size also had an effect on fracture toughness of spinel; values increased from $1.4 - 1.9 \text{ MPa}\sqrt{\text{m}}$ as grain size decreased from approximately $300 \mu\text{m}$ to less than $100 \mu\text{m}$. The failure at large grain sizes is attributed to Al-rich phases segregated at grain boundaries and evidence of tensile residual stresses at Al_2O_3 particles within the matrix is presented. The specimens investigated were commercially fabricated and therefore details pertaining to processing methods and exact compositions are not provided.

The hardness and toughness values provided by Ganesh^{31,40}, represent the highest toughness and lowest hardness values shown in Figure 2.2 and Figure 2.3. High hardness was attributed to small grain size, which was retained because of grain boundary pinning due to the presence of Al_2O_3 particles. A maximum toughness of $5.31 \text{ MPa}\sqrt{\text{m}}$ was measured for the overall composition of $n = 5.6$, suggesting drastic improvements to fracture toughness are possible with increased addition of Al_2O_3 . However, the practicality of such Al-rich compositions for transparent applications needs further investigation.

2.3 Fracture mechanics of brittle materials

In order to understand how fracture toughness might be improved, a brief background of fracture mechanics is provided. The stress at which a brittle material fails^{2, 41, 42} is limited by the inherent flaws within the material⁴³ and dependent upon the geometry and loading conditions present, resulting in the relationship

$$\sigma = \frac{K_i}{Y\sqrt{c}} \quad (2.1)$$

where Y is a dimensionless parameter determined by geometry and the mode of loading, i . The term c denotes the length of the flaw within the material (defined geometrically as a half-penny shaped crack), and K_i is the stress intensity factor, which indicates the amplitude of the stress singularity of the crack tip stress field. In application, a specimen can be loaded until failure occurs at a critical stress, σ_c . If the size of the flaw, the loading conditions, and specimen geometry are known, the critical stress intensity factor, or toughness, K_{iC} , for the active loading mode, i , can be determined. It becomes apparent that there are two methods to improve the stress at which a brittle material fails; reduce the size of the flaws in the material through refining the processing and finishing routine, or increase toughness of the material as proposed in this thesis.

2.3.1 Modes of crack loading

In linear elastic fracture mechanics, the way in which a flaw or crack propagates depends how it is oriented relative to an applied load. Three loading modes, or a combination of them, can be used to describe such orientations, as shown in Figure 2.4. The critical stress intensity factor at which an existing crack will propagate under mode I loading is thus denoted as K_{IC} . Of

the three loading modes, mode I loading maximizes the amount of energy released as a crack propagates. Therefore, K_{IC} typically dictates the toughness of a material. Much of the effort to improve the toughness of a material is therefore devoted to either increasing the value of K_{IC} , or redirecting the path of a propagating crack out of the plane of mode I loading and creating a condition of mixed mode loading. Such toughening is typically achieved in traditional ceramic systems by the addition of a second phase, as discussed in section 2.4.

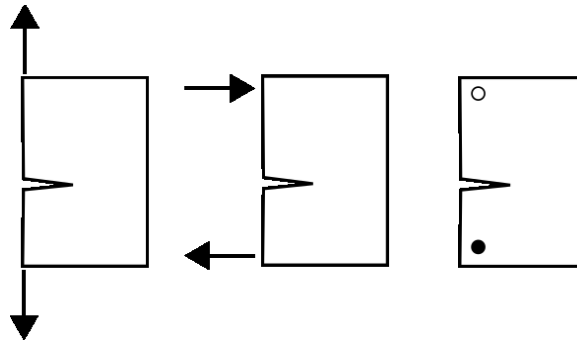


Figure 2.4 Loading modes for a half penny crack are shown. Mode I (left) demonstrates uniaxial tension, or crack opening. Mode II (middle) demonstrates in-plane shear loading, and mode III (right) demonstrates out-of-plane shearing, or tearing. The white and dark circles represent a loading direction into the page and out of the page, respectively.

2.3.2 R-Curve Behavior

R-curve behavior in brittle materials is defined as an increase in toughness observed with crack extension⁴⁴. Such behavior indicates that there are mechanisms active in the wake of the crack which increase the rate of energy dissipation, and materials that demonstrate this are said to exhibit rising R-curve behavior. The rate of energy dissipation is defined by the strain energy release rate⁴¹, G

$$G = - \frac{d(-W_L + U_E)}{d(c)} \quad (2.2)$$

This relationship represents the elastic energy available to create an infinitesimal crack extension

based on the contributions from the introduction of the crack, U_E , and the work performed by external forces, W_L . The critical energy release rate at which a crack will grow, G_c , is considered to be a material property independent of applied load or geometry. Therefore, if a value $G > G_c$ is attained because the external work on the system exceeds the potential energy available for crack growth, crack extension will occur. In relation to R-curve behavior, this implies that the rate in which external energy is dissipated increases with each incremental increase of the crack length for materials with rising R-curve behavior. The strain energy release rate can be related to the stress intensity factor through the relationships⁴⁵

$$G = -\frac{K_I^2}{E} \quad (2.3)$$

$$G = -\frac{K_I^2(1 - \nu^2)}{E} \quad (2.4)$$

For plane stress and plane strain loading conditions, respectively, where ν is the Poisson's ratio and E is the elastic modulus. At critical values, the critical strain energy release rate, G_c , can be related to the fracture toughness, K_{IC} .

2.4 Second phase toughening in ceramics

The toughness of ceramics has been improved through a variety of methods, as discussed below. Transformation toughening and crack bridging are mechanisms active in the wake of the propagated crack. Therefore, systems utilizing these mechanisms exhibit rising R-curve behavior. Crack bowing and crack deflection are toughening mechanisms active at the crack tip, and therefore typically do not affect the R-curve behavior of the material.

2.4.1 Transformation toughening

Transformation toughening utilizes the energy from a propagating crack to induce an expansive phase change in metastable particles within the matrix, creating compressive stresses that exert tractions on the crack faces, thereby closing the crack^{46,47}. ZrO_2 is a material that has been used extensively because particles of the metastable tetragonal phase can be dispersed within a matrix, and a review by Hannink⁴⁸ demonstrated that dispersions of various amounts of ZrO_2 within CeO_2 , Y_2O_3 , and MgO matrices resulted in improved toughnesses from 6 to 14, 3 to 11, and 3 to 14 $MPa\sqrt{m}$, respectively. The phase transformation toughening mechanism is shown schematically in Figure 2.5. While significant improvements to toughness have been demonstrated utilizing this technique, transformation toughening has not been successfully applied to transparent material systems.

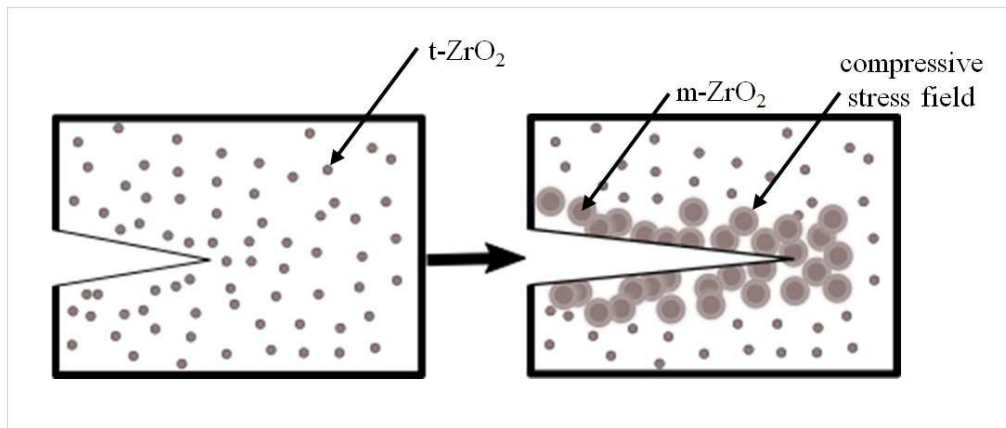


Figure 2.5 Transformation toughening is shown. The opening of the propagating crack introduces a stress to the dispersed metastable particles. The stress induces a phase transformation, resulting in a volume expansion that introduces compressive stresses which act to close the crack.

2.4.2 Crack bridging

Crack bridging occurs when microstructural elements are in contact with both faces of a crack and additional energy is required to overcome the traction of these elements in order for

the propagating crack to continue to open, as shown in Figure 2.6. It has been shown that the most effective way to implement crack bridging is by the use of fibers or ductile second phase particles within a matrix^{49, 50}. While the use of such constituents may be impractical for transparent applications, the same effect has been demonstrated to a lesser degree using other morphologies of second phase materials. For example, it was demonstrated that irregular shaped Al_2O_3 grains within an Al_2O_3 matrix exhibit crack bridging because of the additional energy required to overcome friction as these grains are pulled free from the matrix as the crack opens⁵¹. Case studies of literature⁴⁹ demonstrate rising R-curve behavior where the toughness of Al_2O_3 reinforced with SiC whiskers increases with the size of the starting flaw; the toughness increased from 4.5 to 5.0 $\text{MPa}\sqrt{\text{m}}$ when the starting flaw size increased from less than 30 μm to 50 μm , and values of 6.2 - 8.3 $\text{MPa}\sqrt{\text{m}}$ were measured for flaws ranging from 300 - 920 μm .

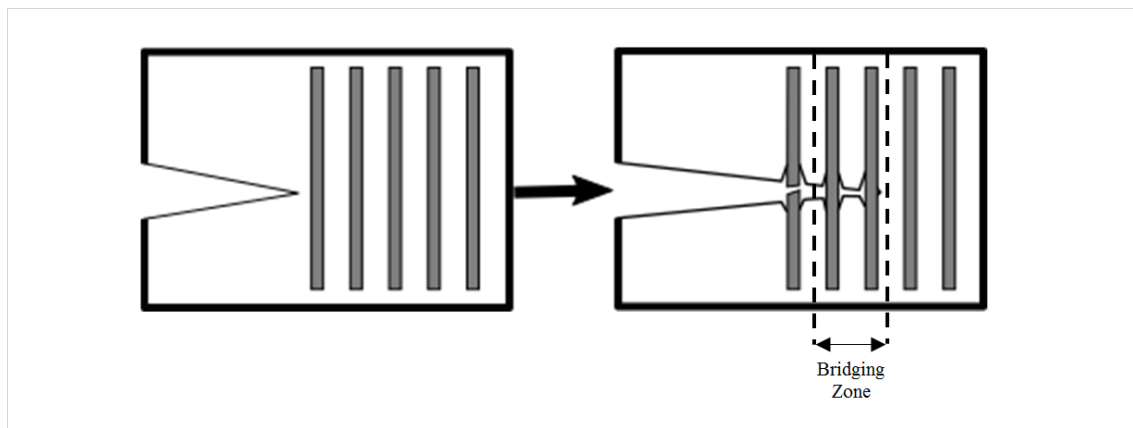


Figure 2.6 Crack bridging is shown. For further crack opening to occur, the traction forces between the fibers and the matrix must be overcome. This debonding increases energy dissipation until the fiber breaks. The unbroken fibers in the wake of the crack constitute the active bridging zone.

2.4.3 Crack bowing

Crack bowing is a mechanism by which a crack propagating through a matrix is impinged when it encounters second phase particles^{52, 53}. The bowing of the crack front decreases the

stress concentration experienced at the crack front, effectively increasing the toughness of the material. Bowing continues until the fracture toughness of the embedded particle is exceeded, at which point the crack propagates through the particle⁵⁴. While an effective toughening technique, crack bowing is only effective if the second phase particles lie within the plane of the propagating crack, as shown in Figure 2.7.

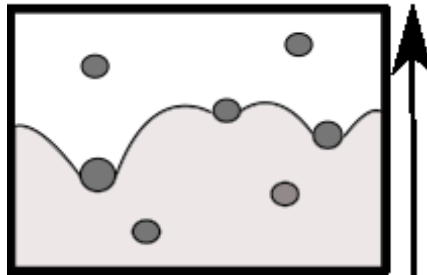


Figure 2.7 Crack bowing is shown where the arrow indicates the direction of propagation (the crack wake is shown in grey). As the front encounters second phase particles, it is pinned. Further propagation causes the front to curve outward, increasing the length of the active front and therefore increasing the rate of energy dissipation.

2.4.4 Crack deflection

Crack deflection can cause a crack to bend or twist out of the plane of mode I fracture; the subsequent mixed mode fracture loading results in a lower stress concentration at the crack tip and therefore a lower driving force for continued crack propagation. This is shown in Figure 2.8 where delamination between layers redirects the direction of propagation. This technique is already employed for window applications, where layers of transparent spinel are bonded together.

Rather than layers, second phase particles can be introduced in such a way as to redirect the direction of the propagation, thus increasing the tortuosity of the crack path and increasing the energy required for further propagation, as shown in Figure 2.9. According to Rodel⁴⁹, a

propagating crack is forced to twist and tilt between the second phase particles, which produces a stress field that lowers the crack driving force.

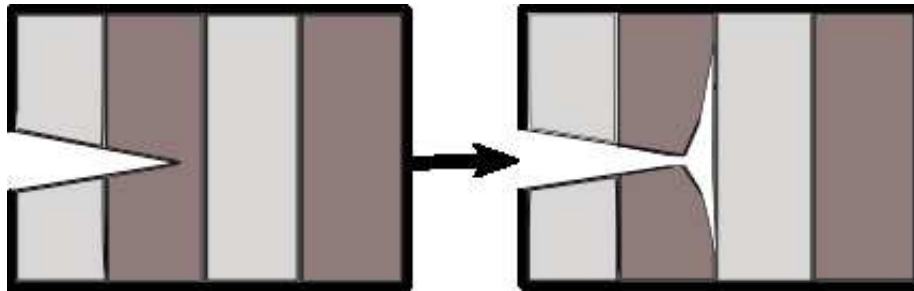


Figure 2.8 Crack deflection at interfacial layers is shown. Propagation is initially due to mode I loading, but is redirected into a mixed loading condition.

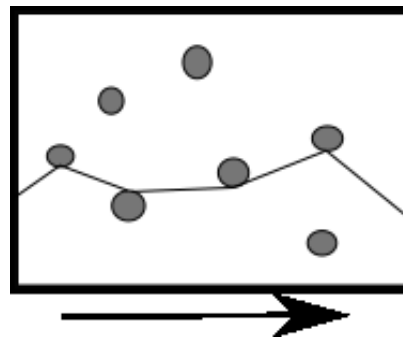


Figure 2.9 Crack deflection at second phase particles is shown where the arrow indicates the direction of propagation. Similar to Figure 2.8, the crack is redirected, resulting in mixed loading modes

Faber and Evans develop a fracture mechanics approach⁵⁴ to predict fracture toughness of a composite based on the particle size, shape, volume fraction and distribution within a matrix, which they confirm experimentally⁵⁵. The findings of these works determined that second phase particles can alter the plane of the propagating crack because of residual stresses, while later works demonstrated that residual tensile stresses may encourage propagation towards the

particles while compressive stresses will cause cracks to bend away^{52, 56, 57}, as shown in Figure 2.10.

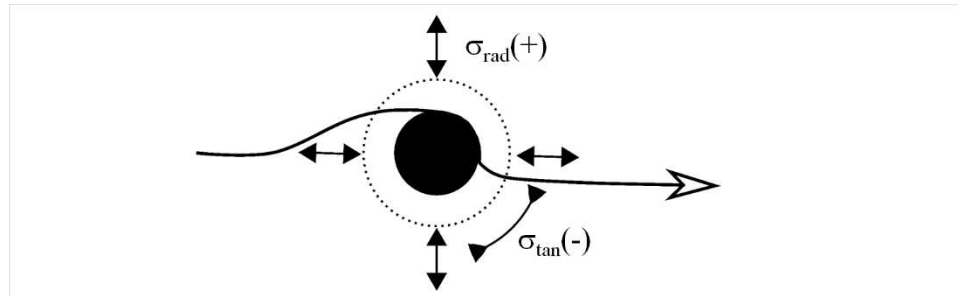


Figure 2.10 Crack deflection due to residual stresses is illustrated for the case when the thermal expansion coefficient of the second phase particle is greater than that for the matrix ($\alpha_p > \alpha_m$). During cooling, the particle shrinks faster than the surrounding matrix, resulting in radial tensile stress and compressive tangential (hoop) stress in the matrix. The propagating crack is first deflected away by compressive stresses, then attracted by tensile stresses.

Work by Taya⁵⁸, demonstrated that residual tensile stresses are created around TiB_2 particles within a matrix of SiC because of the CTE mismatch created during cooling. The change in fracture toughness of the composite material was found to be related to the magnitude of the residual stresses and the interparticle spacing

$$\Delta K_I = 2q \sqrt{\frac{2(\lambda - d)}{\pi}} \quad (2.5)$$

where q is the residual stress, λ is the spacing between the centroids of the particles, and d is the diameter of the particles. The increased tortuosity of the crack path leads to toughening because the overall length of the crack increases, and thus the new surface area created and total energy dissipated are increased.

The ideal second phase inclusion would activate a combination of toughening mechanisms. For example, a particle that creates residual stresses will first deflect the crack out

of the plane of mode I loading, increasing the critical stress intensity factor observed by the crack front. If this effect can be achieved using second phase particles that are more crack resistant than the matrix, further energy will be required once the front is pinned by the second phase particles. Finally, strongly bound second phase particles will create additional friction via crack bridging as the crack continues to open.

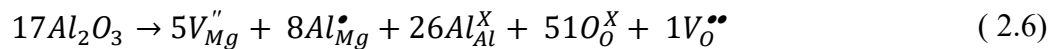
2.4.5 Second phase particles and light scattering

While the presence of a second phase has been shown to enhance mechanical properties, the strategies discussed above have yet to be implemented in transparent materials because gains to toughness may be offset by a loss in transparency. As discussed earlier, scatter could be reduced by ensuring the size of these second phase inclusions is small compared to the wavelength of light to be transmitted, but maintaining such small grain sizes during densification is complicated. However, Al_2O_3 is soluble into magnesium aluminate spinel, allowing for unique control of the microstructural evolution of the second phase during densification and subsequent heat treatments. Furthermore, Al_2O_3 has been produced as a transparent, polycrystalline material^{8,9,35}, and for wavelengths of 0.5 - 5 μm , the refractive index of Al_2O_3 decreases from approximately 1.78 to 1.60 compared to 1.71 to 1.60 for spinel². Other than BeO and MgO, the refractive index of Al_2O_3 most closely matches that of spinel and would create the least amount of light scatter if grains are large enough to interact with wavelengths of interest. Therefore, large second phase particles of Al_2O_3 are expected to produce minimal scattering, but the ability to control the morphology of the second phase particles makes it possible to further optimize the structure if the microstructural evolution is understood, as discussed in section 2.6. However, in order to better understand the structural evolution of the spinel- Al_2O_3 system, the individual structures of the constituent phases are presented first.

2.5 Structure of constituent phases

The corundum structure ($R\bar{3}c$ space group⁵⁹) describes α - Al_2O_3 , where O ions form a hexagonal close packed unit cell and $2/3$ of the octahedral interstices are occupied by Al^{3+} ions. The resulting conventional unit cell has an elongated c-axis relative to the a-axis, as shown in Figure 2.11. Stoichiometric magnesium aluminate spinel, the namesake of the spinel structure, belongs to the $\text{Fd}3m$ space group. A conventional unit cell consists of 8 molecular units of spinel arranged in an FCC oxygen lattice with $1/8$ of the tetrahedral interstices occupied by Mg^{2+} ions and $1/2$ of the octahedral interstices occupied by Al^{3+} ions²⁰. This describes an ideal structure in which there is no inversion of the cation sites, although some degree of inversion is unavoidable in synthetic spinel.

The structure of non-stoichiometric spinel is not as well agreed upon in literature. In general, it is accepted that the cubic structure is maintained as excess Al^{3+} ions occupy tetrahedral Mg^{2+} sites and cation vacancies are created to maintain charge neutrality^{20, 60-62}, but it is unclear whether these vacancies occupy octahedral sites, tetrahedral sites, or both. It has been further proposed that oxygen vacancies are also created for charge compensation⁶³⁻⁶⁵. The theory of oxygen vacancies is supported by Okuyama⁶⁶, where the measured density of spinels of varying stoichiometries closely match theoretical densities predicted by the defect reaction



where increasing the matrix composition by 17 units of Al_2O_3 expands the spinel lattice by 13 units by placing 8 Al ions on Mg sites and creating 5 Mg vacancies and 1 O vacancy to maintain charge balance. The spinel lattice has thus expanded by 13 Mg sites, 26 Al sites, and 52 O sites. The crystal structures of stoichiometric ($n = 1$) and Al-rich ($n = 2$) spinel are also shown in Figure 2.11, where the structure of the $n = 2$ spinel is based off the above defect reaction.

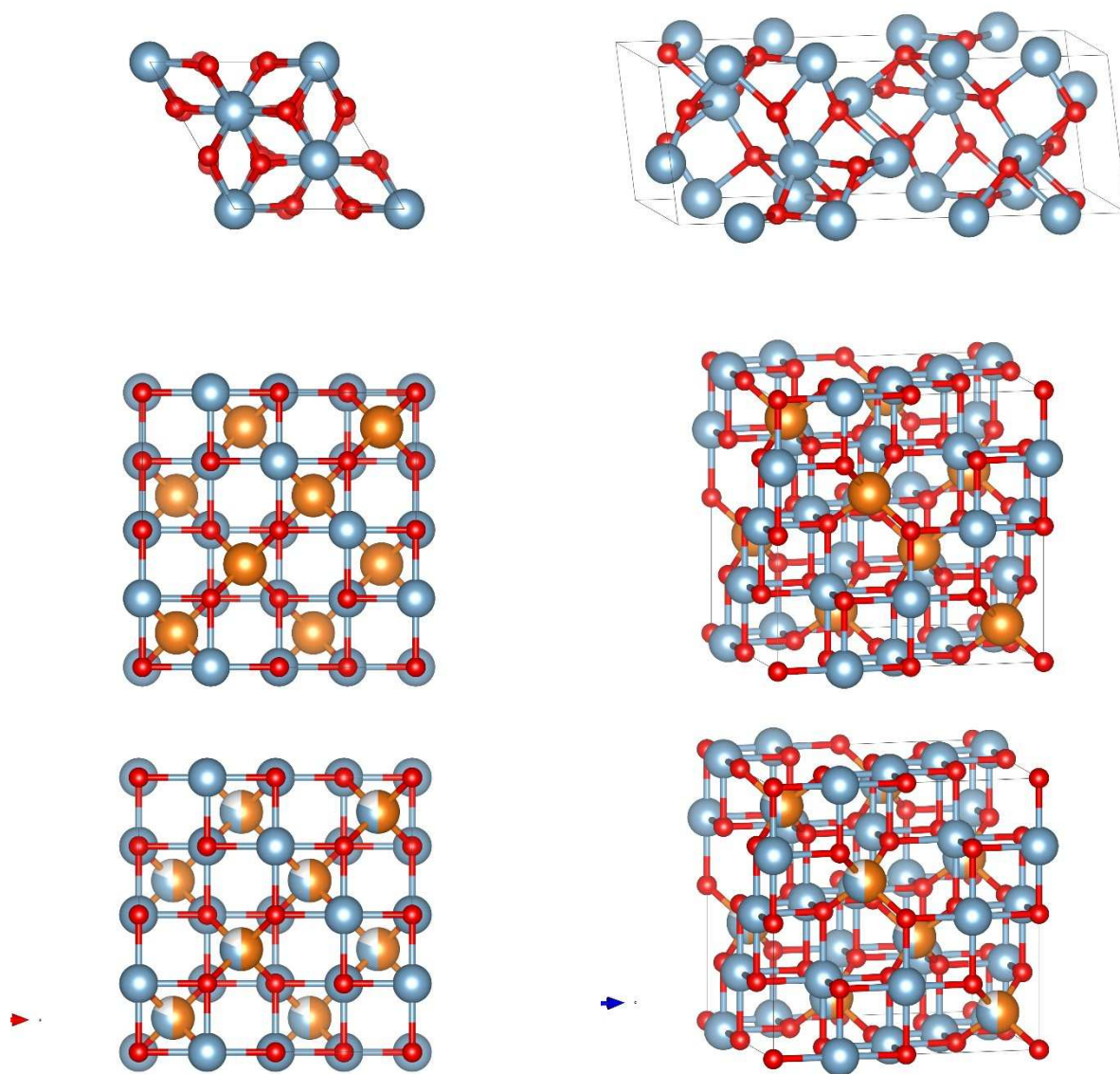


Figure 2.11 Conventional unit cells for are shown for $\alpha\text{-Al}_2\text{O}_3$ (top), stoichiometric, $n = 1$ spinel (middle), and Al-rich, $n = 2$ spinel (bottom). The left column is the cell as viewed down $[001]$ and the right column is an off-axis view (approximately $[1, -0.15, -0.25]$). The red, grey, and orange colors denote the site fractions of O, Al, and Mg ions, respectively. White in the $n = 2$ structure denotes the site fraction of vacancies, as evident in the mixed tetrahedral sites. These structures were created using VESTA Visualization Software (Ver. 3.3.2)

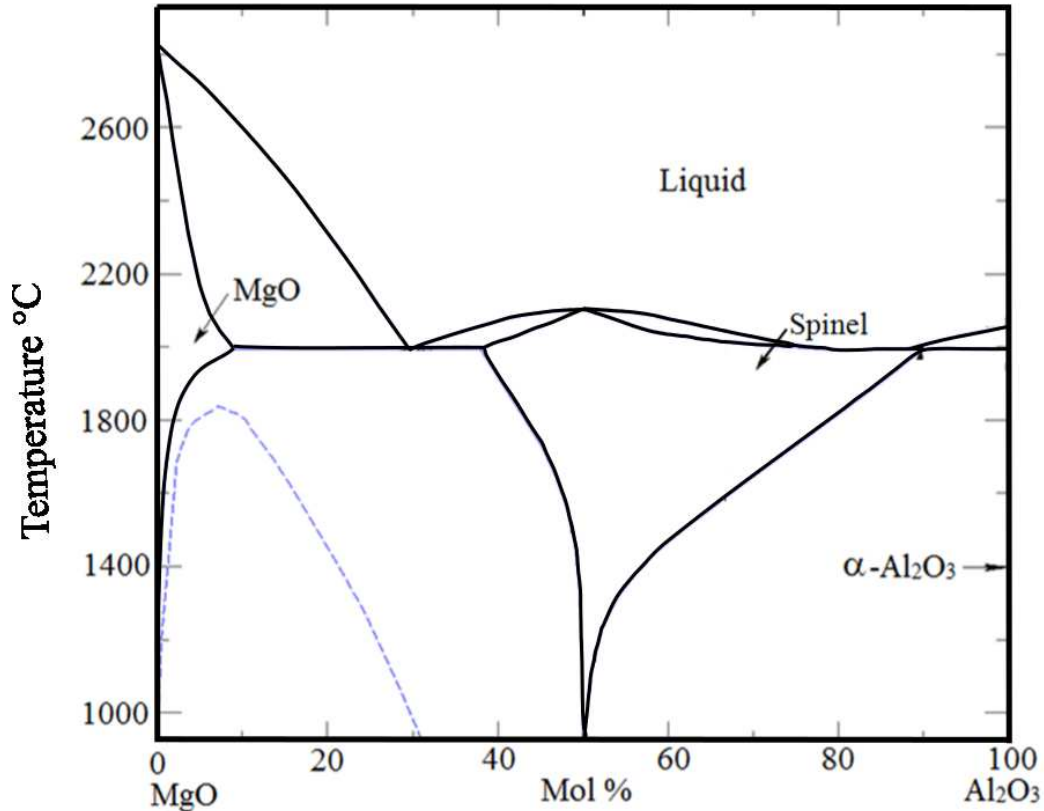


Figure 2.12 The MgO-Al₂O₃ phase diagram is shown⁶⁷.

2.6 Microstructural evolution

The MgO-Al₂O₃ phase diagram⁶⁷ is shown in Figure 2.12, where spinel is the only single phase region between the two end member compositions. A wide range of compositions within this single phase is accessible if the material is processed at high temperatures, owing to increased mixing because of increased entropy at elevated temperatures. In this thesis, compositions of $n = 1$ and $n = 2$ (50 mol % and 66.6 mol %) are investigated. For the $n = 2$ material, crossing the spinel-Al₂O₃ phase boundary will result in either precipitation of Al₂O₃ from Al-rich spinel or dissolution of Al₂O₃ into spinel, depending on the direction of the temperature change^{68, 69}. The kinetics governing precipitation and dissolution⁷⁰⁻⁷⁴ of Al₂O₃ require discussion.

2.6.1 Precipitation

The precipitation of a new phase within the system introduces a volume of material with lower free energy, but new surfaces are also created which increase free energy. Assuming the formation of a spherical precipitate, the change in free energy of a system can be modeled as competing volume and surface area terms⁷⁵

$$\Delta G = \frac{4\pi r^3}{3} \frac{\Delta g^v}{v} + 4\pi r^2 \gamma \quad (2.7)$$

where r is the radius of the precipitate, γ is the specific surface energy, and v is the volume of the new phase. Δg^v is the chemical free energy change per each atom as the atom is transferred from the original phase into the new phase and is negative if the transfer results in a lower free energy for the system. Equation (2.7) demonstrates that the change in free energy of the system increases for small radii up to a maximum at a critical radius, r^* . Once the radius increases beyond r^* , the volumetric term is dominant; the nucleus of the precipitate is now stable and further growth of the precipitate will result in further reducing free energy.

2.6.2 Nucleation and rate limiting mechanisms

The above relationship assumes the formation of a spherical precipitate, similar to what is expected in homogeneous nucleation if minimal strain energy exists between the original and new phases⁷⁵. While such a model provides insight to the competing mechanisms active during precipitation, such simple precipitation is rarely observed in solid-solid systems. It was shown by Lewis⁷⁶ that precipitation of α -Al₂O₃ from single crystals of Al-rich ($n = 2$ and $n = 4$) spinel was limited to the surface and preceded by the formation of two intermediate phases. Both phases had monoclinic symmetry; the first had the orientation relationship

$$\{113\}_m \parallel \{001\}_p, \langle 110_m \parallel 010_p \rangle \quad (2.8)$$

while the second phase had the orientation relationship

$$\{100\}_m \parallel \{010\}_p, \langle 110_m \parallel 001_p \rangle \quad (2.9)$$

where m and p denote the matrix and precipitate, respectively. The combination of precipitation at the surface and specific orientation relationships imply a large strain energy is associated with the formation of hexagonal α -Al₂O₃ from cubic spinel, in agreement with later work by Donlon³⁶. This conclusion is further supported by Bansal⁷⁷, who also observed intermediate phases prior to the precipitation of α -Al₂O₃ on the surface of single crystal spinel (n = 3.5). These phases were determined by TEM to be coherent, then semi-coherent, then incoherent in relation to the matrix spinel structure. Panda⁷⁸ demonstrated that precipitation in polycrystalline material (n = 2) was not restricted to the surface, allowing uniform precipitation of α -Al₂O₃ throughout the bulk without the formation of intermediate phases. Because of the volume contraction associated with precipitation of α -Al₂O₃ from spinel, precipitation initiated at existing grain boundaries to more easily allow the formation of pores. Together, these studies suggest that precipitation in this system might better be modeled by heterogeneous nucleation at existing surfaces where the geometry of the precipitate is dependent on the orientation relationship with the matrix grains⁷³. Equation (2.7) may therefore be modified as

$$\Delta G = \left(\frac{2\pi r^3}{3} \frac{\Delta g^v}{v} + 2\pi r^2 \gamma \right) (2 - 3\cos\theta + \cos^3\theta) \quad (2.10)$$

where θ represents the approximate dihedral angle of the Al₂O₃ precipitate forming at an existing spinel-spinel grain boundary, as illustrated in Figure 2.13.

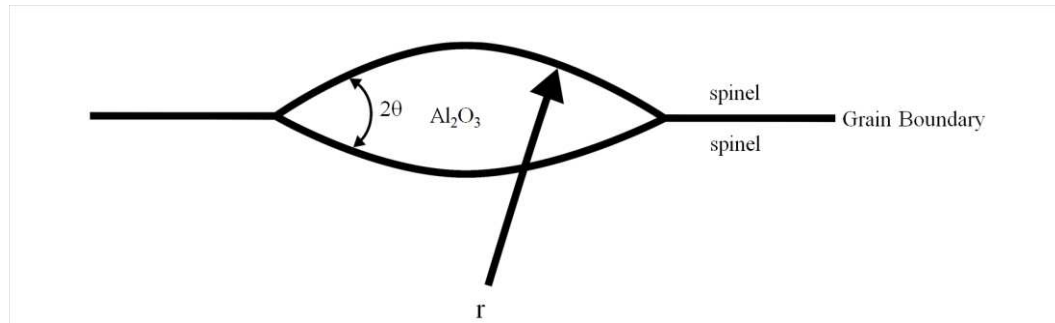


Figure 2.13 Precipitation of Al_2O_3 at a grain boundary in polycrystalline spinel is shown schematically

Once stable nucleation is established, Panda⁷⁸ also demonstrates that the rate of precipitation follows the trends of many other material systems; at high temperatures (just below the solvus line) precipitation is limited by a low nucleation rate, while at low temperatures, the diffusion necessary for precipitation is slowed. A maximum precipitation rate occurs at approximately 1400°C for the composition investigated.

Abrupt changes in the MgO and Al_2O_3 concentrations at the matrix-precipitate interface⁷⁸ suggest that diffusion of constituents to the boundary is fast compared to the time it takes for restructuring of the new phase, and the process is therefore reaction limited (rather than diffusion limited). This is further supported by studies by Ando^{79, 80} and Oishi⁸¹, where increased diffusion rates are attributed to increased disorder along grain boundaries.

2.6.3 Dissolution

As shown in the preceding sections, precipitation from Al-rich spinel has been studied extensively, but a systematic study exploring the controlling mechanisms of the reverse process is lacking. To a first approximation, dissolution can be thought of as “reverse precipitation” where no nucleation step is required⁷⁰. However, the concentration gradients of the diffusing species differ between precipitation and dissolution. During precipitation, a nucleus grows by

consuming the diffusing species that are immediately adjacent to the phase boundary; the concentration of this species is therefore lower near the boundary and increases with increasing distance from the precipitate. In dissolution, the concentration of the diffusing species is highest immediately adjacent to the boundary and decreases with increasing distance from the boundary. However, simple models summarized by Abbaschian⁷⁰ demonstrate that the location of the phase boundary in one dimension can still be approximated according to \sqrt{t}

$$x(t) = x_0 - k\sqrt{Dt} \quad (2.11)$$

where x_0 is the original thickness, k is a constant, D is the diffusivity, and t is time.

In order to improve the simple dissolution models available, a better understanding of the concentration gradient is required. Aaron⁸² reviews these existing models and presents a modified concentration profile relationship to explain the dissolution of V_4C_3 observed in an Fe-V-C alloy. In keeping with previous models, Aaron makes a number of assumptions including (1) the kinetics are dictated by solid-state diffusion, (2) surface strain effects are minimal, (3) the system is in equilibrium before dissolution starts, (4) there is no interaction from other particles within the matrix, and (5) there is a uniform concentration profile outside of the particle. After demonstrating that interface reactions and curvature effects can be neglected for the majority of situations, a relationship for the concentration profile of diffusion limited dissolution is presented

$$C_I(R) = C_I(\infty) \exp\left(\frac{\gamma_{AB} V_P}{TRC_P}\right) \quad (2.12)$$

where C_I is the concentration of the diffusing species at the interface (outside of the particle), γ_{AB} is the specific interfacial energy of the boundary, V_P is the molar volume of the precipitate, C_P is the mole fraction of the diffusing species in the precipitate, and T is the absolute temperature.

Aaron demonstrated the above relationship to be accurate for the dissolution of V_4C_3 into an Fe matrix. However, the model could not predict the dissolution of “complex sulfides and oxides” created by impurities in the system, indicating the model is appropriate for diffusion limited dissolution, but better models are still needed for reaction limited dissolution.

2.7 Proposed scope of research

To summarize, magnesium aluminate spinel is a material that shows great potential for transparent armor applications, but improved fracture toughness is desirable. Traditional toughening techniques that rely on the addition of a second phase have been avoided because of light scattering caused by the presence of the second phase. Studies of precipitation in spinel have demonstrated that the structure of both single-phase Al-rich spinel and two-phase Al_2O_3 -spinel composites may be altered at elevated temperatures. It is reasonable to suggest that a more complete understanding of the mechanisms controlling precipitation and dissolution would permit better control of the evolution of second phase Al_2O_3 . Such control could ultimately allow one to tailor the microstructure of second phase particles in such a way as to include the benefits of second-phase toughening while minimizing light scatter.

The goal of this thesis is to first demonstrate that the structure of second phase Al_2O_3 within an Al-rich spinel matrix can be controlled using densification and heat treatment regimes available in industrial scale manufacturing processes. Next, the resulting effects on toughness and transparency will be investigated, ultimately demonstrating the mechanical enhancements that might be realized for transparent armor applications.

2.8 References

- 1 D.C. Harris, "History and development of polycrystalline optical spinel in the U.S.;" pp. 1–22 in *Wind. Dome Technol. Mater.* Edited by R.W. Tustison. SPIE- The International Society for Optical Engineering, Orlando, 2005.
- 2 D.C. Harris, *Materials for Infrared Windows and Domes: Properties and Performance*. SPIE- The International Society for Optical Engineering, Bellingham, Washinton, 1999.
- 3 M. Medraj, R. Hammond, M.A. Parvez, R.A.L. Drew, and W.T. Thompson, "High temperature neutron diffraction study of the $\text{Al}_2\text{O}_3 - \text{Y}_2\text{O}_3$ system," *J. Eur. Ceram. Soc.*, **26** 3515–3524 (2006).
- 4 P. Hogan, T. Stefanik, C. Willingham, R. Gentilman, R. Integrated, and D. Systems, "Transparent Yttria for IR Windows and Domes – Past and Present;" in *DoD Electromagn. Wind. Symp.* Norfolk, Virginia, 2004.
- 5 R. Rice, *Characterization of Hot-Pressed MgO*. Washington, D.C., 1971.
- 6 A. Krell, J. Klimke, and T. Hutzler, "Advanced spinel and sub- μm Al_2O_3 for transparent armour applications," *J. Eur. Ceram. Soc.*, **29** [2] 275–281 (2009).
- 7 Y. Chou and D.J. Green, "Silicon Carbide Platelet/Alumina Composites: II, Mechanical Properties," *J. Am. Ceram. Soc.*, **76** [6] 1452–1458 (1993).
- 8 I. Yamashita, H. Nagayama, and K. Tsukuma, "Transmission Properties of Translucent Polycrystalline Alumina," *J. Am. Ceram. Soc.*, **91** [8] 2611–2616 (2008).
- 9 R. Apetz and M.P.B. Bruggen, "Transparent Alumina: A Light-Scattering Model," *J. Am. Ceram. Soc.*, **86** [3] 480–486 (2003).
- 10 A.A. DiGiovanni, L. Fehrenbacher, and D.W. Roy, "Hard Domes and Windows from Magnesium Aluminate Spinel;" pp. 56–63 in *Wind. Dome Technol. Mater.* Edited by R.W. Tustison. SPIE- The International Society for Optical Engineering, Orlando, 2005.
- 11 A. Krell, J. Klimke, and T. Hutzler, "Transparent compact ceramics: Inherent physical issues," *Opt. Mater. (Amst.)*, **31** [8] 1144–1150 (2009).
- 12 R.M. Sullivan, "A Historical View of AlON;" pp. 23–32 in *Wind. Dome Technol. Mater.* Edited by R.W. Tustison. SPIE- The International Society for Optical Engineering, Orlando, FL, 2005.
- 13 M. Rubat Du Merac, H.J. Kleebe, M.M. Muller, and I.E. Reimanis, "Fifty years of research and development coming to fruition; Unraveling the complex interactions during processing of transparent magnesium aluminate (MgAl_2O_4) spinel," *J. Am. Ceram. Soc.*, **96** [11] 3341–3365 (2013).

- 14 A. Pechenik, G.J. Piermarini, and S.C. Danforth, "Fabrication of transparent silicon nitride from nanosize particles," *J. Am. Ceram. Soc.*, **75** [12] 3283–3288 (1992).
- 15 J.S. Goela and R.L. Taylor, "Transparent SiC for mid-IR windows and Domes;" in *SPIE Int. Soc. Opt. Photonics*. Edited by P. Klocek. San Diego, California, 1994.
- 16 D. Jiang and A.K. Mukherjee, "Synthesis of Y₂O₃-MgO nanopowder and infrared transmission of the sintered nanocomposite," *Int. Soc. Opt. Photonics*, **7030** 703007-703007–6 (2008).
- 17 J. Wang, L. Zhang, D. Chen, E.H. Jordan, and M. Gell, "Y₂O₃-MgO-ZrO₂ Infrared Transparent Ceramic Nanocomposites," *J. Am. Ceram. Soc.*, **1037** n/a-n/a (2011).
- 18 C.K. Muoto, E.H. Jordan, M. Gell, and M. Aindow, "Phase Homogeneity in Y₂O₃-MgO Nanocomposites Synthesized by Thermal Decomposition of Nitrate Precursors with Ammonium Acetate Additions," *J. Am. Ceram. Soc.*, **94** [12] 4207–4217 (2011).
- 19 J. Wang, E.H. Jordan, and M. Gell, "Plasma Sprayed Dense MgO-Y₂O₃ Nanocomposite Coatings Using Sol-Gel Combustion Synthesized Powder," *J. Therm. Spray Technol.*, **19** [5] 873–878 (2010).
- 20 K. Sickafus and J. Wills, "Structure of spinel," *J. Am. Ceram. Soc.*, **82** [12] 3279–3292 (1999).
- 21 J.L. Sepulveda, R.O. Loufty, S. Ibrahim, and S. Bilodeau, "Large Size Spinel Windows and Domes;" pp. 870806010–87080615 in *Wind. Dome Technol. Mater.* Edited by R.W. Tustison and B.J. Zelinski. SPIE- The International Society for Optical Engineering, Baltimore, 2013.
- 22 J. Spilman, J. Voyles, J. Nick, and L. Shaffer, "Manufacturing process scale-up of Optical Grade Transparent Spinel Ceramic at ArmorLine Corporation;" pp. 87080701–87080710 in *Wind. Dome Technol. Mater.* Edited by R.W. Tustison and B.J. Zelinski. SPIE- The International Society for Optical Engineering, Baltimore, 2013.
- 23 A. Goldstein, "Correlation between MgAl₂O₄-spinel structure, processing factors and functional properties of transparent parts (progress review)," *J. Eur. Ceram. Soc.*, **32** [11] 2869–2886 (2012).
- 24 A. Krell and A. Bales, "Grain Size-Dependent Hardness of Transparent Magnesium Aluminate Spinel," *Int. J. Appl. Ceram. Technol.*, **8** [5] 1108–1114 (2011).
- 25 A.C. Sutorik, G. Gilde, J.J. Swab, C. Cooper, R. Gamble, and E. Shanholtz, "Transparent Solid Solution Magnesium Aluminate Spinel Polycrystalline Ceramic with the Alumina-Rich Composition MgO·1.2 Al₂O₃," *J. Am. Ceram. Soc.*, **95** [2] 636–643 (2012).

- 26 A.C. Sutorik, C. Cooper, and G. Gilde, “Visible Light Transparency for Polycrystalline Ceramics of $\text{MgO}\cdot 2\text{Al}_2\text{O}_3$ and $\text{MgO}\cdot 2.5\text{Al}_2\text{O}_3$ Spinel Solid Solutions,” *J. Am. Ceram. Soc.*, **96** [12] 3704–3707 (2013).
- 27 J.A. Salem, “Transparent armor ceramics as spacecraft windows,” *J. Am. Ceram. Soc.*, **96** [1] 281–289 (2013).
- 28 A.C. Sutorik, G. Gilde, C. Cooper, J. Wright, and C. Hilton, “The Effect of Varied Amounts of LiF Sintering Aid on the Transparency of Alumina Rich Spinel Ceramic with the Composition $\text{MgO}\cdot 1.5\text{Al}_2\text{O}_3$,” *J. Am. Ceram. Soc.*, **95** [6] 1807–1810 (2012).
- 29 A.F. Dericoglu, A.R. Boccaccini, I. Dlouhy, and Y. Kagawa, “Effect of Chemical Composition on the Optical Properties and Fracture Toughness of Transparent Magnesium Aluminate Spinel Ceramics,” *Mater. Trans.*, **46** [5] 996–1003 (2005).
- 30 C.B. Huang, T.C. Lu, L. Bin Lin, M.Y. Lei, and C.X. Huang, “A Study on Toughening and Strengthening of Mg-Al Spinel Transparent Ceramics,” *Key Eng. Mater.*, **336–338** 1207–1210 (2007).
- 31 I. Ganesh, “A review on magnesium aluminate (MgAl_2O_4) spinel: synthesis, processing and applications,” *Int. Mater. Rev.*, **58** [2] 63–112 (2012).
- 32 T. Mroz, L.M. Goldman, A.D. Gledhill, D. Li, and N.P. Padture, “Nanostructured, Infrared-Transparent Magnesium-Aluminate Spinel with Superior Mechanical Properties,” *Int. J. Appl. Ceram. Technol.*, **9** [1] 83–90 (2012).
- 33 M. Shimada, T. Endo, T. Saito, and T. Sato, “Fabrication of transparent spinel polycrystalline materials,” *Mater. Lett.*, **28** [October] 413–415 (1996).
- 34 E.F. Osborn, “Subsolidus Reactions in Oxide Systems in the Presence of Water at High Pressures,” *J. Am. Ceram. Soc.*, **36** [5] 147–151 (1953).
- 35 K. Waetzig and A. Krell, “The Effect of Composition on the Optical Properties and Hardness of Transparent Al-rich $\text{MgO}\cdot n\text{Al}_2\text{O}_3$ Spinel Ceramics,” *J. Am. Ceram. Soc.*, **99** [3] 946–953 (2016).
- 36 W.T. Donlon, T.E. Mitchell, and A.H. Heuer, “Precipitation in non-stoichiometric spinel,” *J. Mater. Sci.*, **17** 1389–1397 (1982).
- 37 J. Zhang, W.W. Chen, and A.J. Ardell, “Solid Solution Strengthening of ZnS;” pp. 93–98 in *Int. Soc. Opt. Eng.* Edited by P. Klocek. San Diego, California, 1990.
- 38 N.S. Stoloff, D.K. Lezius, and T.L. Johnston, “Effect of Temperature on the Deformation of KCl-KBr Alloys,” *J. Appl. Phys.*, **34** [11] 3315–3322 (1963).

- 39 T.S. Liu, R.J. Stokes, and C.H. Li, "Fabrication and Plastic Behavior of Single-Crystal MgO-NiO and MgO-MnO Solid-Solution Alloys," *J. Am. Ceram. Soc.*, **47** [6] 276–279 (1964).
- 40 S. Bhaduri and S.B. Bhaduri, "Microstructural and mechanical properties of nanocrystalline spinel and related composites," *Ceram. Int.*, **28** [2] 153–158 (2002).
- 41 D.J. Green, "Chapter 8: Brittle Fracture;" pp. 210–265 in *An Introd. to Mech. Prop. Ceram.*, 1st ed. Press Syndicate of The University of Cambridge, Cambridge, MA, 1998.
- 42 D.W. Richerson, *Modern Ceramic Engineering: Properties, Processing, and Use in Design*, Third. CRC Press, Boca Raton, FL, 2005.
- 43 A.A. Griffith, "The Phenomena of Rupture and Flow in Solids," *Philisophical Trans. R. Soc. London*, **221** [582–593] 163–198 (1921).
- 44 R.W. Steinbrech, "R-Curve Behavior of Ceramics;" pp. 187–208 in *Fract. Mech. Ceram. Compos. R-Curve Behav. Fatigue*. Edited by R.C. Bradt, D.P.H. Hasselman, D. Munz, M. Sakai and V.Y. Shevchenko. Springer US, Boston, MA, 1992.
- 45 G.R. Irwin, "Fracture;" pp. 551–590 in *Elast. Plast. / Elastizität und Plast.* Edited by S. Flügge. Springer Berlin Heidelberg, Berlin, Heidelberg, 1958.
- 46 M.- June, A.G. Evans, and A.H. Heuer, "Martensitic Transformations in Crack-Tip Stress Fields," **63** [5] 241–248 (1980).
- 47 W. Yan, C.H. Wang, X.P. Zhang, and Y.-W. Mai, "Effect of transformation volume contraction on the toughness of superelastic shape memory alloys," *Smart Mater. Struct.*, **11** [6] 947–955 (2002).
- 48 R.H.J. Hannink, P.M. Kelly, and B.C. Muddle, "Transformation Toughening in Zirconia-Containing Ceramics," *J. Am. Ceram. Soc.*, **83** [3] 461–487 (2000).
- 49 J. Rodel, "Interaction between crack deflection and crack bridging," *J. Eur. Ceram. Soc.*, **10** [3] 143–150 (1992).
- 50 B. Budiansky, J.C. Amazigo, and A.G. Evans, "Small-scale crack bridging and the fracture toughness of particulate-reinforced ceramics," *J. Mech. Phys. Solids*, **36** [2] 167–187 (1988).
- 51 G. Vekinis, M.F. Ashby, and P.W.R. Beaumont, "R-curve behaviour of Al₂O₃ ceramics," *Acta Metall. Mater.*, **38** [6] 1151–1162 (1990).
- 52 G.C. Wei and P.F. Becher, "Improvements in Mechanical Properties in SiC by the Addition of TiC Particles," *J. Am. Ceram. Soc.*, **67** [8] 571–574 (1984).

- 53 M.G. Jenkins, J.A. Salem, and S.G. Seshadri, "Fracture Resistance of a TiB₂ Particle / SiC Matrix Composite at Elevated Temperature," *J. Compos. Mater.*, **23** 77–91 (1989).
- 54 K.T. Faber and A.G. Evans, "Crack deflection processes-I. Theory," *Acta Metall.*, **31** [4] 565–576 (1983).
- 55 K.T. Fabert and A.G. Evans, "Crack Deflection Processes-II. Experiment," *Acta Metall.*, **31** [4] 165–76 (1983).
- 56 W. Kreher and W. Pompe, "Increased fracture toughness of ceramics by energy-dissipative mechanisms," *J. Mater. Sci.*, **16** 694–706 (1981).
- 57 N. Tessier-Doyen, J.C. Glandus, and M. Huger, "Untypical Young's modulus evolution of model refractories at high temperature," *J. Eur. Ceram. Soc.*, **26** [3] 289–295 (2006).
- 58 M. Taya, S. Hayashi, A.S. Kobayashi, and H.S. Yoon, "Toughening of a Particulate-Reinforced Ceramic-Matrix Composite by Thermal Residual Stress," *J. Am. Ceram. Soc.*, **73** [5] 1382–1391 (1990).
- 59 T. Hahn (ed.), *International Tables for Crystallography*, 5th ed. Springer, Dordrecht, The Netherlands, 2005.
- 60 V.T. Gritsyna, I. V Afanasyev-Charkin, V. a Kobayakov, and K.E. Sickafus, "Structure and electronic states of defects in spinel of different compositions MgO·nAl₂O₃:Me," *J. Am. Ceram. Soc.*, **82** [12] 3365–3373 (1999).
- 61 R. Sheldon, T. Hartmann, K. Sickafus, A. Ibarra, B. Scott, D. Argyriou, A. Larson, and R. Von Dreele, "Cation Disorder and Vacancy Distribution in," *J. Am. Ceram. Soc.*, **82** [12] 3293–3298 (1999).
- 62 S.T. Murphy, C.A. Gilbert, R. Smith, T.E. Mitchell, and R.W. Grimes, "Non-stoichiometry in MgAl₂O₄ spinel," *Philos. Mag.*, **90** [10] 1297–1305 (2010).
- 63 K.P.R. Reddy and A.R. Cooper, "Oxygen diffusion in magnesium aluminate spinel," *J. Am. Ceram. Soc.*, **64** [6] 368–371 (1981).
- 64 C.-J. Ting and H.-Y. Lu, "Defect Reactions and the Controlling Mechanism in the Sintering of Magnesium Aluminate Spinel," *J. Am. Ceram. Soc.*, **82** [4] 841–848 (1999).
- 65 C.-J. Ting and H.-Y. Lu, "Deterioration in the Final-Stage Sintering of Magnesium Aluminate Spinel," *J. Am. Ceram. Soc.*, **83** [7] 1592–1598 (2000).
- 66 Y. Okuyama, N. Kurita, and N. Fukatsu, "Defect structure of alumina-rich nonstoichiometric magnesium aluminate spinel," *Solid State Ionics*, **177** [1–2] 59–64 (2006).

- 67 B. Hallstedt, "Thermodynamic Assessment of the System MgO-Al₂O₃," *J. Am. Ceram. Soc.*, **75** [6] 1497–1507 (1992).
- 68 D.R. Gaskell, *Introduction to the Thermodynamics of Materials*, 4th ed. Taylor and Francis, New York, NY, 2003.
- 69 D.A. Porter and K.E. Easterling, "Chapter 1: Thermodynamics and Phase Diagrams;" pp. 1–59 in *Phase Transform. Met. Alloy*. T. J. Press, Padstow, England, 1981.
- 70 R. Abbaschian, L. Abbaschian, and R.E. Reed-Hill, "Chapter 15: Nucleation and Growth Kinetics;" pp. 463–497 in *Phys. Metall. Princ.*, 4th ed. Edited by H. Gowans and J. Dinsmore. Cengage Learning, Stamford CT, 209AD.
- 71 R.W. Balluffi, S.M. Allen, and W.C. Carter, "Chapter 17: General Features of Phase Transformations;" pp. 419–431 in *Kinet. Mater.*, 1st ed. Edited by R.A. Kemper. John Wiley and Sons, Hoboken, NJ, 2005.
- 72 R.W. Balluffi, S.M. Allen, and W.C. Carter, "Chapter 18: Spinodal and Order-Disorder Transformation;" pp. 433–458 in *Kinet. Mater.*, 1st ed. Edited by R.A. Kemper. John Wiley and Sons, Hoboken, NJ, 2005.
- 73 R.W. Balluffi, S.M. Allen, and W.C. Carter, "Chapter 19: Nucleation;" pp. 459–499 in *Kinet. Mater.*, 1st ed. Hoboken, NJ, 2005.
- 74 R.W. Balluffi, S.M. Allen, and W.C. Carter, "Chapter 20: Growth of Phases in Concentration and Thermal Fields;" pp. 501–532 in *Kinet. Mater.*, 1st ed. Edited by R.A. Kemper. John Wiley and Sons, Hoboken, NJ, 2005.
- 75 T.B. Reed, *Free Energy of Formation of Binary Compounds: An Atlas of Charts for High-Temperature Chemical Calculations*, First. The MIT Press, Cambridge, MA, 1971.
- 76 M.H. Lewis, "Precipitation in non-stoichiometric spinel crystals," *Philos. Mag.*, **20** 958–998 (1969).
- 77 G.K. Bansal and A.H. Heuer, "Precipitation in nonstoichiometric magnesium aluminate spinel," *Philos. Mag.*, **29** [4] 709–722 (1974).
- 78 P.C. Panda and R. Raj, "Kinetics of Precipitation of α -Al₂O₃ in Polycrystalline Supersaturated MgO•2Al₂O₃ Spinel Solid Solution," *J. Am. Ceram. Soc.*, **69** [5] 365–73 (1986).
- 79 K. Ando and Y. Oishi, "Self-diffusion coefficients of oxygen ion in single crystals of MgO•nAl₂O₃ spinels," *J. Chem. Phys.*, **61** [2] 625 (1974).
- 80 K. Ando and Y. Oishi, "Oxygen diffusion in MgO-Al₂O₃ spinel enhanced by phase boundaries with precipitated corundum," *J. Ceram. Assoc. Japan*, **83** [8] 417–418 (1975).

- ⁸¹ Y. Oishi and K. Ando, "Self-diffusion of oxygen in polycrystalline MgAl₂O₄," *J. Chem. Phys.*, **376** [1975] 1973–1976 (1975).
- ⁸² H.B. Aaron and G.R. Kotler, "Second Phase Dissolution," *Metall. Trans.*, **2** [2] 393–408 (1971).

CHAPTER 3
DIFFUSION LIMITED PRECIPITATION OF ALUMINA IN
MAGNESIUM ALUMINATE SPINEL

Modified from a paper published in The Journal of the American Ceramic Society (2016)

DOI 10.1111/jace.14619, 2016

J. Aaron Miller, Ivar E. Reimanis, Weiguo Miao, Anthony C. Sutorik

3.1 Abstract

Precipitation of Al_2O_3 from non-stoichiometric, dense spinel was examined with the intent to design strengthened transparent ceramics. Powders of magnesium aluminate spinel, $\text{MgO}\cdot n\text{Al}_2\text{O}_3$, with compositions $n = 1$ and $n = 2$ were uniaxially hot pressed at 1873 K, hot isostatically pressed at 2073 K and heat treated in air or vacuum at 1573 K for 1, 5, 10, 15, and 20 hours. It was observed that precipitation of $\alpha\text{-Al}_2\text{O}_3$ in $n = 2$ material initiated from the surface and progressed to various depths, with greater depths corresponding to treatments in air. The kinetics are shown to be limited by the diffusion of oxygen through the reacted layer. The results reveal that the environment used to densify spinel has a large influence on the evolution of the two phase microstructure during subsequent heat treatment.

3.2 Introduction

Magnesium aluminate spinel has long been a material of interest because of its broad transmission window from approximately 200 nm to 6000 nm, making it a candidate material for a host of applications including infrared domes and missile windows, transparent armor, space shuttle windows, optical lenses and laser host materials¹⁻⁶. Within this range, inline transmission

values (ILT) between 75-85% have been reported⁶, which approach the theoretical maximum of 87% transmission for spinel without anti-reflective coating¹. Furthermore, spinel has an advantage over other competing materials as it can be processed as a polycrystalline material allowing for formation of complex shapes from powders⁷.

Spinel is the only single phase region within the MgO-Al₂O₃ phase diagram⁸, and the range of compositions over which this single, cubic phase is stable increases with increasing temperature. As such, spinel is often described as MgO•nAl₂O₃ where n = 1 is stoichiometric spinel and values of n < 1 and n > 1 refer to MgO-rich and Al₂O₃-rich spinel, respectively. For n > 1, some studies suggest that cation vacancies are created as excess Al³⁺ ions occupy Mg²⁺ tetrahedral sites⁹⁻¹². Other works claim that oxygen vacancies are also created¹³⁻¹⁵. The type and amount of defects present may depend on the densification method. For example, vacuum hot pressing in a graphite die, commonly used to remove gaseous impurities, creates an environment that promotes oxygen vacancies⁴. The coupling of intrinsic defects in non-stoichiometric spinel and the processing environment has not been examined.

Non-stoichiometric spinel is of interest since it may be a way to improve the strength and/or toughness via second phase precipitation,^{16,17} and it has been shown recently that compositions up to n = 2.5 can be produced with high transparency¹⁸. Previous studies with single crystals have shown that the precipitation of α-Al₂O₃ is preceded by the formation of intermediate phases¹⁹⁻²². Furthermore, precipitation was observed to occur only at free surfaces because of the lattice strain associated with volume contraction upon the formation of Al₂O₃ from the spinel matrix. In contrast, it was shown by Panda that precipitation from single phase, polycrystalline n = 2 material could occur throughout the bulk because creation of pores at grain boundaries compensated for volume contraction, and no intermediate precipitation phases were observed²³.

It should be noted that the densification parameters in Panda's study did not allow for the complete removal of porosity and impurities which is critical for creating transparent material²⁴.²⁵. Neither that work nor the work on single crystals explored how processing conditions typically needed for transparent spinel influence the evolution of precipitation. The present work explores the defect structure of Al₂O₃-rich spinel created by densification in low PO₂ environments and how precipitation of Al₂O₃ is affected.

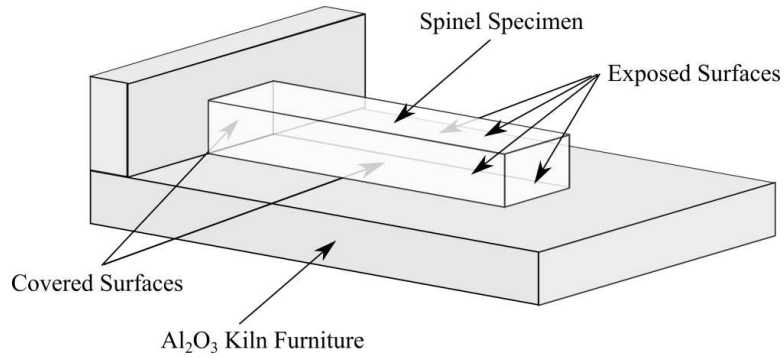
3.3 Experimental procedure

MgO•nAl₂O₃ powders of compositions n = 1.00 and n = 2.00, henceforth referred to as n = 1 and n = 2, were made by mixing Mg(OH)₂ and γ-Al₂O₃ powders in appropriate amounts and calcined to form material containing spinel and Al₂O₃ phases. Further details are provided elsewhere²⁶. Prior to hot pressing, the as-received powders were sieved through 58 mesh nylon screen to remove agglomerates that formed during transportation and storage. 20.4g of powder was loaded into a grafoil-lined circular carbon die with a diameter of 3.81 cm (1.5 in.). The material was then uniaxially hot pressed (Thermal Technologies 610G-25T) under a vacuum of 0.01 Pa (10⁻⁵ Torr) to 1873 K at 7 deg per minute. A pressure of 35 MPa was applied starting at 1473 K and held for 5 hours at 1873 K before unloading and naturally cooling. Post hot pressing, the pellets were polished with 68 grit SiC paper to remove all graphoil, then hot isostatically pressed (HIPed) by American Isostatic Pressing (Columbus, OH) to 2123 K and 207 MPa in an argon environment for 5 hours to further ensure single phase material was achieved and to remove porosity. The HIPed discs were ground to plane-parallel with a uniform thickness of 4 mm using a surface grinder with a 400 grit diamond wheel and then machined into chevron notch bars of dimensions 25.0 x 4.0 x 3.1 mm by Bomas Machining (Somerville Ma). As part of another study²⁷, the bars were fractured in accordance with ASTM standard C1421-10.

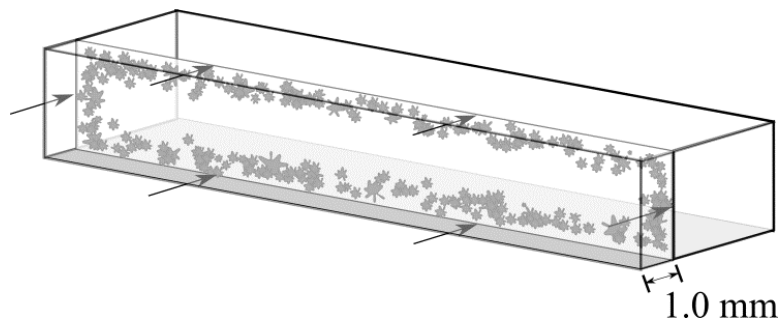
All specimens fractured into two pieces; one piece was then heat treated in atmosphere and the other was heat treated in vacuum for this study.

To examine the kinetics of precipitation, one set of specimens was heat treated at temperatures within the two-phase region for $n = 2$ spinel by heating specimens at 7 deg per minute to 1573 K for 1, 5, 10, 15, and 20 hours. To demonstrate the ability to control the location of precipitation, a separate specimen was heat treated in air within the single-phase region at 1873 K for 24 hours in order to restore oxygen to the spinel matrix. This specimen was then heat treated at 1573 K in vacuum for 10 hours. This specimen will henceforth be referred to as the restored specimen. Heat treatments in air were carried out using a drop down furnace (Deltech DT/31/RS/BHW) and vacuum heat treatments were done at 0.01 Pa using the same hot press as in the processing, but with no load applied. Specimens for all heat treatments were placed on high-purity Al_2O_3 kiln furniture with the bottom and end faces of the rectangular specimen in direct contact with the furniture, as shown in Figure 3.1 A. Post heat treatment, 1.0 mm of material was removed to reveal a length-wise cross section perpendicular to the top and bottom and polished down to 1 μm diamond finish, as shown in Figure 3.1 B.

Energy dispersive spectroscopy (EDS) and x-ray diffraction (Phillips X'Pert Pro) were used to identify the phases present, and scanning electron microscopy (JEOL JSM-7000F) was used to evaluate the microstructure. Optical microscopy of the polished cross section surfaces (Leco Olympus PMG3) was used to measure the advancement of Al_2O_3 precipitation from the surface of the material into the bulk. The distance from the exposed or covered surface to the leading edge of the precipitation front was measured every 500 μm for the length of the specimen, providing a minimum of 25 measurements for each data point.



(A)



(B)

Figure 3.1 A spinel test specimen on high purity Al₂O₃ kiln furniture used for heat treatments is shown. The bottom and end surface of the specimen were in intimate contact with the furniture, while the remaining surfaces are exposed to the atmosphere of the furnace. These are referred to as covered and exposed surfaces, respectively (A). Post heat treatment the specimen was cross sectioned perpendicular to the top and bottom and polished to reveal the depth of Al₂O₃ precipitation where arrows indicated the direction of material removal (B).

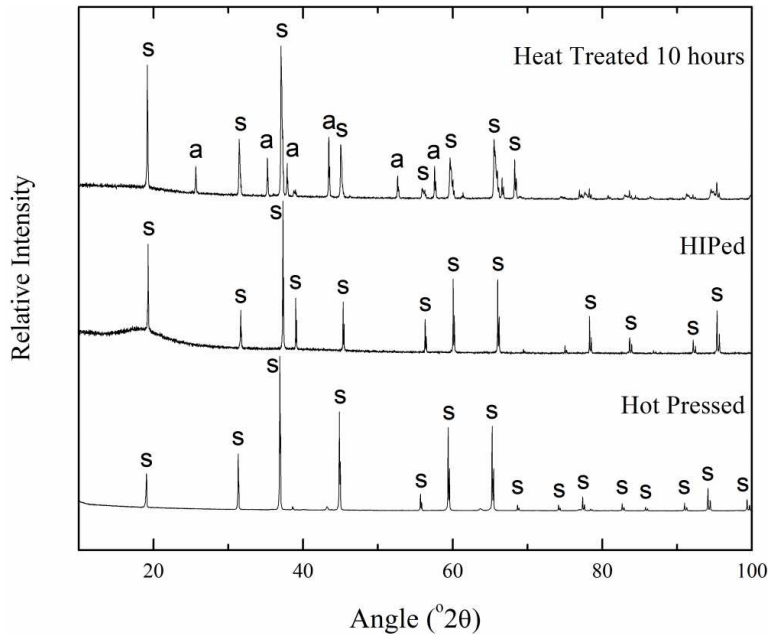


Figure 3.2 XRD spectra for $n = 2$ material after hot pressing, HIPing, and heat treating for 10 hours in air are shown. After hot pressing and HIPing, only spinel (S) was present. The heat treatment led to the appearance of α - Al_2O_3 peaks (a).

3.4 Results

Upon HIPing, the $n = 1$ material was fully dense and visibly transparent, but cloudy. Cloudiness vanished after 5 hours of heat treatment in either air or vacuum, and no precipitation was observed for the $n = 1$ material for any length of heat treatment. The $n = 2$ material was also fully dense after HIPing, but only visibly translucent and light gray in color, which persisted regardless of heat treatment. Note that high optical transmission is not the major focus of this study, as sintering aids which promote transparent spinel during hot pressing such as LiF were not added so as to not complicate the investigation of transport phenomena. X-ray diffraction (XRD) of the $n = 2$ material confirms that single phase spinel was present after densification and α - Al_2O_3 precipitated during heat treatment, as shown in Figure 3.2. Precipitation in the $n = 2$ material was first observed at the surface where EDS revealed that the precipitates were rich in

Al and contained O, but that Mg was not present. Figure 3.3 shows a representative EDS map for $n = 2$ material heat treated in air.

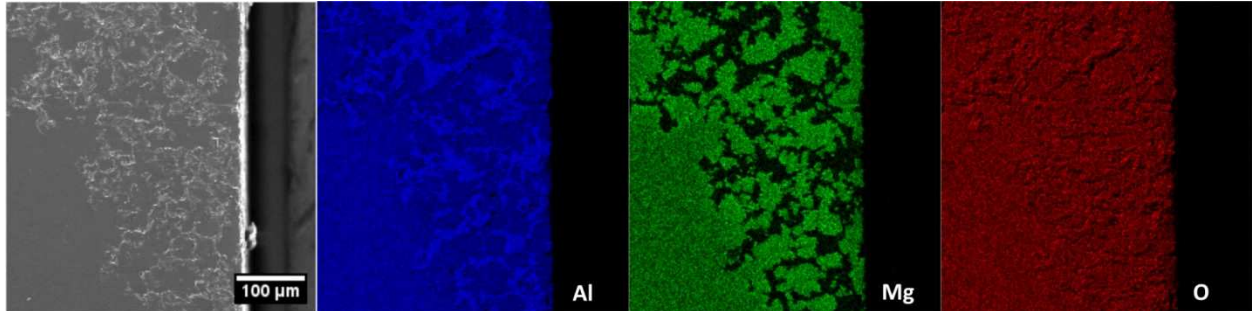


Figure 3.3 SEM and corresponding EDS mapping of Al, Mg, and O is shown for a cross section of $n = 2$ material heat treated for 10 hours in air. The right side is the surface that was exposed to air. A growth front of Al_2O_3 is apparent.

For the $n = 2$ material heat treated in air, precipitation was first observed at the surface after 5 hours. After 10 hours, a uniform precipitation front had been established at both the exposed and covered surface (Figure 3.1), although the depth of the reaction front was measured to be $160 \mu\text{m}$ from the exposed surface but only $25 \mu\text{m}$ from the covered surface. Beyond 10 hours, the front from both exposed and covered surfaces proceeded inward through the bulk at linear rates as described below. The resulting microstructures for heat treatment of $n = 2$ spinel in air are shown in Figure 3.4. Specimens heat treated in vacuum showed a similar trend of precipitation occurring first at the surface then proceeding inwards, although the depth of the precipitation front was much less for the same heat treatment times, as shown in Figure 3.5. After 10 hours, the depth of the precipitation front of the specimen treated in vacuum was measured to be $50 \mu\text{m}$ and $70 \mu\text{m}$ from the exposed and covered surfaces, respectively. The depths of the precipitation front as a function of atmosphere and time for the $n = 2$ specimens heat treated in air and in vacuum are shown in Figure 3.6.

Precipitation was also observed in the restored specimen. However, the majority of the precipitation occurred at the core of the specimen with very little precipitation observed at the surface, as shown in Figure 3.7. The differences in precipitation process are attributed to controlling the presence of oxygen, as discussed in the following section.

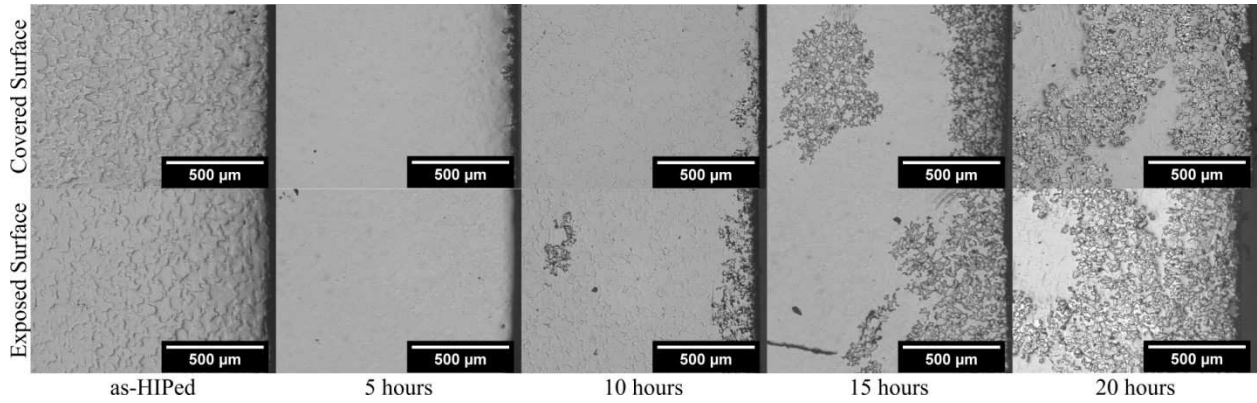


Figure 3.4 Optical micrographs showing the progression of precipitation of $\alpha\text{-Al}_2\text{O}_3$ from the surface inwards in $n = 2$ spinel during heat treatment in air are shown. Isolated surface precipitation was first observed after heat treating for 5 hours. After 20 hours, a uniform precipitation front had reached a depth of approximately $820\ \mu\text{m}$.

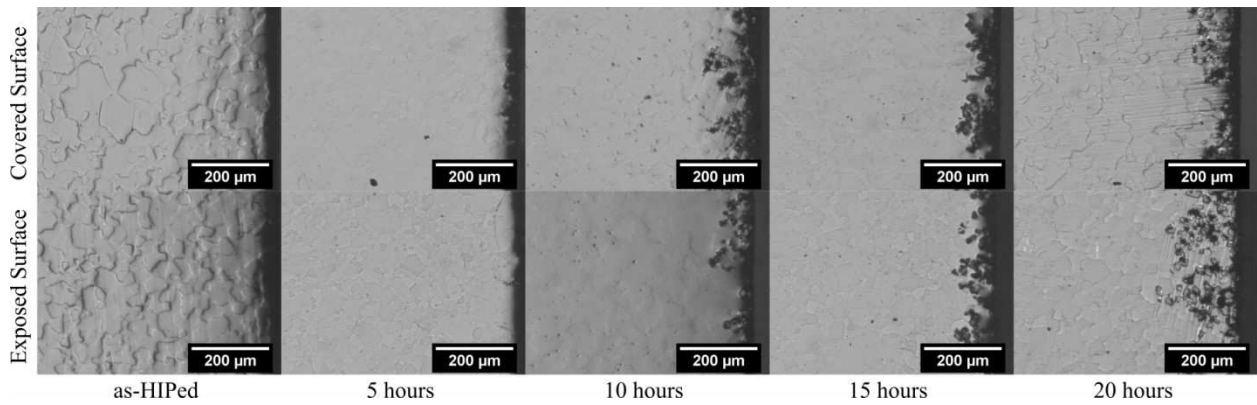


Figure 3.5 Optical micrographs showing the progression of precipitation of $\alpha\text{-Al}_2\text{O}_3$ from the surface in towards the bulk in $n = 2$ spinel during heat treatment in vacuum are shown. After 20 hours, the precipitation front had reached a depth of approximately $120\ \mu\text{m}$. Note that the magnification is increased when compared to Figure 3.4 to better show the precipitated region.

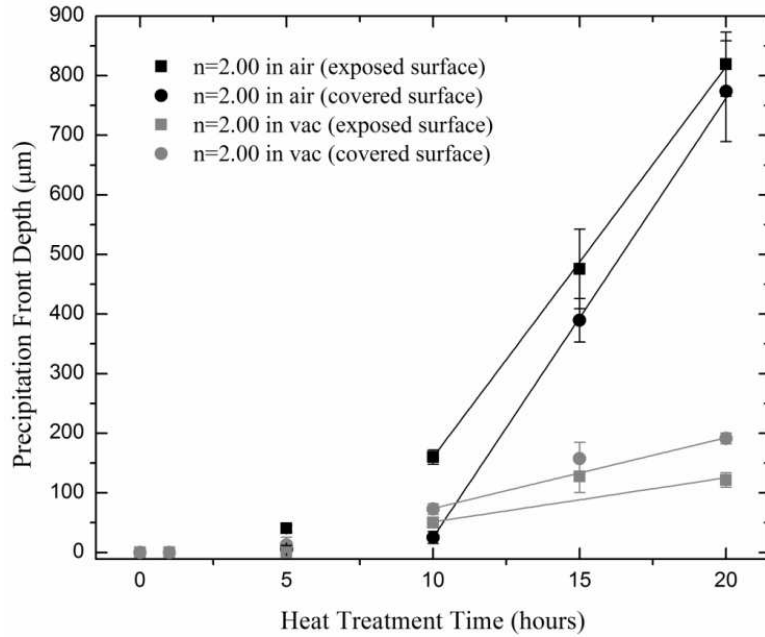
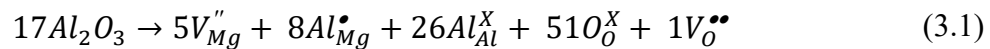


Figure 3.6 The depth of the Al_2O_3 precipitation front in $n = 2$ material from various surfaces is shown as a function of heat treatment time and atmosphere. Precipitation appeared to follow a linear trend with time after a uniform surface layer was developed after 10 hours heat treatment. The as-HIPed material is shown as 0 hours heat treatment. Covered surface refers to the faces of the specimen in direct contact with the kiln furniture, while exposed surface refers to the faces of the specimen open to the atmosphere of the heat treatment.

3.5 Discussion

Based on the composition dependence of density for single phase, Al-rich spinel densified in air, Okuyama¹³ proposed that excess Al_2O_3 was incorporated into the spinel matrix according to the Kroger-Vink defect reaction

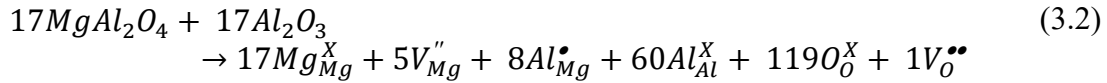


where increasing the matrix composition by 17 units of Al_2O_3 expands the spinel lattice by 13 units by placing 8 Al ions on Mg sites and creating 5 Mg vacancies and 1 O vacancy to maintain charge balance. The lattice has thus expanded by 13 Mg sites, 26 Al sites, and 52 O sites while maintaining the spinel structure. To create $n = 2$ material, the defected structure shown in



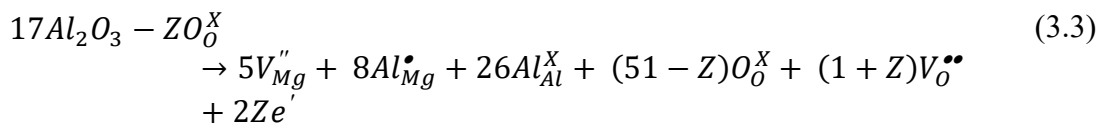
Figure 3.7 Polished cross sections of two specimens are shown. Material that was HIPed, then heat treated in air at 1573 K for 10 hours (left) is compared to material that was HIPed, then heat treated in air at 1873 K for 24 hours, then heat treated in vacuum at 1573 K for 10 hours (right), demonstrating that precipitation can occur at the surface or at the core depending on processing conditions.

equation (3.1) would be combined with 17 units of $n = 1$ spinel to create 30 units of $n = 2$ spinel described by



where the spinel structure is again maintained with an overall organization of 30 Mg sites, 60 Al sites, and 120 O sites. During heat treatment in air or in vacuum, material of this structure would be expected to precipitate back into 17 units of $n = 1$ spinel and 17 units of Al_2O_3 . However, the observation that the precipitation front advanced approximately 4 times further in air than in vacuum over the entire range of time investigated indicates that the presence of excess oxygen plays a key role in precipitation of $\alpha-Al_2O_3$ in spinel. Furthermore, the observation that a precipitation front moves from the surface to the interior of the specimen indicates that oxygen is being supplied from the environment and dictates the precipitation kinetics.

It is noteworthy that reducing environments similar to what the specimens were exposed to during densification in this study have been shown to create relatively high concentrations of oxygen vacancies in Al-rich spinel⁴. It is thus clear that the presence of these oxygen vacancies extends the phase stability of Al-spinel and that oxygen must be restored to the structure prior to complete precipitation of all excess Al_2O_3 . This suggests a modified defect reaction for material densified in low PO_2 environments



where Z is dependent on the oxygen vacancy concentration as determined by the PO_2 during

densification.

It is logical to assume that precipitation first occurs at isolated, energetically favorable sites at the surface where oxygen was readily available from the atmosphere. Precipitation would continue along free surfaces first, and then into the bulk once a uniform surface layer had formed, consistent with observations in this study (Figure 3.4 and Figure 3.5). As this reaction layer penetrates into the bulk, it is expected that pores would form due to the volume change as denser $\alpha\text{-Al}_2\text{O}_3$ precipitates from spinel, as observed by Panda and shown in Figure 3.8 in this study. The reaction front proceeds into the bulk at a linear rate with time, indicating rapid diffusion of oxygen to the reaction front. This rapid diffusion is likely due to the porosity and phase boundary disorder created during precipitation. Because oxygen has to diffuse through an increasingly thick precipitated region with time, it is possible that the rate of advancement would eventually deviate from a linearity, similar to the Deal-Grove model for oxidation of silicon²⁸. However, this was not observed for the heat treatment times used in this study. Rather, the linear trend with time matches results observed by Donlon,¹⁹ who observed precipitation of $\alpha\text{-Al}_2\text{O}_3$ similar to autocatalytic, discontinuous precipitation reactions observed in metallic alloy systems²⁹ where disorder at grain boundaries enhances the mobility of defects, such as oxygen vacancies, allowing the formation of incoherent precipitates from the host structure.

The linear portion of the front advancement may best be modeled by the mean squared displacement of an atom diffusing in 3 dimensions by random walk³⁰

$$\langle r^2 \rangle = \frac{6Dt}{f} \quad (3.4)$$

where r is the mean distance an atom or vacancy has traveled from an initial reference point, D is the diffusivity, t is time, and f is the correlation factor accounting for already occupied

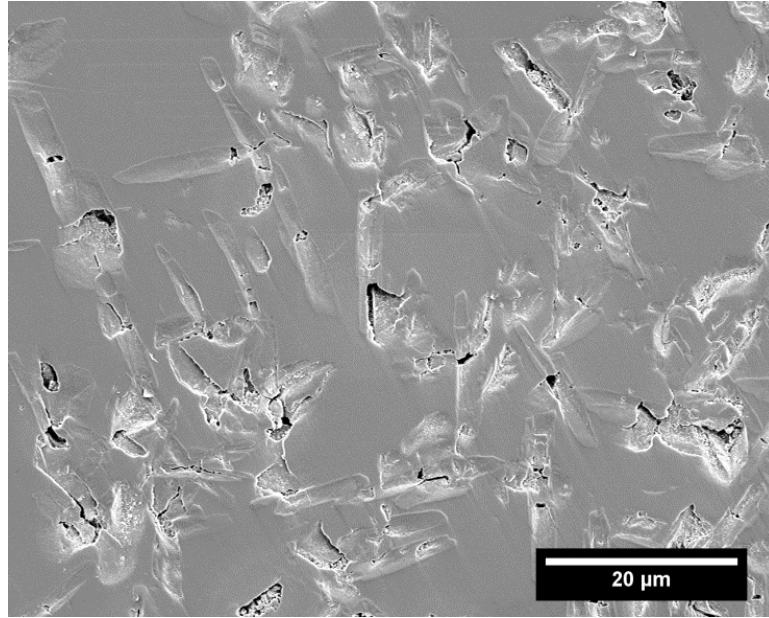


Figure 3.8 SEM micrograph of precipitated region displaying porosity formed as a result of volume contraction during precipitation. This porosity and enhanced disorder at phase boundaries help to explain the rapid diffusion and linear trend observed in the advancement of the precipitation front.

sites. Diffusivities for oxygen in magnesium aluminate spinel extrapolated to 1573 K range from $1.75 \times 10^{-20} \text{ m}^2/\text{s}$ to $1.19 \times 10^{-18} \text{ m}^2/\text{s}$ for stoichiometric ($n = 1$) and Al_2O_3 rich ($n = 2$) single crystals, respectively^{14,31}, while diffusivities as high as $6.23 \times 10^{-15} \text{ m}^2/\text{s}$ have been measured in polycrystalline alumina-spinel composites which exhibit enhanced oxygen diffusion at disordered phase boundaries³². Using this largest diffusivity value and a correlation factor of 0.85 for self diffusion in an FCC lattice³⁰ results in a mean distance of 56 μm after 20 hours, which is within an order of magnitude of the reaction depth measured for air heat treatments.

In Figure 3.6, similar slopes are shown for the depth of the reaction front measured from the exposed and covered surfaces of the material heat treated in air, indicating that the precipitation front proceeded at a similar rate once established. After 10 hours the reaction front had reached a depth of 160 μm from the surface exposed to air, but only a depth of 25 μm from

the surface in intimate contact with the Al_2O_3 kiln furniture. The discrepancy in depth despite the similar reaction rate reveals that an incubation time (approximately 2.5 hours in the present case) is required for the covered surface compared to the exposed surface. Therefore, the presence of Al_2O_3 kiln furniture introduces an additional energy barrier to precipitation, likely by delaying oxygen transfer to the surface of the material. Once oxygen reaches the surface, it diffuses into the bulk at the same rate as oxygen diffusion into the exposed surfaces. The opposite trend was observed in vacuum, although to a much lesser degree. Namely, there was a slight incubation time observed for the exposed surface compared to the covered surface. In this case, the furniture is no longer a barrier to oxygen transfer compared to the exposed surfaces because there is little oxygen present at the exposed surfaces in the vacuum.

In the case of the restored specimen, the 24 hour heat treatment at 1873 K in air allowed oxygen diffusion into the specimen. However, single-phase spinel is stable at this temperature, preventing precipitation. Upon subsequent heat treatment within the two-phase region at 1573 K, precipitation was observed. However, as this heat treatment was performed in vacuum, oxygen was simultaneously diffusing out of the material, creating a stable, single phase, non-stoichiometric matrix similar to the as-HIPed material. Therefore, precipitation could not occur at the oxygen-deficient surfaces but was able to occur within the bulk where oxygen was still present.

The observation that $\alpha\text{-Al}_2\text{O}_3$ precipitates directionally from surfaces when heat treated in vacuum may seem unusual since the vacuum environment provides too little oxygen. Specifically, the amount of oxygen present in the vacuum environment ($\sim 1.6 \times 10^{-7}$ mol/m³) is well below that needed to precipitate the amount of Al_2O_3 observed after 20 hours, given the size of the chamber used in this experiment (approximately 1 m³). Instead, the cause of precipitation

arises due to the volatility of MgO under vacuum. Past work has shown that densification of spinel in reducing atmospheres, especially in the presence of carbon dies used for hot pressing, causes volatilization of MgO from the surface^{33,34}. Removing MgO from a region already rich in Al₂O₃ further increases the driving force for precipitation, promoting the precipitation observed in the n = 2 material heat treated in vacuum. Recall that no precipitation was observed in the n = 1 material processed in the same manner, indicating that MgO volatilization alone did not provide enough driving force for Al₂O₃ precipitation in stoichiometric material. Further precipitation in the n = 2 material is limited by the oxygen deficiency within the structure and thus only limited precipitation was observed for n = 2 specimens heat treated in vacuum because oxygen was never restored to the structure.

3.6 Conclusions

Alumina-rich n = 2 material was oxygen deficient following densification via hot pressing and HIPing in reducing environments, and therefore the resulting microstructure from subsequent heat treatments was dependent on the atmosphere present. Heat treatments in vacuum resulted in MgO volatilization, leading to precipitation, but limited to a relatively small surface region. Precipitation in specimens heat treated in air was enhanced due to diffusion of oxygen into the structure, resulting in a precipitation layer advancing from the surface into the bulk. Restoring oxygen by heat treating in air within the single phase temperature region prior to heat treatment in the two phase region under vacuum allowed for precipitation at the core rather than at the surface. Understanding this enables the design of precipitation strengthened transparent spinel by suggesting methods to control the amount and location of second phase Al₂O₃.

3.7 Acknowledgements

This work was made possible through funding from Corning Incorporated.

3.8 References

- ¹ D.C. Harris, *Materials for Infrared Windows and Domes: Properties and Performance*. SPIE- The International Society for Optical Engineering, Bellingham, Washington, 1999.
- ² D.C. Harris, "History and development of polycrystalline optical spinel in the U.S.;" pp. 1–22 in *Wind. Dome Technol. Mater.* Edited by R. W. Tustison. SPIE- The International Society for Optical Engineering, Orlando, 2005.
- ³ J.A. Salem, "Transparent armor ceramics as spacecraft windows," *J. Am. Ceram. Soc.*, **96** [1] 281–289 (2013).
- ⁴ M. Rubat Du Merac, H.J. Kleebe, M.M. Muller, and I.E. Reimanis, "Fifty years of research and development coming to fruition; Unraveling the complex interactions during processing of transparent magnesium aluminate (MgAl_2O_4) spinel," *J. Am. Ceram. Soc.*, **96** [11] 3341–3365 (2013).
- ⁵ I. Reimanis and H.-J. Kleebe, "A Review on the Sintering and Microstructure Development of Transparent Spinel (MgAl_2O_4)," *J. Am. Ceram. Soc.*, **92** [7] 1472–1480 (2009).
- ⁶ A. Goldstein, "Correlation between MgAl_2O_4 -spinel structure, processing factors and functional properties of transparent parts (progress review)," *J. Eur. Ceram. Soc.*, **32** [11] 2869–2886 (2012).
- ⁷ A.A. DiGiovanni, L. Fehrenbacher, and D.W. Roy, "Hard Domes and Windows from Magnesium Aluminate Spinel;" pp. 56–63 in *Wind. Dome Technol. Mater.* Edited by R.W. Tustison. SPIE- The International Society for Optical Engineering, Orlando, 2005.
- ⁸ B. Hallstedt, "Thermodynamic Assessment of the System $\text{MgO-Al}_2\text{O}_3$," *J. Am. Ceram. Soc.*, **75** [6] 1497–1507 (1992).
- ⁹ K. Sickafus and J. Wills, "Structure of spinel," *J. Am. Ceram. Soc.*, **82** [12] 3279–3292 (1999).
- ¹⁰ V.T. Gritsyna, I. V Afanasyev-Charkin, V. a Kobayakov, and K.E. Sickafus, "Structure and electronic states of defects in spinel of different compositions $\text{MgO} \cdot n\text{Al}_2\text{O}_3 \cdot \text{Me}$," *J. Am. Ceram. Soc.*, **82** [12] 3365–3373 (1999).

- 11 R. Sheldon, T. Hartmann, K. Sickafus, A. Ibarra, B. Scott, D. Argyriou, A. Larson, and R. Von Dreele, "Cation Disorder and Vacancy Distribution in," *J. Am. Ceram. Soc.*, **82** [12] 3293–3298 (1999).
- 12 S.T. Murphy, C.A. Gilbert, R. Smith, T.E. Mitchell, and R.W. Grimes, "Non-stoichiometry in MgAl₂O₄ spinel," *Philos. Mag.*, **90** [10] 1297–1305 (2010).
- 13 Y. Okuyama, N. Kurita, and N. Fukatsu, "Defect structure of alumina-rich nonstoichiometric magnesium aluminate spinel," *Solid State Ionics*, **177** [1-2] 59–64 (2006).
- 14 K.P.R. Reddy and A.R. Cooper, "Oxygen diffusion in magnesium aluminate spinel," *J. Am. Ceram. Soc.*, **64** [6] 368–371 (1981).
- 15 C.-J. Ting and H.-Y. Lu, "Defect Reactions and the Controlling Mechanism in the Sintering of Magnesium Aluminate Spinel," *J. Am. Ceram. Soc.*, **82** [4] 841–848 (1999).
- 16 C.B. Huang, T.C. Lu, L. Bin Lin, M.Y. Lei, and C.X. Huang, "A Study on Toughening and Strengthening of Mg-Al Spinel Transparent Ceramics," *Key Eng. Mater.*, **336-338** 1207–1210 (2007).
- 17 D.J. Green, *An introduction to the mechanical properties of ceramics*, First. Press Syndicate of The University of Cambridge, Cambridge, 1998.
- 18 K. Waetzig and A. Krell, "The Effect of Composition on the Optical Properties and Hardness of Transparent Al-rich MgO·nAl₂O₃ Spinel Ceramics," *J. Am. Ceram. Soc.*, **99** [3] 946–953 (2016).
- 19 W.T. Donlon, T.E. Mitchell, and A.H. Heuer, "Precipitation in non-stoichiometric spinel," *J. Mater. Sci.*, **17** 1389–1397 (1982).
- 20 N. Doukhan, J.C. Doukhan, and B. Escaig, "T.E.M. Study of High Temperature Precipitation in (Al₂O₃)_n MgO Spinel," *Mater. Res. Bull.*, **11** [2] 125–34 (1976).
- 21 M.H. Lewis, "Precipitation in non-stoichiometric spinel crystals," *Philos. Mag.*, **20** 958–998 (1969).
- 22 G.K. Bansal and A.H. Heuer, "Precipitation in nonstoichiometric magnesium aluminate spinel," *Philos. Mag.*, **29** [4] 709–722 (1974).
- 23 P.C. Panda and R. Raj, "Kinetics of Precipitation of α-Al₂O₃ in Polycrystalline Supersaturated MgO·2Al₂O₃ Spinel Solid Solution," *J. Am. Ceram. Soc.*, **69** [5] 365–73 (1986).

- 24 M. Rubat du Merac, I.E. Reimanis, C. Smith, H.J. Kleebe, and M.M. Müller, “Effect of Impurities and LiF Additive in Hot-Pressed Transparent Magnesium Aluminate Spinel,” *Int. J. Appl. Ceram. Technol.*, **48** 33–48 (2012).
- 25 I. Ganesh, “A review on magnesium aluminate (MgAl_2O_4) spinel: synthesis, processing and applications,” *Int. Mater. Rev.*, **58** [2] 63–112 (2012).
- 26 A.C. Sutorik, G. Gilde, J.J. Swab, C. Cooper, R. Gamble, and E. Shanholtz, “Transparent Solid Solution Magnesium Aluminate Spinel Polycrystalline Ceramic with the Alumina-Rich Composition $\text{MgO} \cdot 1.2 \text{Al}_2\text{O}_3$,” *J. Am. Ceram. Soc.*, **95** [2] 636–643 (2012).
- 27 J.A. Miller, I.E. Reimanis, W. Miao, A.C. Sutorik, and J.A. Salem, “Mechanical and Optical Properties in Precipitated Regions of Alumina-Rich Magnesium Aluminate Spinel,” *Int. J. Appl. Ceram. Technol.*, To Be Published (n.d.).
- 28 B.E. Deal and A.S. Grove, “General relationship for the thermal oxidation of silicon,” *J. Appl. Phys.*, **36** [12] 3770–3778 (1965).
- 29 E. Hornbogen, “Systematics of the Cellular Precipitation Reactions,” *Metall. Trans.*, **3** [November] 2717–2727 (1972).
- 30 R.W. Balluffi, S.M. Allen, and W.C. Carter, “Chapter 7: Atomic Models for Diffusion;” pp. 145–159 in *Kinet. Mater.*, 1st ed. John Wiley and Sons, Hoboken, NJ, 2005.
- 31 Y. Oishi and K. Ando, “Self-diffusion of oxygen in polycrystalline MgAl_2O_4 ,” *J. Chem. Phys.*, **376** [1975] 1973–1976 (1975).
- 32 K. Ando and Y. Oishi, “Oxygen diffusion in $\text{MgO-Al}_2\text{O}_3$ spinel enhanced by phase boundaries with precipitated corundum,” *J. Ceram. Assoc. Japan*, **83** [8] 417–418 (1975).
- 33 C.-J. Ting and H.-Y. Lu, “Deterioration in the Final-Stage Sintering of Magnesium Aluminate Spinel,” *J. Am. Ceram. Soc.*, **83** [7] 1592–1598 (2000).
- 34 M. Matsui, T. Takahashi, and I. Oda, “Influence of MgO vaporization on the final-stage sintering of $\text{MgO-Al}_2\text{O}_3$ spinel;” pp. 562–73 in *Adv. Ceram. Vol. 10, Struct. Prop. MgO Al₂O₃ Ceram.* Edited by W.D. Kingery. American Ceramic Society, Columbus, OH, 1984.

CHAPTER 4
MECHANICAL AND OPTICAL PROPERTIES IN PRECIPITATED REGIONS OF
ALUMINA-RICH MAGNESIUM ALUMINATE SPINEL

A paper Accepted by The International Journal of Applied Ceramic Technology (2016)

DOI 10.1111/ijac.12644

J. Aaron Miller, Ivar E. Reimanis, Weiguo Miao, Jonathan A. Salem

4.1 Abstract

The toughening and strengthening of transparent ceramics is challenging because microstructural alterations typically lead to light scattering. Here, controlled precipitation of α - Al_2O_3 from non-stoichiometric spinel is explored to demonstrate unique control over the evolution of second phase Al_2O_3 and how the microstructure might be altered to enhance fracture toughness while minimizing light scatter. Alumina-rich magnesium aluminate spinel, $\text{MgO}\cdot n\text{Al}_2\text{O}_3$, where $n = 2$, was hot pressed and HIPed to produce fully dense, single phase material. The material was then heat treated in air at 1573 K for up to 20 hours to create a two-phase spinel- Al_2O_3 composite. The fracture toughness varies from 0.88 - 2.47 $\text{MPa}\sqrt{\text{m}}$ depending on the microstructure; enhanced toughness at the surface was due to increased crack tortuosity at phase boundaries, but residual tensile stresses were observed in the interior of the material. Precipitation causes local volume contraction and the formation of porosity, decreasing optical transmission, especially for heat treatment times longer than 5 hours¹.

4.2 Introduction

Magnesium aluminate spinel has been studied extensively because of its desirable combination of chemical and thermal stability, mechanical robustness, and transparency to large portions of the visible and infrared spectrum, creating the potential for this material to be used in applications including refractory material,^{1,2} transparent armor,³ missile radomes⁴, and space craft windows⁵. High hardness and fracture toughness are desirable for such applications, influencing the direction of much of the research in recent years. Specifically, the influence of varied stoichiometry on the mechanical properties of spinel has been of interest.

Spinel is the only single phase region in the MgO-Al₂O₃ phase diagram⁶ besides the end members, and the compositional range over which spinel remains stable increases with increasing temperature. Written as MgO•nAl₂O₃, single phase spinel exists from n = 0.8 (MgO rich), to n = 3.5 (Al₂O₃ rich)⁷.

When compared to the Knoop hardness of stoichiometric spinel (12.2 GPa), works by Krell⁸ and Sutorik^{9,10} observed little change for Al-rich compositions up to n = 1.5 (12.3 GPa) followed by a significant decrease for compositions up to n = 2.5 (11.0 GPa), indicating that stoichiometry affects the mechanical properties of single phase spinel. Dericioğlu¹¹ demonstrated increasing indentation fracture toughness from 1.47 – 1.79 MPa√m to 1.65 – 2.21 MPa√m as stoichiometry increased from n = 1 to n = 2 for various applied loads, although a minimum fracture toughness of 1.18 – 1.34 MPa√m was observed for n = 1.5 spinel. An extended list of experimental toughness values from literature is summarized by DuMerac¹², concluding that typical fracture toughness values for stoichiometric, single phase spinel ranges from 1.1 – 2.2 MPa√m and that the addition of excess Al₂O₃ has resulted in both superior and inferior mechanical performance. Figure 4.1 and Figure 4.2 summarize experimental hardness

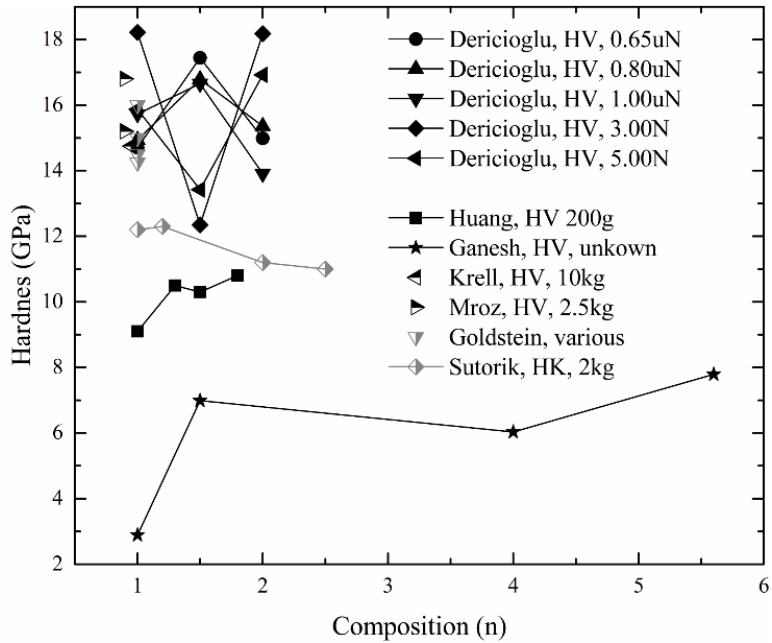


Figure 4.1 Experimental hardness values for single phase magnesium aluminate spinel are shown for varied compositions. Values from Vickers hardness are shown in black while other techniques are shown in grey.

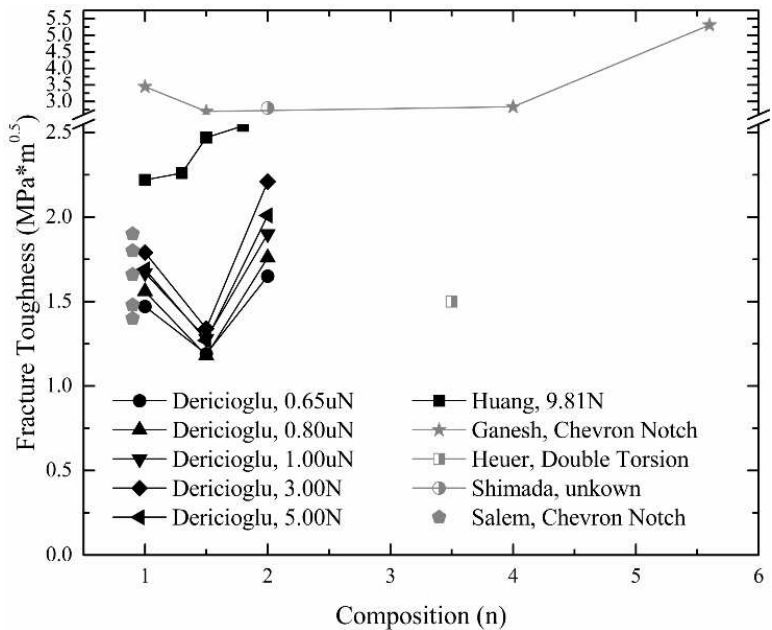


Figure 4.2 Experimental toughness values for single phase magnesium aluminate spinel are shown for varied compositions. Values from indentation toughness are shown in black while other techniques are shown in grey.

and fracture toughness data, respectively, found in literature^{5, 8, 9, 11, 13–18}.

The above studies utilize the wide composition range of spinel to vary the stoichiometry and alter the mechanical properties while maintaining single phase material in order to avoid light scattering by a second phase. While transparency is a critical consideration for optical applications, limiting potential material systems to a single phase precludes toughening mechanisms that are active in two-phase systems. Enhanced fracture toughness has been observed in spinel¹³ and other material systems^{19, 20} because the presence of a second phase has been shown to alter crack propagation via mechanisms such as crack deflection¹⁵ or bridging^{21, 22}. Additionally, the thermal expansion mismatch between the matrix phase and the particulate has been shown to modify toughness through the introduction of tensile and compressive stresses,^{23, 24} further indicating that there is potential to improve the fracture toughness of spinel through the introduction of a second phase. However, in order to exploit any potential mechanical benefits from the presence of a second phase, the phase must be incorporated into the matrix in such a way that the final microstructure does not deter the optical properties of the new composite material.

The restrictions imposed by the optical requirements may limit the choices for second phase materials, but both MgO and Al₂O₃ are potential candidates because both have been produced as transparent materials^{3, 25–27}, and the refractive indices of MgO, Al₂O₃, and spinel are similar for wavelengths from approximately 0.4 – 5 μm²⁸, meaning that light scatter at phase boundaries would be minimal, especially if the final grain size is approximately an order of magnitude smaller than the wavelength of interest²⁹ and porosity within the material is minimized. Furthermore, because of the increased solubility of both MgO and Al₂O₃ into spinel at higher temperatures, there is potential for exceptional control over the evolution of the two-phase

microstructure by controlled precipitation at lower processing temperatures. As indicated by the phase diagram, Al_2O_3 is more soluble in spinel than MgO , and thus Al_2O_3 precipitation from Al-rich spinel has been studied more extensively than MgO precipitation³⁰⁻³⁴. The kinetics of Al_2O_3 precipitation from Al-rich spinel is dictated by the restoration of oxygen from the atmosphere during heat treatment in air³⁸, and therefore, it is possible to design particular two-phase microstructures. The mechanical behavior of these microstructures are not known. The goal of the work presented here is to evaluate the potential improvements to the mechanical properties of spinel, specifically fracture toughness, that might be attained through the addition of second phase Al_2O_3 . Consideration is also given to the effects on the optical properties.

4.3 Experimental procedure

$\text{MgO}\cdot n\text{Al}_2\text{O}_3$ powders of compositions $n = 1$ and $n = 2$ were provided by Army Research Laboratory and synthesis details are provided elsewhere¹⁰. They are herein referred to as “ARL powders”. The as-received powder was sieved through 58 mesh nylon screen to remove agglomerates that formed during transportation and storage. 20.4 g of powder was loaded into a grafoil-lined circular carbon die with a diameter of 3.81 cm (1.5 in.), then hot pressed (Thermal Technologies 610G-25T, Santa Rosa, CA) under a vacuum of 0.01 Pa (10^{-5} Torr) to 1873 K at 7 deg per minute. A pressure of 35 MPa was applied starting at 1473 K and held for 5 hours at 1873 K before unloading and naturally cooling. Post hot pressing, the pellets were polished with 68 grit SiC paper to remove all grafoil, then hot isostatically pressed (HIPed) by American Isostatic Pressing (Columbus, OH) to 2123 K and 207 MPa for 5 hours in argon to further ensure the starting material was single phase with a density greater than 99.8% of theoretical. For comparison, a plate of dense, stoichiometric ($n = 1$) transparent spinel 15 mm thick was obtained from the vendor ArmorLine. It was densified by the vendor with a two-step hot-press/HIP

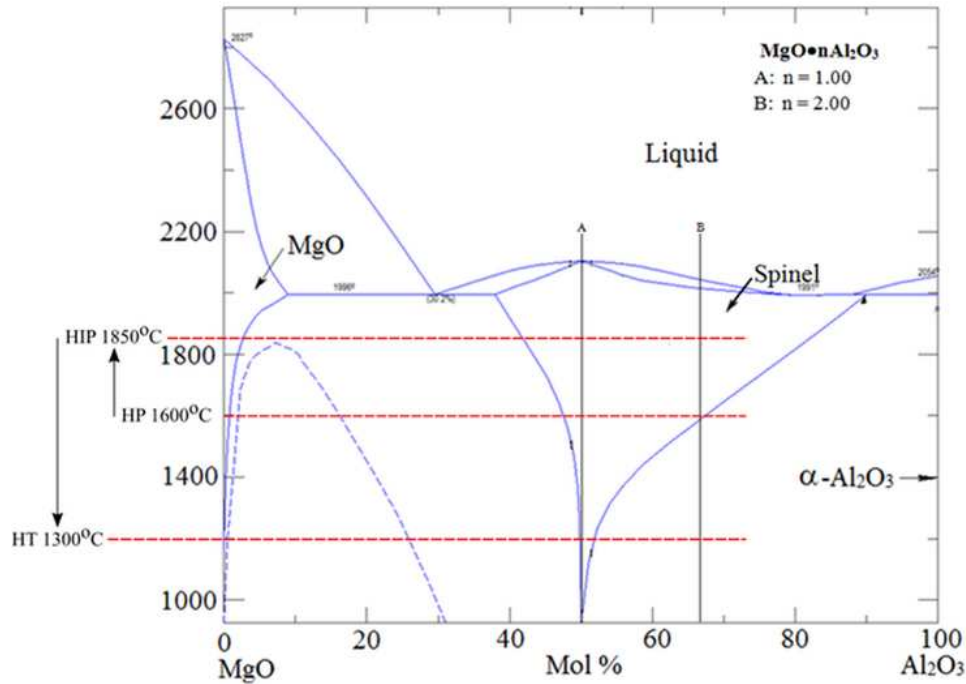


Figure 4.3 The MgO-Al₂O₃ phase diagram is shown with vertical lines marked A and B to denote stoichiometric ($n = 1$) and Al-rich ($n = 2$) compositions, respectively. The intersection of these lines with the horizontal dotted lines show the thermodynamically favored phases for each composition at the hot pressing, hot isostatic pressing, and heat treatment temperatures used in this study.

approach, similar to the densification procedure in the present work. The ArmorLine material was not heat treated.

Post HIPing, heat treatments were performed in air at 1573 K for 1, 5, 10, 15, and 20 hours using a drop down furnace (Deltech DT/31/RS/BHW, Denver, CO). Figure 4.3 uses the spinel phase diagram to illustrate the thermodynamically favorable phases for each composition at each processing step. Post heat treatment, 1.0 mm of material was removed from opposite faces to reveal a length-wise cross section and the opposing sides were polished to 1 μm diamond finish for indentation and optical transmission measurements.

Toughness was measured by two techniques, the chevron notch method³⁵ and the indentation fracture toughness method³⁶. For the former, the material was ground to plane-

parallel with a uniform thickness of 4.0 mm using a surface grinder with a 400 grit diamond wheel and machined into chevron notch bars of dimensions 25.0 x 4.0 x 3.1 mm by Bomas Machining (Somerville, MA) for four-point bending (Instron 8562, High Wycombe UK). For indentation toughness, a 4x10 grid of indents was made on the polished surface of each specimen (Instron 1350, High Wycombe UK) where each indent was separated by a distance of 1.3 mm (0.05 in.) and the first row of indents was 0.5 mm from the edge. All valid indents from each grid were evaluated per methods investigated by Anstis where fracture toughness is determined by:

$$K_{Ic} = \zeta_V^R \left(\frac{E}{H} \right)^{1/2} \left(\frac{P}{c_0^{1/2}} \right) \quad (4.1)$$

The parameter ζ_V^R is an experimental calibration constant³⁶ determined to be 0.016 ± 0.004 and the variables E, H, P, and C_0 are the elastic modulus, hardness, applied load, and length of the half-penny crack, respectively. The elastic modulus of n = 2 spinel was determined to be 298.8 ± 4.0 GPa by nanoindentation (Hysitron TI 950 TriboIndenter, Minneapolis, MN) and Vickers hardness 9.807 N (1 kgf) was determined to be 11.5 GPa (Instron Wolpert 350, High Wycombe UK). Using the same machine and applying a load of 29.420 N (3 kgf) created a deformation zone large enough to interact with several grains and created half penny cracks of acceptable geometry to allow measurement of the toughness of the polycrystalline material. On select specimens, microhardness and nanohardness was evaluated. Vickers microhardness was evaluated according to ASTM standards³⁷ using a load of 0.9807 N (100 gf) (Wilson/ Tukon Series 200, Buehler, Lake Bluff, IL) where indents were spaced 55 μm (0.002 in.) apart, with indent diagonals of approximately 12 – 15 μm . Nanohardness was measured using a Hysitron TI 950 TriboIndenter (Minneapolis, MN) where a load of 10,000 μN was applied for indents in a 10

x 10 grid with 50 μm spacing between indents.

In-line transmission through each specimen was measured from 400-4000 cm^{-1} (2500-25000nm) using Fourier transform infrared spectroscopy (Thermo Scientific Nicolet Magna 550 Series II, Waltham, MA) where specimens were 1.1 mm thick and polished to 1 μm finish on both sides. Optical microscopy (Leco Olympus PMG3, St. Joseph, MI) and scanning electron microscopy (JEOL JSM-7000F, Tokyo, Japan) were used to evaluate the microstructure.

4.4 Results and discussion

The structural evolution of the second phase, the mechanical properties, and the optical properties were investigated in this study. To clarify the work presented, each will be discussed individually.

4.4.1 Precipitation

Precipitation was observed to occur first at the surface and then proceed into the interior of the specimen. The times investigated here (up to 20 hours) did not allow sufficient time for uniform precipitation throughout the bulk, resulting in a final microstructure consisting of a two phase Al_2O_3 -spinel region near the surface that terminated abruptly into a single-phase Al-rich spinel matrix towards the core of the specimen. A representative image of the reaction front is shown in Figure 4.4. The porosity observed within the precipitated region is attributed volume contraction as more dense Al_2O_3 separates from the single phase, Al-rich spinel. The theoretical densities of α - Al_2O_3 and stoichiometric ($n = 1$) spinel are 3.980 and 3.583 g/cm^3 , respectively. Assuming the defect reaction proposed by Okuyama³⁹ and the calculating the ideal lattice parameter for $n = 2$ spinel proposed by Viertel's relationship for non-stoichiometric spinel^{40,41}, a theoretical density of 3.567 g/cm^3 is calculated for $n = 2$ spinel. Therefore, one mol of $n = 2$

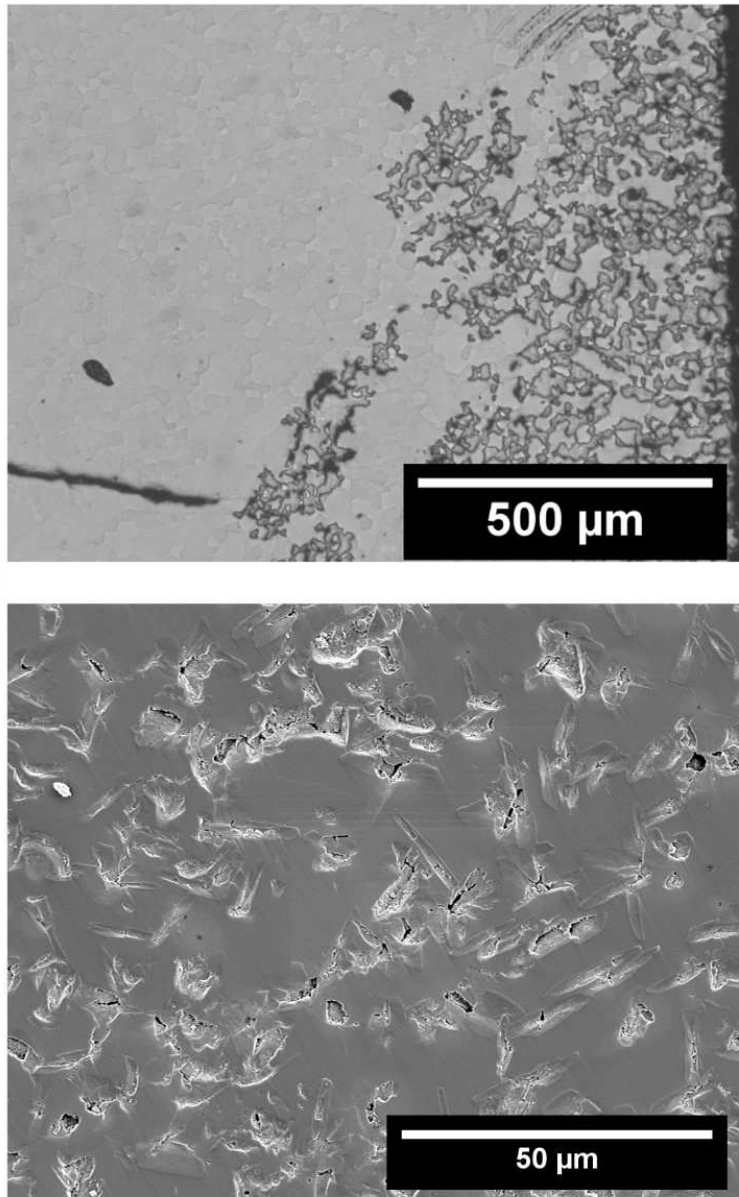


Figure 4.4 A polished cross section of $n = 2$ spinel after 15 hours of heat treatment in air is shown, illustrating the advance of the Al_2O_3 precipitation front from the surface shown at right (Top). Higher magnification reveals that porosity forms at spinel- Al_2O_3 phase boundaries to compensate for the volume contraction that occurs when Al_2O_3 precipitates (Bottom).

Table 4-1 The Indentation toughness and Chevron notch toughness of n = 2 spinel as-HIPed and after 1 hour of heat treatment is compared.

HT Time (hours)	Precipitation Depth (μm)	Indentation K_{IC} ($\text{MPa}\sqrt{\text{m}}$)	Chevron Notch K_{IC} ($\text{MPa}\sqrt{\text{m}}$)
as-HIPed	0 ± 0	1.72 ± 0.06	1.73 ± 0.03
1	0 ± 0	1.68 ± 0.04	1.73 ± 0.06

spinel separating into one mole of n = 1 spinel and one mol of $\alpha\text{-Al}_2\text{O}_3$ would result in a volume contraction of 4.54% if not restrained by surrounding material. Quantification of the observed porosity was attempted, but precise measurements using Archimedes method were unsuccessful because the overall change in density created by the small volume of precipitated material was smaller than experimental error. Image analysis using ImageJ software indicated a porosity of 3-5% within the precipitated regions.

4.4.2 Mechanical properties

The fracture toughness determined by chevron notch for the as-HIPed and one-hour heat treatments of the n = 2 ARL material are $1.73 \pm 0.03 \text{ MPa}\cdot\text{m}^{0.5}$ and $1.73 \pm 0.04 \text{ MPa}\cdot\text{m}^{0.5}$, respectively, compared to $1.72 \pm 0.06 \text{ MPa}\cdot\text{m}^{0.5}$ and $1.68 \pm 0.04 \text{ MPa}\cdot\text{m}^{0.5}$ by indentation fracture toughness, as summarized in Table 4-1. The chevron notch technique was not used for the remaining heat treatment times because precipitation originated at the surface and did not reach the center of the specimens even after 20 hours, so the notch tip would be located within single phase spinel regardless of heat treatment time. Therefore, this technique could not accurately evaluate the behavior of a crack tip originating in the precipitated region and the indentation toughness technique was used to specifically probe such locations.

Figure 4.5 compares indents made in the single-phase region near the precipitation front and in the precipitated region for n = 2 spinel heat treated for 20 hours to indents made in the as-

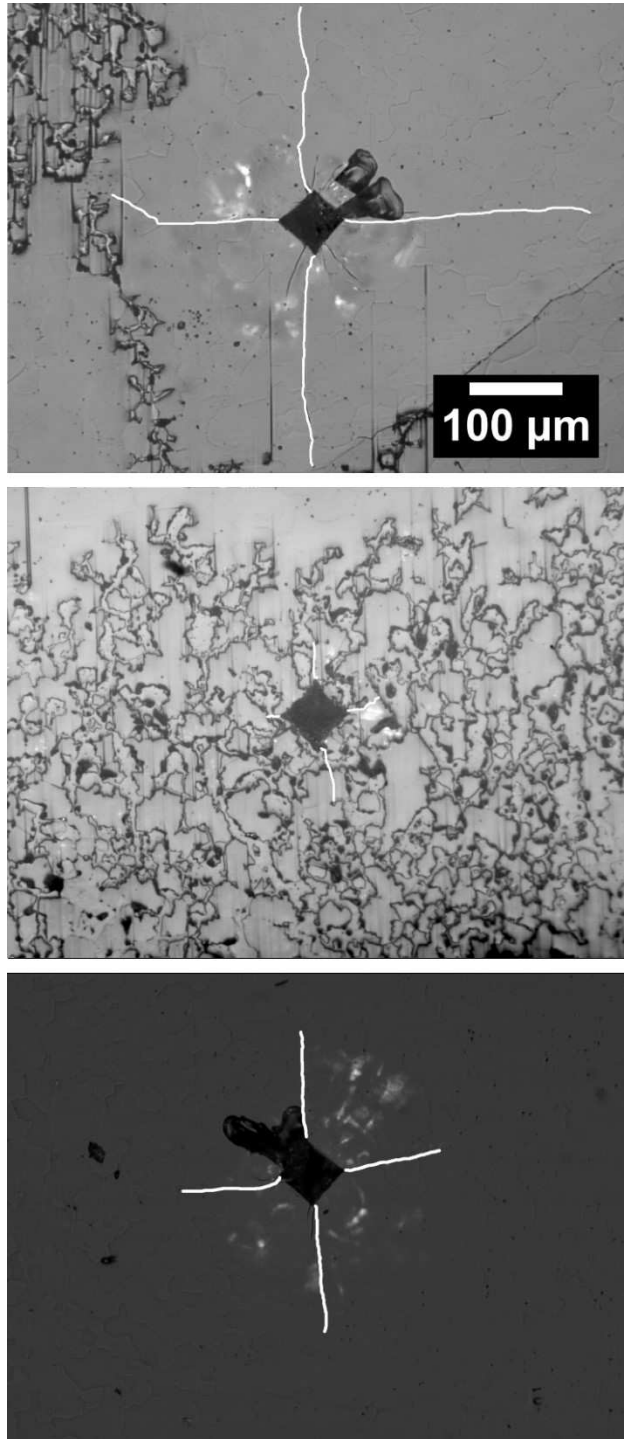


Figure 4.5 A Vickers indent in the spinel matrix just beyond the precipitation front after 20 hours (Top) is compared to an indent made within the precipitated region after 20 hours (Middle) and an indent made in the as-HIPed material (Bottom) where the emanating cracks are enhanced in white. Compared to the indent in the as-HIPed specimen, the cracks did not propagate as far in the precipitated region. However, longer cracks were observed in the single-phase region immediately preceding the precipitation front.

HIPed $n = 2$ material. The shortest cracks were observed in the precipitated region of the heat treated specimen and further investigation revealed this toughness increase was due to increased crack tortuosity along phase boundaries, as shown in Figure 4.6. A toughness of 2.48 ± 0.07 MPa*m^{0.5} was measured for the precipitated region, showing a significant increase from 1.72 ± 0.06 MPa*m^{0.5} measured for the as-HIPed material. However, indents in the region immediately preceding the precipitation front created cracks longer than those observed in as-HIPed material, and a toughness of 0.88 ± 0.07 MPa*m^{0.5} was measured.

It was observed that the toughness measured by the indentation method of the stoichiometric material made from the ARL powders decreased from 1.42 ± 0.04 MPa*m^{0.5} after HIPing to 1.21 ± 0.07 MPa*m^{0.5} after heat treatment for 20 hours in air; the decrease was attributed to abnormal grain growth during heat treatment. Coarse grain spinel has been shown to exhibit low toughness due to impurities or LiF segregation to the boundaries¹². Grain boundary mobility has been observed to be enhanced by a factor of $10^2 - 10^3$ in Mg-rich spinel compared to stoichiometric and Al-rich spinel^{42, 43}, suggesting the abnormal growth observed in this study might be the result of Mg-rich regions within the $n = 1$ ARL powders. Abnormal growth was not observed in the $n = 2$ material for any length of heat treatment.

The fracture toughnesses measured by the indentation method for the $n = 1$ ARL and the $n = 1$ ArmorLine material, are 1.42 ± 0.04 MPa*m^{0.5} and 1.45 ± 0.08 MPa*m^{0.5}, respectively. The as-received ArmorLine material and the as-HIPed ARL material express a baseline toughness for spinel; adding excess Al₂O₃ provides a modest improvement to the as-HIPed toughness and heat treatment provides further enhancement where precipitation occurs but a reduction in toughness in regions adjacent to the precipitation front. Indentation toughness

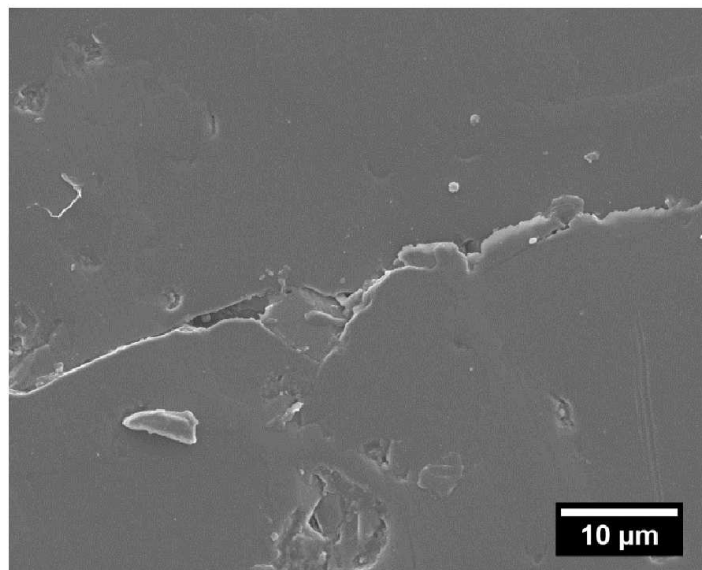
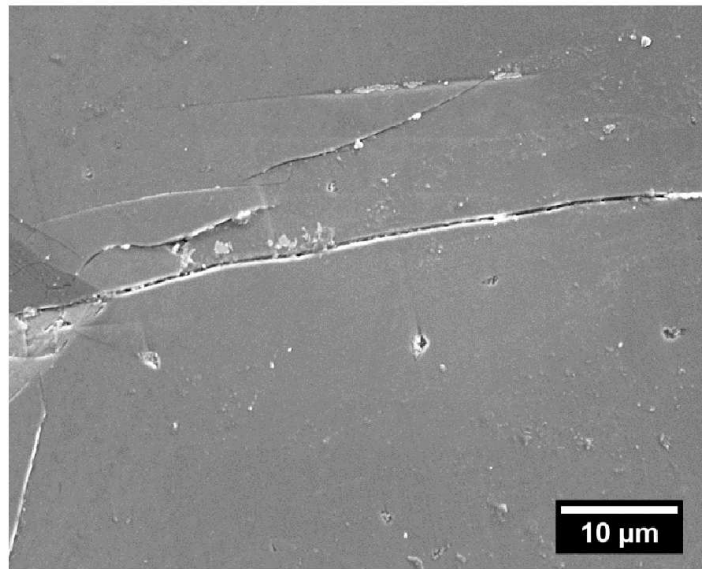


Figure 4.6 SEM micrographs of cracks created from Vickers indents within the matrix (Top) and precipitated region (Bottom) are shown, revealing that second phase Al₂O₃ precipitates greatly enhanced crack tortuosity. In both cases, the indent is out of view to the left of the image.

Table 4-2 The indentation toughness of spinel is summarized for varied compositions and processing conditions. The single-phase matrix and precipitated region of the material heat treated for 20 hours correspond to Region II and Region I, respectively, in Figure 4.7 All indents for all specimens were performed under ambient lab conditions (21°C, 50% relative humidity).

Composition (n)	Source	Heat Treatment	Indent Location	Indentation K_{IC} (MPa \sqrt{m})
1	ArmorLine	as-Received	Bulk	1.45 ± 0.08
1	ARL	as-HIPed	Bulk	1.42 ± 0.04
1	ARL	20 hours in air	Bulk	1.21 ± 0.07
2	ARL	as-HIPed	Bulk	1.72 ± 0.06
2	ARL	20 hours in air	Single phase matrix	0.88 ± 0.07
2	ARL	20 hours in air	Precipitated region	2.48 ± 0.07

values for the ArmorLine and ARL material are summarized in Table 4-2.

The low toughness in the region adjacent to the precipitation front is the result of the residual tensile stresses created from the volume contraction as α -Al₂O₃ precipitates from single phase n = 2 material as discussed earlier. Vickers microhardness was measured as a function of distance from the leading edge of the precipitation front, and results for the specimen heat treated for 10 hours are shown in Figure 4.7. In order to space indents close together without the deformation zone of one indent affecting the next (at least twice as far apart as the length of the indent diagonal, per ASTM standards³⁷), a load of 0.9807 N (100gf) was used; this load allowed the minimal spacing while still producing indents large enough to interact with multiple grains and accurately measure the polycrystalline behavior of the material. While toughness information at this scale would be desirable, the indents at this load did not produce sufficient half-penny cracking behavior to evaluate indentation toughness.

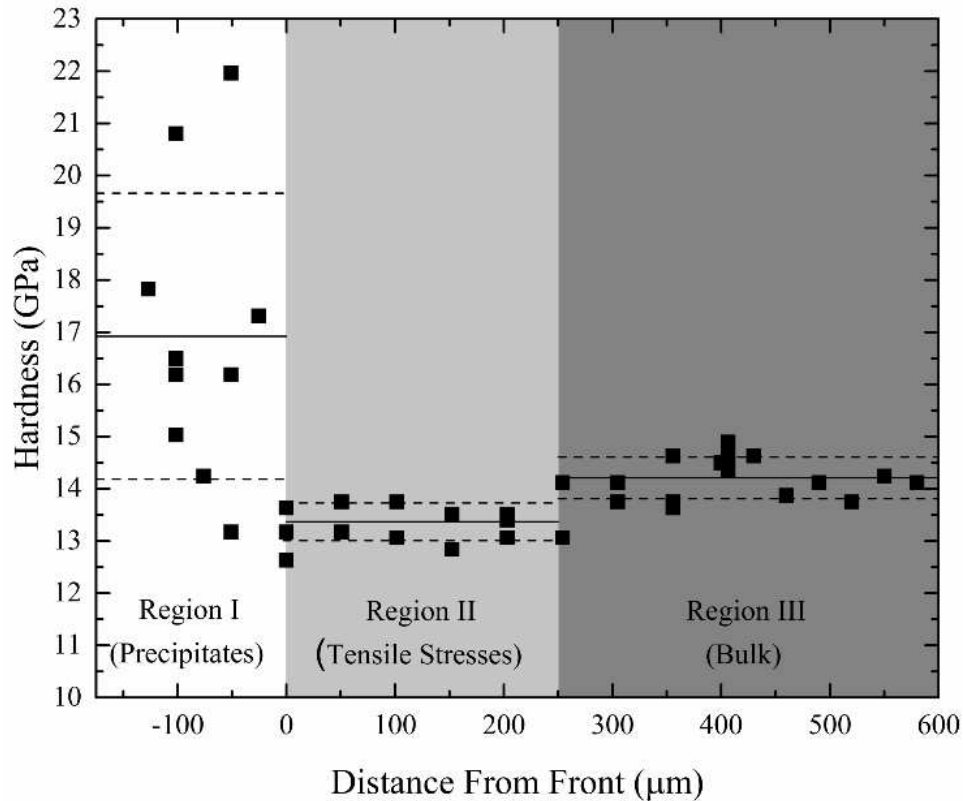


Figure 4.7 Vickers hardness under 100gf load is shown for $n = 2$ spinel heat treated for 10 hours where the leading edge of the precipitation front is designated as the origin for the x-axis. The 3 regions of different hardness values are shown where the average and standard deviation is shown as solid and dashed lines, respectively.

Figure 4.7 reveals that the hardness measured across the specimen can be separated into three distinct regions; Region I includes indents within the precipitated region where the average hardness is highest but scatter is considerably greater, Region II includes indents in the region immediately ahead of the advancing precipitation front where the minimum hardness was measured, and Region III includes indents beyond the affected zone where the hardness is constant. Solid lines and dashed lines represent the average and standard deviation, respectively, for each region. The specimen heat treated for 10 hours is shown because the uniform depth of the precipitation front allows for clear measurement of the distance from indent to the front. The uniformity of the front is lost as “fingers” of precipitation form with increasing heat treatment

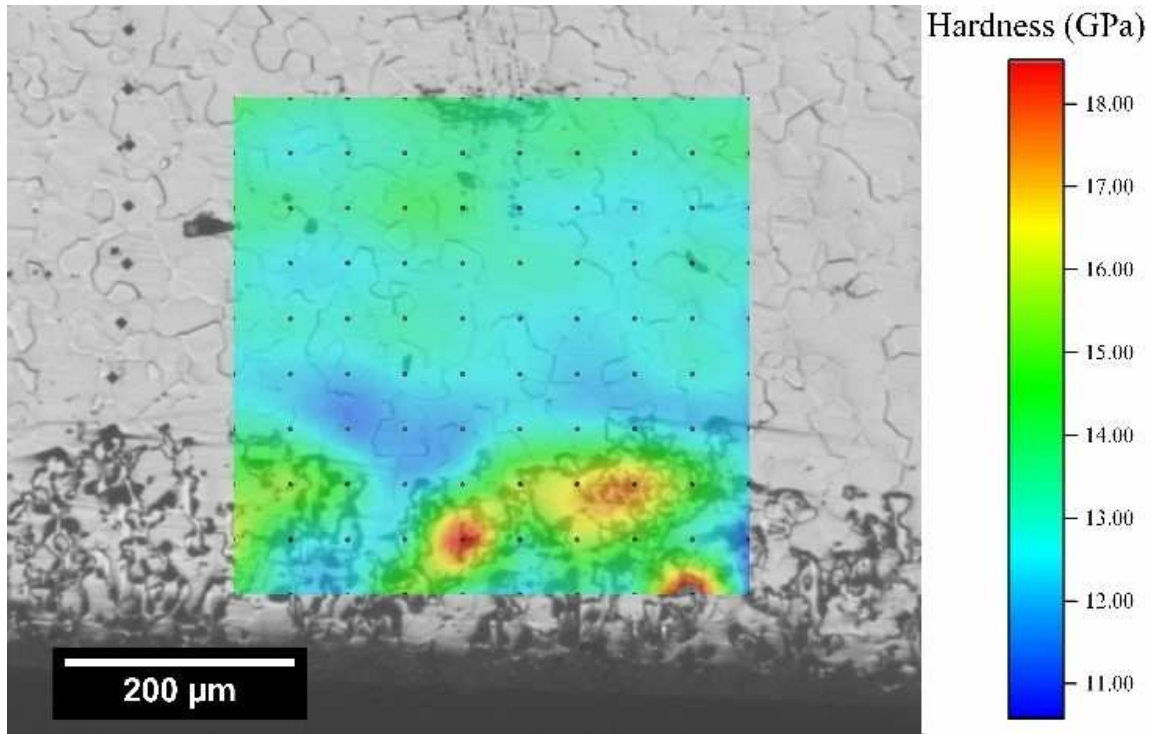


Figure 4.8 Hardness measured by nanoindentation is overlaid onto the specimen from which it was measured. Black dots represent the location of the indent, each spaced 50 μm from other indents. The lowest hardness measured occurred in material immediately adjacent to the precipitation front.

time, making it difficult to accurately assess the distance between indents and the nearest portion of the front, especially if these fingers are just below the surface of indentation. Nanoindentation of the same specimen supported the results observed in microhardness; the highest hardness and the largest variability was observed within the precipitated region and the lowest hardness occurred in the material immediately adjacent. Figure 4.8 (color online) shows measured hardness overlaid onto the microstructure. Both microhardness and nanohardness support the notion that tensile stresses adjacent to the precipitation front exist, decreasing the hardness by approximately 1.0-1.5 GPa compared to the bulk. The slight difference in the magnitudes measured are likely due to indentation size effects; in the material used in this study, microhardness (100 gf) probed the material to a depth of approximately 15 μm compared to a

depth of only 130 nm by nanohardness.

The combination of indentation toughness and micro hardness measurements explain how the structural evolution of non-stoichiometric spinel alters the mechanical properties as α - Al_2O_3 precipitates with increasing heat treatment time. Initially, precipitates form at the free surface where the volume contraction is more easily accommodated. The fracture toughness is enhanced within this two-phase region because of increased crack tortuosity at phase boundaries. As the precipitation front advances into the bulk of the material and the distance from the free surface increases, the volume contraction incurred during precipitation leads to both porosity and tensile stress. The residual tensile stresses are most severe in the material immediately in front of the advancing precipitation front. Crack propagation is stimulated in this region, resulting in a lower fracture toughness than in the as-HIPed material. The residual stress decreases and the mechanical properties increase with increasing distance away from the precipitation front and into the bulk.

4.4.3 Optical properties

The as-HIPed $n = 2$ material showed a maximum in-line transmission of 60.0% at 2800cm^{-1} , but transmission decreased to 1.2% after a heat treatment of 20 hours as shown in Figure 4.9. The loss in transmission is attributed to increased light scattering caused by porosity created to compensate the volume contraction during precipitation of Al_2O_3 . 52.0% transmission was measured for the specimen heat treated for 5 hours after the precipitated region had reached a thickness of $40 \pm 6 \mu\text{m}$, demonstrating that light scatter could be minimal for sufficiently thin precipitation layers.

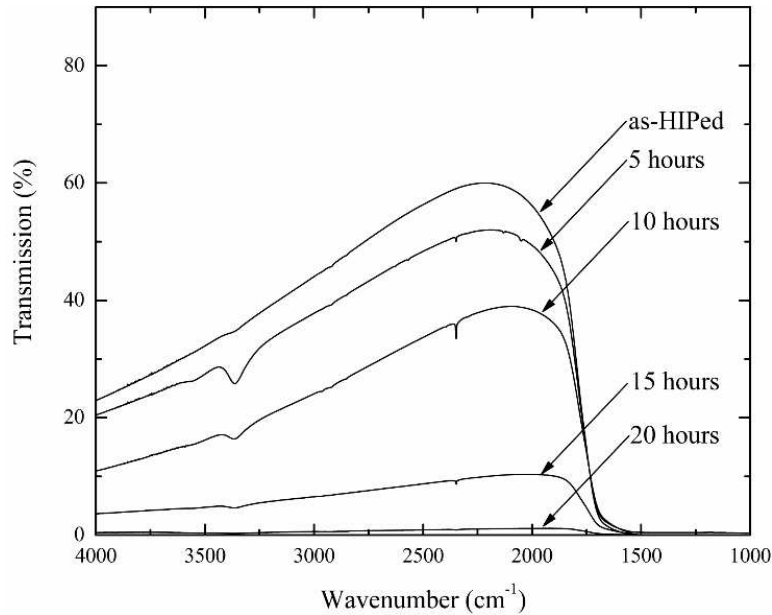


Figure 4.9 FTIR transmission spectra for $n = 2$ spinel heat treated in air for 5, 10, 15, and 20 hours is shown. Transmission decreases with increasing heat treatment time as the thickness of the precipitation front and the amount of porosity increases.

It has been shown that the addition of LiF promotes densification of spinel through removing impurities and reducing porosity⁴⁵. Therefore, the addition of densification aids could potentially minimize light scatter at the material surface by reducing the formation of pores, and such an idea deserves further investigation. However, the mechanisms by which LiF enhances densification are not fully understood, so it was not used in this study to avoid complicating the interpretation of the observed mechanical and optical properties.

4.5 Conclusions

Spinel powder of the composition $n = 2$ was densified into single phase material prior to heat treatment for various times to allow precipitation of Al_2O_3 from single phase Al-rich spinel. The effects on the mechanical and optical properties of the material were examined. Comparison of indentation toughness to chevron notch toughness confirmed that indentation toughness was a viable method for determining the toughness of Al-rich, polycrystalline spinel used in this study.

Examination of individual indentations revealed the fracture toughness was enhanced within precipitated regions due to increased crack tortuosity, but diminished significantly in the nearby unprecipitated regions of the spinel matrix due to residual tensile stresses from volume contraction. In-line transmission decreased with heat treatment time due to porosity formation from Al₂O₃ precipitation.

The results observed in this study suggest that it is possible to significantly enhance the toughness of the surface of magnesium aluminate spinel by precipitating excess Al₂O₃ to increase crack tortuosity along phase boundaries. Furthermore, loss of transmission may be minimal if the precipitated zone remains thin, especially if densification aids are introduced to minimize the formation of porosity. As a result, transparent spinel with more impact resistant surfaces may be created through careful control of the precipitation process from non-stoichiometric materials.

4.6 Acknowledgements

This work was made possible through funding from Corning Incorporated. The Authors also wish to acknowledge Anthony C. Sutorik, currently at Dow Chemical Co., Midland, MI, who provided powder samples and discussions during his tenure at Army Research Laboratory, Aberdeen Proving Grounds, MD.

4.7 References

- ¹ R. Sarkar, A. Ghosh, and S.K. Das, "Reaction sintered magnesia rich magnesium aluminate spinel: Effect of alumina reactivity," *Ceram. Int.*, **29** [4] 407–411 (2003).
- ² A. Ghosh, R. Sarkar, B. Mukherjee, and S.K. Das, "Effect of spinel content on the properties of magnesia-spinel composite refractory," *J. Eur. Ceram. Soc.*, **24** [7] 2079–2085 (2004).

- 3 A. Krell, J. Klimke, and T. Hutzler, “Advanced spinel and sub- μm Al_2O_3 for transparent armour applications,” *J. Eur. Ceram. Soc.*, **29** [2] 275–281 (2009).
- 4 A.A. DiGiovanni, L. Fehrenbacher, and D.W. Roy, “Hard Domes and Windows from Magnesium Aluminate Spinel;” pp. 56–63 in *Wind. Dome Technol. Mater.* Edited by R.W. Tustison. SPIE- The International Society for Optical Engineering, Orlando, 2005.
- 5 J.A. Salem, “Transparent armor ceramics as spacecraft windows,” *J. Am. Ceram. Soc.*, **96** [1] 281–289 (2013).
- 6 B. Hallstedt, “Thermodynamic Assessment of the System $\text{MgO}-\text{Al}_2\text{O}_3$,” *J. Am. Ceram. Soc.*, **75** [6] 1497–1507 (1992).
- 7 E.F. Osborn, “Subsolidus Reactions in Oxide Systems in the Presence of Water at High Pressures,” *J. Am. Ceram. Soc.*, **36** [5] 147–151 (1953).
- 8 A. Krell and A. Bales, “Grain Size-Dependent Hardness of Transparent Magnesium Aluminate Spinel,” *Int. J. Appl. Ceram. Technol.*, **8** [5] 1108–1114 (2011).
- 9 A.C. Sutorik, C. Cooper, and G. Gilde, “Visible Light Transparency for Polycrystalline Ceramics of $\text{MgO}\cdot 2\text{Al}_2\text{O}_3$ and $\text{MgO}\cdot 2.5\text{Al}_2\text{O}_3$ Spinel Solid Solutions,” *J. Am. Ceram. Soc.*, **96** [12] 3704–3707 (2013).
- 10 A.C. Sutorik, G. Gilde, J.J. Swab, C. Cooper, R. Gamble, and E. Shanholtz, “Transparent Solid Solution Magnesium Aluminate Spinel Polycrystalline Ceramic with the Alumina-Rich Composition $\text{MgO}\cdot 1.2\text{Al}_2\text{O}_3$,” *J. Am. Ceram. Soc.*, **95** [2] 636–643 (2012).
- 11 A.F. Dericioglu, A.R. Boccaccini, I. Dlouhy, and Y. Kagawa, “Effect of Chemical Composition on the Optical Properties and Fracture Toughness of Transparent Magnesium Aluminate Spinel Ceramics,” *Mater. Trans.*, **46** [5] 996–1003 (2005).
- 12 M. Rubat Du Merac, H.J. Kleebe, M.M. Muller, and I.E. Reimanis, “Fifty years of research and development coming to fruition; Unraveling the complex interactions during processing of transparent magnesium aluminate (MgAl_2O_4) spinel,” *J. Am. Ceram. Soc.*, **96** [11] 3341–3365 (2013).
- 13 C.B. Huang, T.C. Lu, L. Bin Lin, M.Y. Lei, and C.X. Huang, “A Study on Toughening and Strengthening of Mg-Al Spinel Transparent Ceramics,” *Key Eng. Mater.*, **336–338** 1207–1210 (2007).
- 14 I. Ganesh, “A review on magnesium aluminate (MgAl_2O_4) spinel: synthesis, processing and applications,” *Int. Mater. Rev.*, **58** [2] 63–112 (2012).

- 15 A. Goldstein, “Correlation between $MgAl_2O_4$ -spinel structure, processing factors and functional properties of transparent parts (progress review),” *J. Eur. Ceram. Soc.*, **32** [11] 2869–2886 (2012).
- 16 A.C. Sutorik, G. Gilde, C. Cooper, J. Wright, and C. Hilton, “The Effect of Varied Amounts of LiF Sintering Aid on the Transparency of Alumina Rich Spinel Ceramic with the Composition $MgO \cdot 1.5Al_2O_3$,” *J. Am. Ceram. Soc.*, **95** [6] 1807–1810 (2012).
- 17 T. Mroz, L.M. Goldman, A.D. Gledhill, D. Li, and N.P. Padture, “Nanostructured, Infrared-Transparent Magnesium-Aluminate Spinel with Superior Mechanical Properties,” *Int. J. Appl. Ceram. Technol.*, **9** [1] 83–90 (2012).
- 18 M. Shimada, T. Endo, T. Saito, and T. Sato, “Fabrication of transparent spinel polycrystalline materials,” *Mater. Lett.*, **28** [October] 413–415 (1996).
- 19 Y. Chou and D.J. Green, “Silicon Carbide Platelet/Alumina Composites: I I, Mechanical Properties,” *J. Am. Ceram. Soc.*, **76** [6] 1452–1458 (1993).
- 20 Y. Fan, G. Igarashi, W. Jiang, L. Wang, and A. Kawasaki, “Highly strain tolerant and tough ceramic composite by incorporation of graphene,” *Carbon N. Y.*, **90** 274–283 (2015).
- 21 J. Rodel, “Interaction between crack deflection and crack bridging,” *J. Eur. Ceram. Soc.*, **10** [3] 143–150 (1992).
- 22 B. Budiansky, J.C. Amazigo, and A.G. Evans, “Small-scale crack bridging and the fracture toughness of particulate-reinforced ceramics,” *J. Mech. Phys. Solids*, **36** [2] 167–187 (1988).
- 23 M. Taya, S. Hayashi, A.S. Kobayashi, and H.S. Yoon, “Toughening of a Particulate-Reinforced Ceramic-Matrix Composite by Thermal Residual Stress,” *J. Am. Ceram. Soc.*, **73** [5] 1382–1391 (1990).
- 24 W. Kreher and W. Pompe, “Increased fracture toughness of ceramics by energy-dissipative mechanisms,” *J. Mater. Sci.*, **16** 694–706 (1981).
- 25 I. Yamashita, H. Nagayama, and K. Tsukuma, “Transmission Properties of Translucent Polycrystalline Alumina,” *J. Am. Ceram. Soc.*, **91** [8] 2611–2616 (2008).
- 26 R. Rice, *Characterization of Hot-Pressed MgO*. Washington, D.C., 1971.
- 27 R. Apetz and M.P.B. Bruggen, “Transparent Alumina: A Light-Scattering Model,” *J. Am. Ceram. Soc.*, **86** [3] 480–486 (2003).
- 28 D.C. Harris, *Materials for Infrared Windows and Domes: Properties and Performance*. SPIE- The International Society for Optical Engineering, Bellingham, Washinton, 1999.

- 29 A. Krell, J. Klimke, and T. Hutzler, "Transparent compact ceramics: Inherent physical issues," *Opt. Mater. (Amst.)*, **31** [8] 1144–1150 (2009).
- 30 M.H. Lewis, "Precipitation in non-stoichiometric spinel crystals," *Philos. Mag.*, **20** 958–998 (1969).
- 31 N. Doukhan, J.C. Doukhan, and B. Escaig, "T.E.M. Study of High Temperature Precipitation in $(\text{Al}_2\text{O}_3)_n \text{MgO}$ Spinel," *Mater. Res. Bull.*, **11** [2] 125–34 (1976).
- 32 W.T. Donlon, T.E. Mitchell, and A.H. Heuer, "Precipitation in non-stoichiometric spinel," *J. Mater. Sci.*, **17** 1389–1397 (1982).
- 33 P.C. Panda and R. Raj, "Kinetics of Precipitation of $\alpha\text{-Al}_2\text{O}_3$ in Polycrystalline Supersaturated $\text{MgO}\cdot 2\text{Al}_2\text{O}_3$ Spinel Solid Solution," *J. Am. Ceram. Soc.*, **69** [5] 365–73 (1986).
- 34 G.K. Bansal and A.H. Heuer, "Precipitation in nonstoichiometric magnesium aluminate spinel," *Philos. Mag.*, **29** [4] 709–722 (1974).
- 35 American Society for Testing and Materials, "Standard Test Methods for Determination of Fracture Toughness of Advanced Ceramics," *ASTM Stand. C1421-10*, 1–66 (2014).
- 36 G.R. Anstis, P. Chantikul, B.R. Lawn, and D.B. Marshall, "A Critical Evaluation of Indentation Techniques for Measuring Fracture Toughness: I, Direct Crack Measurements," *J. Am. Ceram. Soc.*, **64** [September] 533–538 (1981).
- 37 American Society for Testing and Materials, "Standard Test Method for Knoop and Vickers Hardness of Materials," *ASTM Stand. E384-11*, 1–43 (2012).
- 38 J.A. Miller, I.E. Reimanis, W. Miao, and A.C. Sutorik, "Diffusion limited precipitation of alumina in magnesium aluminate spinel," *J. Am. Ceram. Soc.*, To Be Published (n.d.).
- 39 Y. Okuyama, N. Kurita, and N. Fukatsu, "Defect structure of alumina-rich nonstoichiometric magnesium aluminate spinel," *Solid State Ionics*, **177** [1–2] 59–64 (2006).
- 40 H.U. Viertel and F. Seifert, "Thermal Stability of defect spinels in the system $\text{MgAl}_2\text{O}_4\text{-Al}_2\text{O}_3$," *N. Jb. Miner. Abh.*, **140** [1] 89–101 (1980).
- 41 H.U. Viertel and F. Seifert, "Physical properties of defect spinels in the system $\text{MgAl}_2\text{O}_4\text{-Al}_2\text{O}_3$," *N. Jb. Miner. Abh.*, **134** [2] 167–182 (1979).
- 42 Y. Chiang and D. Kingery, "Grain-Boundary Migration in Nonstoichiometric Solid Solutions of Magnesium Aluminate Spinel: I, Grain Growth Studies," *J. Am. Ceram. Soc.*, **77** 271–277 (1989).

- 43 Y.M. Chiang and W.D. Kingery, "Grain-boundary migration in nonstoichiometric solid solutions of magnesium aluminate spinel: I, grain growth studies," *J. Am. Ceram. Soc.*, **72** [2] 271–277 (1989).
- 44 L. Fehrenbacher, J. Kutsch, and D. Stockwell, *Transparent Spinel Ceramics For Armor and Electro-Optical Applications*, *Technol. Assess. Transf. Inc.*, 1–4 (n.d.).
- 45 I. Reimanis and H.-J. Kleebe, "A Review on the Sintering and Microstructure Development of Transparent Spinel (MgAl_2O_4)," *J. Am. Ceram. Soc.*, **92** [7] 1472–1480 (2009).

CHAPTER 5

ENHANCED FRACTURE TOUGHNESS IN NON-STOICHIOMETRIC MAGNESIUM ALUMINATE SPINEL THROUGH CONTROLLED DISSOLUTION OF SECOND PHASE ALUMINA

A paper submitted to the Journal of the American Ceramic Society

J. Aaron Miller, Ivar E. Reimanis, Marc Rubat Dumerac

5.1 Abstract

Dissolution of Al_2O_3 particles into a MgAl_2O_4 (spinel) matrix is accompanied by a volumetric expansion that is predicted to lead to a compressive stress field upon cooling, a promising microstructure for enhanced toughening of transparent spinel. The present study explores the conditions to form such a microstructure by hot pressing powders of Al_2O_3 particles contained in stoichiometric spinel ($\text{MgO}\cdot n\text{Al}_2\text{O}_3$) to form the overall composition $n = 2$. Particulate composites were formed under shorter hot press times, but complete Al_2O_3 dissolution was achieved after hot pressing at 1700°C for 10 hours. A toughness of 4.34 ± 0.20 $\text{MPa}\sqrt{\text{m}}$ was achieved for the particulate composite. Complete dissolution led to a toughness of 2.26 ± 0.17 $\text{MPa}\sqrt{\text{m}}$, significantly higher than for the equivalent non-stoichiometric spinel made by traditional methods, 1.72 ± 0.06 $\text{MPa}\sqrt{\text{m}}$. X-ray diffraction measurements revealed lattice parameter changes consistent with the dissolution of Al_2O_3 into spinel. The observed enhancement in toughness in the material is attributed to a combination of residual stresses that arise from the coefficient of thermal expansion mismatch between particle and matrix, crack deflection caused by second phase particles, and the volume expansion as Al_2O_3 dissolves into the spinel matrix.

5.2 Introduction

The mechanical properties of traditional, monolithic ceramic materials can be enhanced through the addition of a second phase, where crack propagation may be deterred via mechanisms including crack bridging¹⁻³, crack deflection⁴⁻⁶, or residual stresses⁷. An additional challenge exists for transparent ceramics since microstructure modifications typically lead to light scattering that may occur at pores^{8,9} or due to the presence of a second phase.

Magnesium aluminate spinel, $\text{MgO}\cdot\text{Al}_2\text{O}_3$, referred to as spinel here, is well-known ceramic with many uses¹⁰⁻¹⁴, including ones where high transparency in the visible and infra-red regime is required, such as missile radomes¹⁵⁻¹⁷, transparent armor^{16,18}, and space craft windows¹⁹. The utility of transparent spinel could be greatly improved if the strength and toughness could be increased over the typical values achieved to date, which range from 250 – 400 MPa for strength^{3,13,20,21} and 1.8 – 2.0 $\text{MPa}\sqrt{\text{m}}$ for toughness¹². Polycrystalline Al_2O_3 has itself been produced as transparent material^{18,22,23}, and is highly soluble into stoichiometric spinel²⁴⁻²⁹. Although the mechanical and optical properties of single phase, Al-rich spinel have already been investigated³⁰⁻³³, few studies have investigated such properties for two phase Al_2O_3 -spinel composite materials³⁴.

The current study seeks to explore the feasibility of enhancing the fracture toughness of magnesium aluminate spinel through the introduction of second phase Al_2O_3 particles. Not only is this system composed of two transparent materials, but there exists the potential to dissolve Al_2O_3 into the spinel matrix, creating a design space in which the amount and morphology of the second phase particles may be controlled. Specifically, the dissolution of an Al_2O_3 particle into a spinel matrix results in a 4.76% volume expansion if there is no stress relaxation, and thus, the

possibility exists to form a nearly monolithic, transparent ceramic with a spatially varying residual stress field. The evolution of the second phase as controlled by varied densification parameters and the relationship to the resulting mechanical properties are investigated.

5.3 Experimental procedure

Materials were made by combining stoichiometric ($n = 1$) magnesium aluminate spinel powder (Baikowski, Malakoff TX) with enough Al_2O_3 (SASOL, Tucson AZ) powder such that the overall composition corresponds to $n = 2$ for $\text{MgO} \cdot n\text{Al}_2\text{O}_3$. $\alpha\text{-Al}_2\text{O}_3$ was used for most of the experiments, but one specimen with $\gamma\text{-Al}_2\text{O}_3$ was investigated. The particle sizes and purities of the starting powders are summarized in Table 5-1. While larger in starting particle size than the $\alpha\text{-Al}_2\text{O}_3$ material, the $\gamma\text{-Al}_2\text{O}_3$ powder is of higher purity. More importantly, $\gamma\text{-Al}_2\text{O}_3$ was included in the study to investigate any differences in dissolution between cubic $\gamma\text{-Al}_2\text{O}_3$ and hexagonal $\alpha\text{-Al}_2\text{O}_3$ into the cubic spinel matrix. Powders were mixed in DI water to form a slurry of 20 wt. % solids and milled in a Nalgene bottle for 24 hours with no media to allow uniform dispersion of the spinel and Al_2O_3 particles. The slurry was then dried using roto-evaporation (Buchi R-210, New Castle DE) for 3 hours with the chiller temperature, heater temperature, and vacuum held at 5°C , 80°C , and 8 KPa, respectively. The resulting cake material was further dried at 100°C for 48 hours in a drying oven (Fisher Scientific, Waltham MA) before being milled with Al_2O_3 media for 3 hours and sieved through 300 μm mesh.

Table 5-1 The particle size and purities of the starting powders is summarized.

Material	Baikowski $\text{MgO} \cdot \text{Al}_2\text{O}_3$	SASOL $\alpha\text{-Al}_2\text{O}_3$	SASOL $\gamma\text{-Al}_2\text{O}_3$
Particle Size (μm)	0.43	0.30	1.8
Purity	99.995%	99.99%	99.997+%

To form dense compacts, 10 g of the mixed powder was hot pressed (Thermal Technologies

610G-25T, Santa Rosa CA) in a 2.54 cm diameter circular carbon die lined with grafoil. To evaluate the effects of hot pressing time on the dissolution of Al_2O_3 into spinel, separate runs were held at 1600°C for 5, 10, 20, and 30 hours. Additional runs were held at 1650°C and 1700°C for 10 hours to investigate the role of increasing temperature. For all runs, a 2 hour hold at 400°C and a 1 hour hold at 1200°C were included; holding at low temperature allowed a vacuum level of 0.01 Pa (10^{-5} Torr) to be maintained by removing moisture and organic impurities while the high temperature hold allowed for thermal equilibration of the system and off gassing of high temperature volatiles before the load was applied. 1200°C was chosen as the maximum temperature to allow off gassing before grain growth is expected in spinel¹². At the end of the 1200°C hold, a load of 35 MPa was applied as temperature was increased and held until the end of the high temperature soak. Both ramp up and cool down rates were held to 7 degrees C per minute. The densified specimens were then cut to reveal the cross section (Buehler Isomet Low Speed Saw, Lake Bluff IL), then ground to plane-parallel with a thickness of 1.1 mm (Harig Grinder, MT Clemens MI) before being polished to 1 μm diamond finish.

X-ray diffraction (PANalytic Phillips X'Pert Pro, Almelo, The Netherlands) and scanning electron microscopy with energy dispersive spectroscopy (JEOL JSM-7000F, Tokyo, Japan) were performed to assist in the evaluation of the extent of dissolution of Al_2O_3 into spinel. Reitveld refinement was used to model the X-ray diffraction results and peak shifts were correlated with Al_2O_3 dissolution as well as residual stresses in the remaining Al_2O_3 particles. The amount of second phase Al_2O_3 present was quantified using image analysis software (FIJI ImageJ 1.51d) on images of the polished surfaces. For each specimen, light microscopy was used (Leco Olymus PMGS, St. Joseph MI) to collect images from a minimum of 3 different locations.

Indentation fracture toughness was measured according to methods investigated by Anstis³⁵ where toughness is determined by:

$$K_{Ic} = \zeta_V^R \left(\frac{E}{H} \right)^{1/2} \left(\frac{P}{c_0^{1/2}} \right) \quad (5.1)$$

The parameter ζ_V^R is the material independent experimental calibration constant equal to 0.016 ± 0.004 . The elastic modulus, E, was determined for each specimen by nanoindentation (Hysitron TI 950 Triboindenter, Minneapolis MN) where indents were made using a load of 0.01 N. The hardness, H, was determined using a load of 9.807 N (1 kgf) (Instron Wolpert 350, High Wycombe, UK), while indents for indentation toughness were made using the same indenter with a load, P, of 29.420 N (3 kgf). The length of the half-penny crack, c_0 , was measured using optical microscopy. Via comparison with chevron notch fracture toughness testing, it was previously determined that the method of Anstis, et al worked well to determine the fracture toughness of spinel³⁶.

5.4 Results and discussion

The structural evolution and resulting mechanical properties are discussed.

5.4.1 Structural evolution

XRD indicated the expected peaks for spinel and α -Al₂O₃ powder mixtures (Figure 5.1). However, γ -Al₂O₃ peaks had low relative intensities, likely due to the large surface area associated with small crystallite size (Figure 5.1, inset). Thus, the highest-intensity peaks at 39.34°, 45.36°, and 66.62° were obscured by shoulders of spinel peaks at 39.20°, 45.10°, and 65.23° 2 θ , respectively. After hot pressing for 5 hours at 1600°C, only spinel and α -Al₂O₃ peaks were present (Figure 5.2). Hot-pressed γ -

Al₂O₃ and spinel powder mixture patterns revealed no γ -Al₂O₃ peaks, indicating complete conversion to α -Al₂O₃, consistent with previous work.³⁷ Since γ -Al₂O₃ converts to α -Al₂O₃ before significant dissolution, only mixtures with α -Al₂O₃ were hot pressed using longer times and higher temperatures.

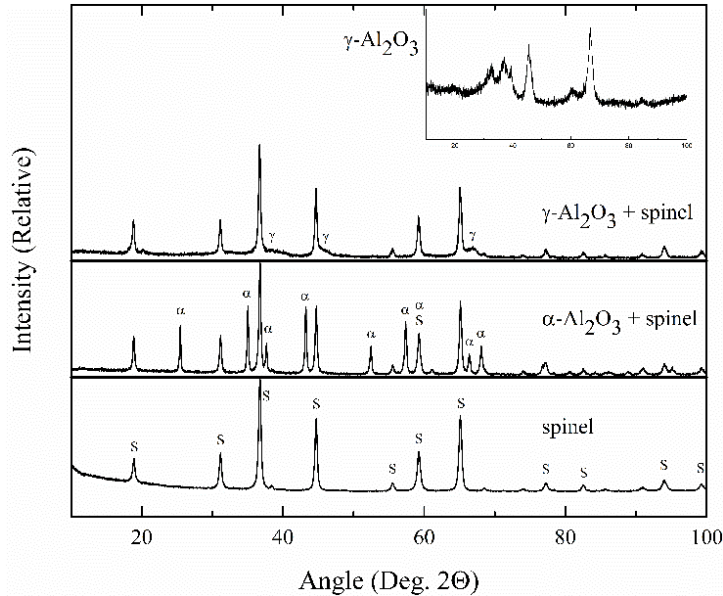


Figure 5.1 XRD patterns of α -Al₂O₃ and γ -Al₂O₃ powders mixed with stoichiometric ($n = 1$) spinel powder are shown. For reference, pure $n = 1$ powder is also shown where all peaks are identified as spinel (S). Because of the lack of crystallinity in the starting powder, γ -Al₂O₃ peaks (γ) at 39.34, 45.36, and 66.62 deg. (inset) were overwhelmed when mixed with spinel powder, while peaks from α -Al₂O₃ (α) were clearly identifiable when mixed.

The XRD patterns for hot pressed material for 5, 10, 20, and 30 hours at 1600°C, 10 hours at 1650°C, and 10 hours at 1700°C are shown in Figure 5.3 and peaks at approximately 35° and 37° are shown in detail in Figure 5.4. After hot pressing at 1600°C for 5 hours, the diffraction peak from the 104 plane of α -Al₂O₃ was observed at 35.04°. This peak shifted to higher angles while decreasing in intensity until disappearing after hot pressing at 1700°C for 10 hours. Diffraction from the 311 spinel plane created the peak initially at 36.94°, which also shifted to higher angles with increased hot pressing time and temperature. This peak shift indicates the lattice parameters of both phases are decreasing; Chiang and Kingery's³⁸ summary

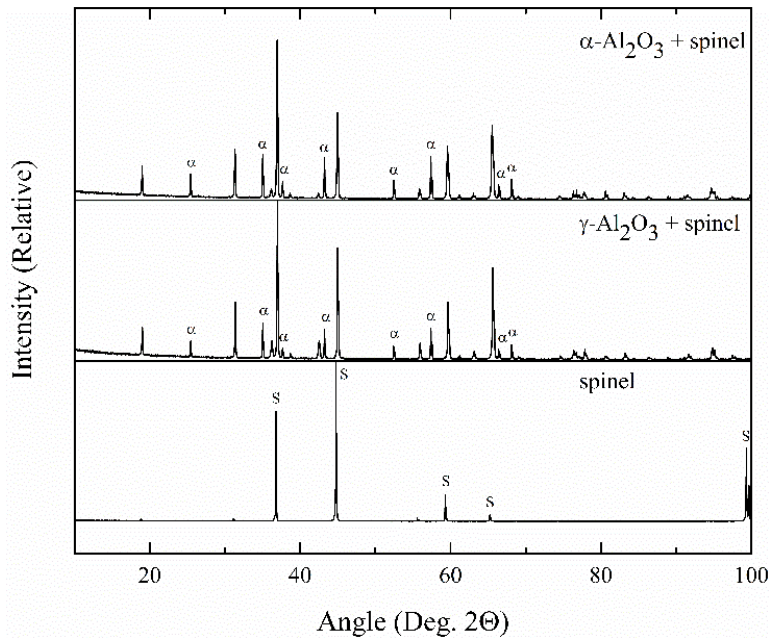


Figure 5.2 XRD patterns are shown for powders hot pressed for 5 hours at 1600°C. Regardless of whether α -Al₂O₃ or γ -Al₂O₃ powder was mixed with $n = 1$ powder, all peaks were identified as spinel (S) or α -Al₂O₃ (α) post hot pressing.

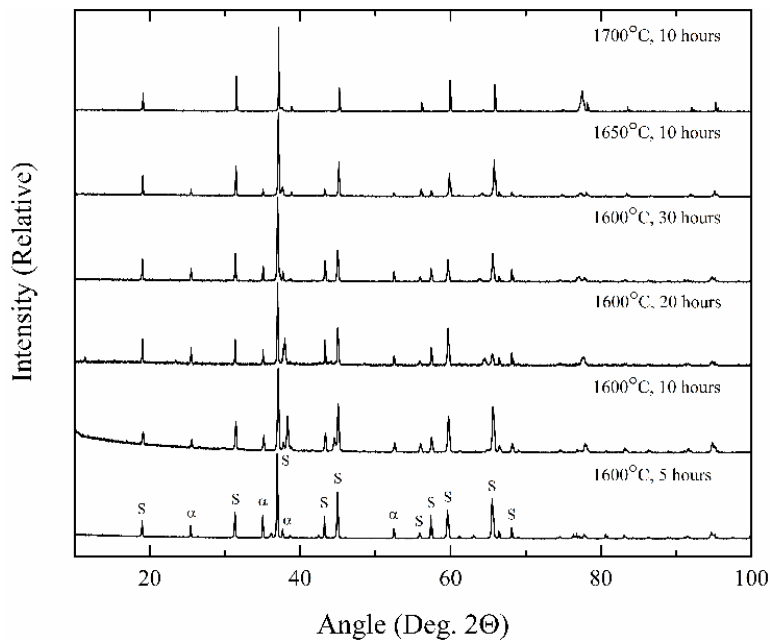


Figure 5.3 XRD patterns are shown for various hot pressing temperatures. In all cases, α -Al₂O₃ and stoichiometric ($n = 1$) spinel powders were mixed to form an overall composition of MgO•2Al₂O₃.

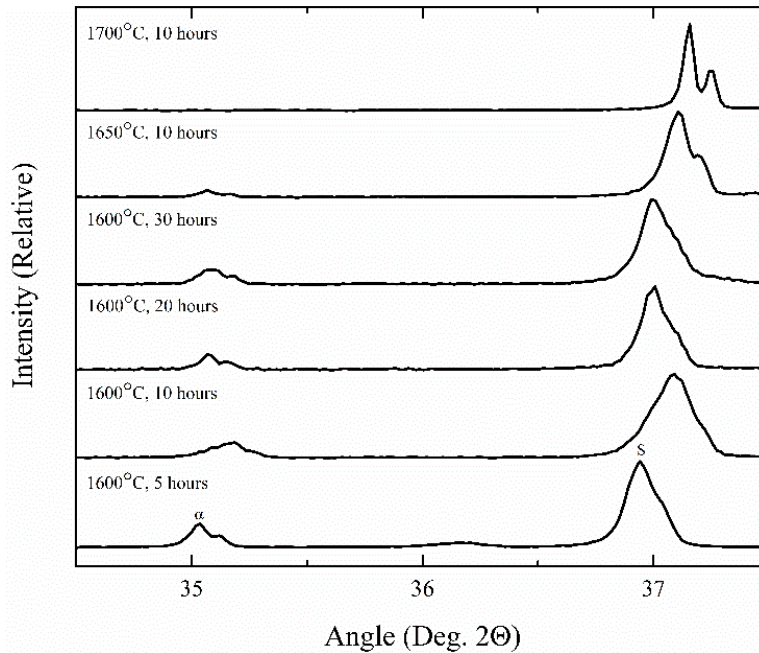


Figure 5.4 XRD patterns from Figure 5.3 are shown from 34° to 38° , showing the 104 α - Al_2O_3 peak at approximately 35° and the 311 spinel peak at approximately 37° . With the exception of the specimen heat treated at 1600°C for 10 hours, all patterns show that both peaks shift to the right with increased hot pressing, indicating a decrease in lattice parameter.

of previous works clearly showed the cubic lattice of spinel shrinks as Al_2O_3 is incorporated into the structure. Reitveld refinement of these XRD patterns indicate that the lattice parameter of spinel decreases from 8.039 \AA to 8.005 \AA , in good agreement with this summary. The a- and c-lattice parameters for α - Al_2O_3 were found to decrease from 4.760 \AA to 4.758 \AA and 12.994 \AA to 12.989 \AA , respectively. It is proposed that the decrease in the α - Al_2O_3 lattice parameters are a result of residual compressive forces created during dissolution. In an unrestricted system, one mol of Al_2O_3 dissolving into one mol of $n = 1$ spinel would produce one mol of $n = 2$ spinel and an overall volume expansion of 4.76% ^{34, 36}.

Polished cross sections of each specimen are shown in Figure 5.5, supporting the observations from XRD that second phase Al_2O_3 dissolved into the spinel matrix with increasing hot press time and temperature. For fully dense material with the overall composition $n = 2$, 38.6

vol. % Al_2O_3 is expected if no dissolution were to occur. Hot pressing for 5 hours at 1600°C results in 32.3 ± 2.8 vol. % Al_2O_3 with an average particle diameter of 11.07 ± 0.43 μm as measured with image analysis. As hot pressing time or temperature is increased, the volume of Al_2O_3 decreases, while the average particle size increases, as summarized in Table 5-2. Hot pressing at 1700°C for 10 hours results in complete dissolution of all second phase $\alpha\text{-Al}_2\text{O}_3$, although concentrations of carbon are observed where spinel- Al_2O_3 interfaces previously existed. EDS in Figure 5.6 confirms the presence of carbon at the phase boundaries. Carbon remains once the second phase $\alpha\text{-Al}_2\text{O}_3$ has completely dissolved, as shown in Figure 5.7. Hot pressing the $\gamma\text{-Al}_2\text{O}_3$ –spinel powder at 1600°C for 5 hours results in 26.0 ± 2.8 vol. % second phase particles with an average diameter of 11.3 ± 1.9 μm , similar to the $\alpha\text{-Al}_2\text{O}_3$ –spinel powder pressed under identical conditions.

It was noted that the observed Al_2O_3 particles ($7.1 - 13.4$ μm) were large compared to the starting particle sizes of the powders ($0.3 - 1.8$ μm , Table 5-1), suggesting that Al_2O_3 particles cluster during the mixing and milling steps used in powder preparation, despite the precautions to ensure phase dispersion. Furthermore, the $\alpha\text{-Al}_2\text{O}_3$ –spinel material hot pressed at 1600°C showed an increase in the average particle size with increasing hot pressing time, despite the overall volume of Al_2O_3 decreasing. Together, these observations suggest that clusters of small Al_2O_3 particles are present initially and dissolve into the spinel matrix, but concurrently sinter to form larger, single Al_2O_3 particles. The evolution of small $\alpha\text{-Al}_2\text{O}_3$ clusters into fewer, larger particles was confirmed with scanning electron microscopy (Figure 5.8). Initially, smaller individual second phase particles were observed with porosity along the phase boundaries.

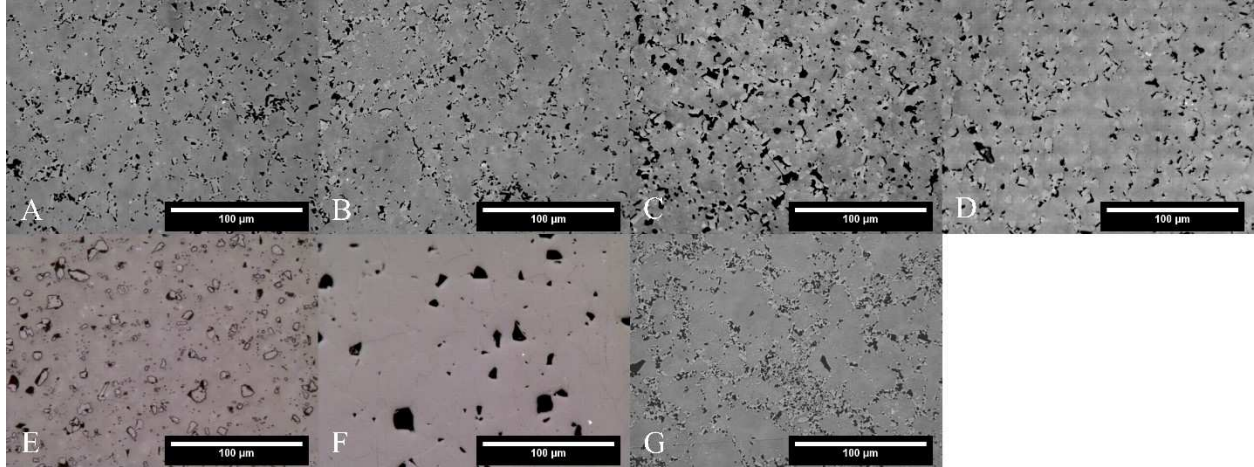


Figure 5.5 Polished surfaces are shown for α - Al_2O_3 -spinel hot pressed at 1600°C for 5, 10, 20, and 30 hours (A-D), 1650°C for 10 hours (E), and 1700°C for 10 hours (F). γ - Al_2O_3 -spinel hot pressed at 1600°C for 5 hours is also shown (G).

Table 5-2 The vol. % Al_2O_3 , mean free path between particles, measured indentation toughness, and calculated residual compressive stresses are summarized for hot pressing times and temperatures investigated. The mean free path for material hot pressed at 1700°C is the distance between carbon concentrations, as no Al_2O_3 was observed. The calculated residual compressive stress is determined after contributions from the Taya and Faber & Evans models have been subtracted

Al_2O_3	Hot Press Time (hours)	Hot Press Temperature (°C)	Vol. % Al_2O_3	Particle Size (μm)	Mean Free Path (μm)	Fracture Toughness ($\text{MPa}\sqrt{\text{m}}$)	Residual Compressive Stress (MPa)
α	5	1600	32.3±2.3	11.07±0.43	10.06±0.43	4.34±0.20	442.6
α	10	1600	33.0±2.7	12.22±1.47	10.86±1.47	3.46±0.22	259.2
α	20	1600	28.4±4.3	12.19±0.94	12.64±0.94	3.17±0.22	188.8
α	30	1600	19.7±1.3	13.38±0.54	19.33±0.54	3.01±0.16	128.7
α	10	1650	13.7±1.3	9.48±0.13	18.30±0.13	2.36±0.13	138.2
α	10	1700	0±0	11.22±0.77	45.61±0.77	2.26±0.17	14.4
γ	5	1600	26.0±2.8	11.32±1.89	12.78±1.89	3.28±0.14	206.2
α	5	1600	0±0	0±0	0±0	1.72±0.06	0

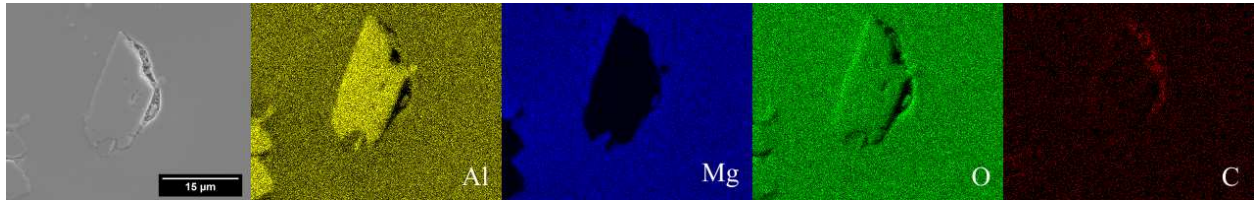


Figure 5.6 SEM and corresponding energy dispersive spectroscopy mapping of Al, Mg, O, and C is shown for α - Al_2O_3 -spinel powders hot pressed at 1650°C for 10 hours. Lack of Mg and increased concentration of Al signifies an Al_2O_3 particle within the spinel matrix. During hot pressing, C from the die diffuses into the material where it is concentrated at the interface between the two phases.

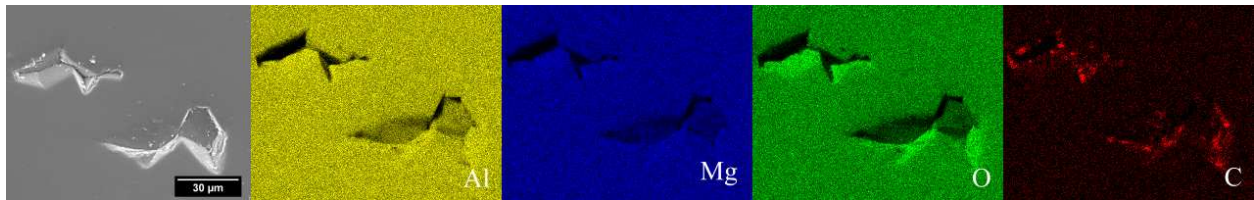


Figure 5.7 SEM and corresponding energy dispersive spectroscopy mapping of Al, Mg, O, and C is shown for α - Al_2O_3 -spinel powders hot pressed at 1700°C for 10 hours. All second phase Al_2O_3 has dissolved into the spinel matrix, but residual C at internal pores remains where second phase particles once were.

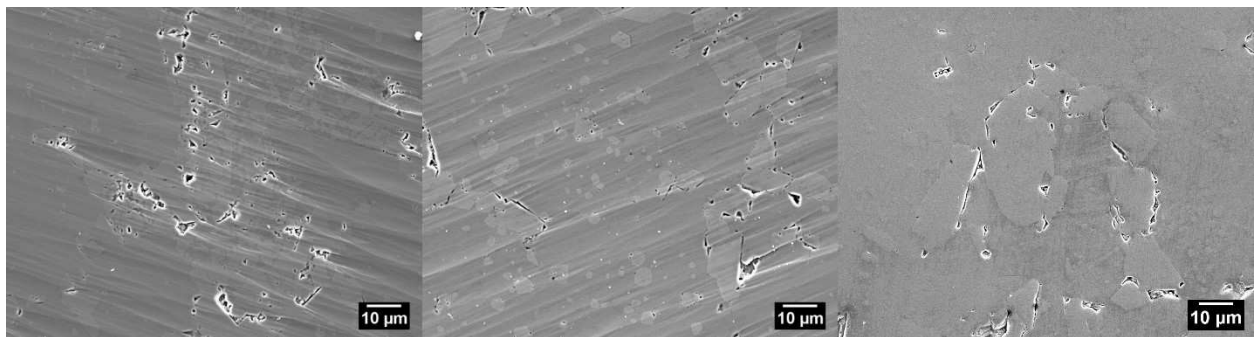


Figure 5.8 Scanning electron micrographs of lighter Al_2O_3 particles within a dark spinel matrix are shown for material hot pressed at 1600°C for 5 (left), 20 (middle), and 30 (right) hours.

Fewer, larger particles were observed with increasing hot pressing time while porosity at phase boundaries remained. The larger particles eventually dissolve into the spinel matrix, as evidenced by the decrease in both particle size and particle volume for the material hot pressed at 1650°C and 1700°C for 10 hours.

The average distance between the centers of Al₂O₃ particles, λ , for each specimen was determined using the equation^{7, 39}

$$\lambda = \frac{1.085d}{\sqrt{f_p}} \quad (5.2)$$

where d is the average particle diameter and f_p is the volume fraction of particles within the matrix. The mean free path between particles, or the distance from the edge of one particle to the edge of another, was therefore estimated as $\lambda - d$. For α -Al₂O₃-spinel material hot pressed at 1600°C for 5 hours the mean free path was determined to be $10.06 \pm 0.43 \mu\text{m}$ and increases with increasing dissolution as summarized in Table 5-2. It should be noted that in the case of the material hot pressed at 1700°C, the spacing describes the distance between concentrations of carbon, as no second phase Al₂O₃ particles were detected.

5.4.2 Mechanical properties

The fracture toughness was highest for the composites with the largest volume fraction of Al₂O₃ (Table 5-2). With decreasing volume fraction of Al₂O₃ at longer hot pressing times and higher temperatures, the fracture toughness monotonically decreased. Table 5-2 also shows that the toughness directly corresponds to the mean free path between the Al₂O₃ particles, a correlation that would be expected if a crack deflection type mechanism is operative⁴.

Representative indents shown in Figure 5.9 demonstrate that the cracks interact with the Al₂O₃ particles. The fracture toughness is shown as a function of mean free path in Figure 5.10. The

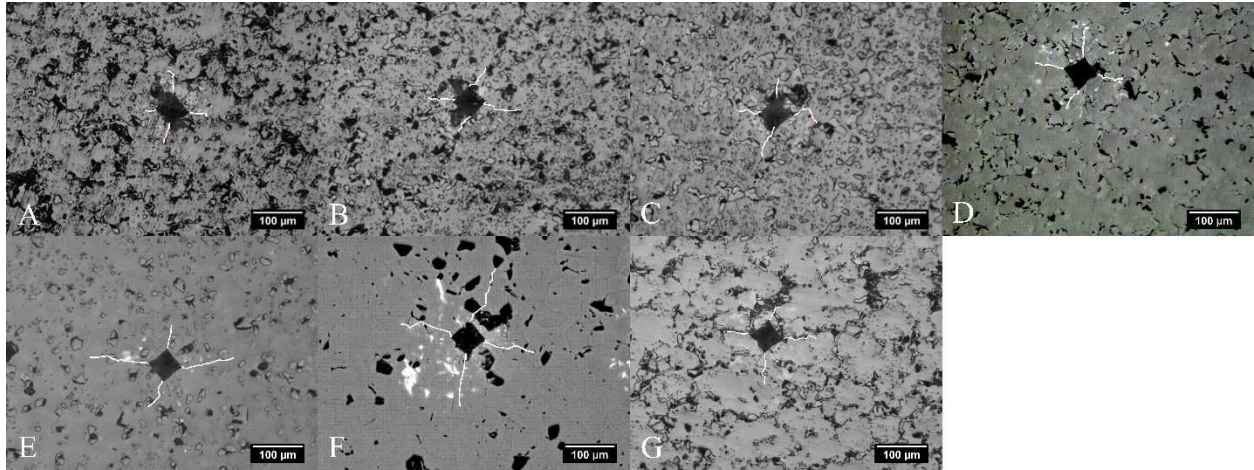


Figure 5.9 Vickers indents are shown in material hot pressed at 1600°C for 5, 10, 20, and 30 hours (A-D), 1650°C for 10 hours (E), and 1700°C for 10 hours (F). γ -Al₂O₃-spinel hot pressed at 1600°C for 5 hours is also shown (G). Images are enhanced to show cracks from indentation in white.

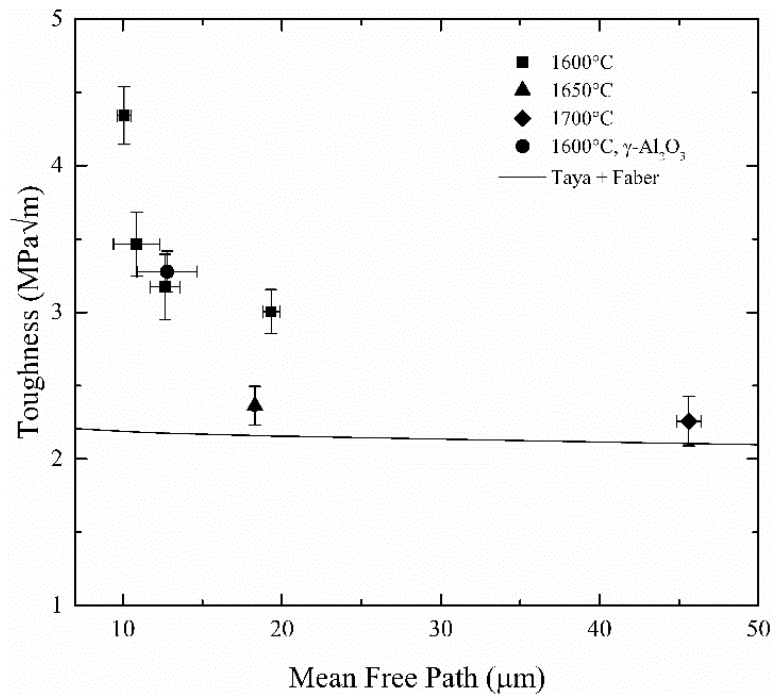


Figure 5.10 The measured indentation toughness is shown as a function of the mean free path between second phase Al₂O₃ particles. Combined CTE mismatch and crack deflection mechanisms are expected to produce toughness values modeled by the solid line.

lowest fracture toughness is the specimen in which all the Al_2O_3 has dissolved within limits of detection of this study (10 hours at 1700°C). The lower bound toughness, $2.26 \pm 0.17 \text{ MPa}\sqrt{\text{m}}$, is significantly higher than that ($1.72 \pm 0.06 \text{ MPa}\sqrt{\text{m}}$) for dense spinel of the same overall composition ($n = 2$) prepared by a conventional hot-pressing/hot isostatically pressing route, the latter measured by both the method of Anstis, et al, and the chevron notch technique by the present authors³⁶ (Table 4-1). Even though all the Al_2O_3 is dissolved, there must be some microstructure alteration that gives rise to toughening. It is hypothesized that the volume expansion inherent with the dissolution of Al_2O_3 into spinel leads to a compressive/tensile stress field that corresponds to the original spacing of Al_2O_3 particles. For composites in which Al_2O_3 particles are still present, two additional toughening mechanisms may be operative, one due to particulate crack deflection, the other due to a thermal residual stress field arising from the difference in coefficient of thermal expansion between Al_2O_3 and spinel.

According to Faber and Evans⁴, for uniformly distributed, spherical particles accounting for 10-30 vol. % of the composite material, crack deflection may increase the fracture toughness 1.12 to 1.15 times compared to a single phase monolith. Taya⁷ proposed that a composite material might form significant residual stresses from CTE mismatch during cooling, which could be modeled by the resulting stress on the matrix, q , and the mean free path between second phase particles, $\lambda - d$.

$$\Delta K_I = 2q \sqrt{\frac{2(\lambda - d)}{\pi}} \quad (5.3)$$

In this model, q is determined by

$$q = \frac{2E_m f_p B \alpha}{A} \quad (5.4)$$

where E_m and f_p are the elastic modulus of the matrix and the volume fraction of second phase particles. The term α represents the misfit strain caused by the difference in thermal expansion between Al_2O_3 and spinel. The constants A and B are dependent on the particulate volume fraction, elastic moduli, and Poisson's ratio of the matrix and particle materials:

$$A = (1 - f_p)(B + 2)(1 + v_m) + 3Bf_p(1 - v_m) \quad (5.5)$$

$$B = \frac{(1+v_m)(E_p)}{(1-2v_p)(E_m)} \quad (5.6)$$

Nielsen⁴⁰ determined the mean coefficients of thermal expansion (CTE) from 20 – 1600°C for Al_2O_3 and spinel to be $9.83 \times 10^{-6} \text{ C}^{-1}$ and $9.95 \times 10^{-6} \text{ C}^{-1}$, respectively. An elastic modulus and Poisson's ratio, E_m and v_m , of 275 GPa and 0.26 were assumed for spinel⁴¹ while a modulus and Poisson's ratio, E_p and v_p , of 344.5 GPa and 0.27 were assumed for α - Al_2O_3 ⁴². Because of the similarities in CTE and Poisson's ratio for the two materials in this system, stresses from thermal mismatch are expected to enhance the fracture toughness by a maximum of 4 %. As shown in Figure 5.10, the contributions to toughness from the combined Faber & Evans and Taya models underestimate the experimental data and fail to explain the improved toughness observed in the single phase material in this study compared to the previous study.

If it is assumed that additional residual stress arises due to the volume expansion arising from dissolution, then the toughness is higher than that predicted with the Faber & Evans and Taya models. When a volumetric strain of 4.76 % is used to replace the misfit strain, α , in Taya's model, the predicted residual stress is 3.4 GPa. To estimate the actual residual stress after accounting for crack deflection and CTE mismatch stresses, the measured fracture toughness and particle spacing were used to determine the stress, q , from the Taya model (Equation 5.3).

Results of this calculation are included in Table 5-2. Because the estimated stresses are much

less than the predicted stress of 3.4 GPa, it is obvious that stress relaxation at elevated temperature must be active. A maximum residual stress of 443 MPa was determined for α - Al_2O_3 -spinel material hot pressed at 1600°C for 5 hours and a minimum stress of 14.4 MPa was determined for the same material hot pressed at 1700°C for 10 hours, for which complete dissolution had occurred. The compressive stress in the latter explains the improvement in toughness compared to material from the previous study and reveals that creep does not completely alleviate the volumetric phase transition expansion stresses even at temperatures as high as 1700°C.

The decrease in residual stress with increasing time and temperature of hot pressing is explained by the dissipation of the stress fields surrounding second Al_2O_3 particles, as illustrated in Figure 5.11. As the particles dissolve into the spinel matrix, the compressive stresses develop in the regions immediately adjacent to the particles. These regions of Al-rich spine ($n > 1$) are highly stressed but small in size. When the mean free path between the particles (or cluster of particles) is small, a higher concentration of Al_2O_3 is present and thus a larger volume expansion occurs here. As dissolution at high temperature continues, Al_2O_3 continues to dissolve while creep allows the stresses concentrated near particles to dissipate more uniformly into the matrix. The current study shows that residual compressive stresses can be retained even after complete dissolution of the second phase particles has been achieved, but even greater enhancements to fracture toughness may be realized if some amount of second phase Al_2O_3 is left undissolved.

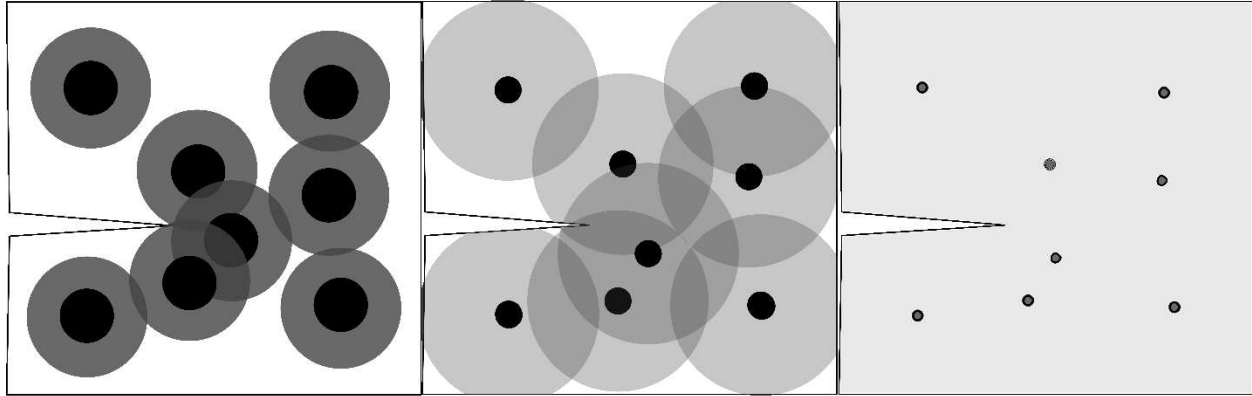


Figure 5.11 Black Al_2O_3 particles are shown dissolving into the spinel matrix, creating grey regions of Al-rich spinel (left). Continued dissolution results in smaller particles spread farther apart (middle), until complete dissolution and a uniform stoichiometry and stress distribution is achieved (right). The dissipation of stress concentrations results in increased crack propagation and lower fracture toughness.

5.5 Conclusions

The fracture toughness of a composite Al_2O_3 -spinel material with the overall composition $\text{MgO}\cdot 2\text{Al}_2\text{O}_3$ was investigated. Hot pressing time and temperature were varied to allow dissolution of the second phase into the spinel matrix. Toughness decreased with increased dissolution as the mean free path between second phase particles increased. However, upon complete dissolution, the toughness of the single phase material was still higher than the toughness measured for material of the same composition densified from single phase powders. The toughness increase could not be described simply due to crack deflection and thermal expansion mismatch. The volume expansion due to dissolution of Al_2O_3 into spinel is responsible for some of the toughness.

The current work demonstrates that the toughness of magnesium aluminate spinel can be increased by the presence of second phase Al_2O_3 , and that the structure of the Al_2O_3 may be modified through customized densification parameters. If the starting powders are mixed more homogeneously to allow direct dissolution of Al_2O_3 into the matrix rather than clusters growing to

larger particles first, and if densification aids and proper powder shielding are introduced to remove porosity and reduce carbon diffusion, the current work suggests that it is possible to create a toughened spinel composite for transparent armor applications.

5.6 Acknowledgements

This work was made possible through funding from Corning Incorporated.

5.7 References

- ¹ B. Budiansky, J.C. Amazigo, and A.G. Evans, “Small-scale crack bridging and the fracture toughness of particulate-reinforced ceramics,” *J. Mech. Phys. Solids*, **36** [2] 167–187 (1988).
- ² J. Rodel, “Interaction between crack deflection and crack bridging,” *J. Eur. Ceram. Soc.*, **10** [3] 143–150 (1992).
- ³ C.B. Huang, T.C. Lu, L. Bin Lin, M.Y. Lei, and C.X. Huang, “A Study on Toughening and Strengthening of Mg-Al Spinel Transparent Ceramics,” *Key Eng. Mater.*, **336–338** 1207–1210 (2007).
- ⁴ K.T. Faber and A.G. Evans, “Crack deflection processes-I. Theory,” *Acta Metall.*, **31** [4] 565–576 (1983).
- ⁵ Y. Chou and D.J. Green, “Silicon Carbide Platelet/Alumina Composites: II, Mechanical Properties,” *J. Am. Ceram. Soc.*, **76** [6] 1452–1458 (1993).
- ⁶ Y. Wang, K.L. Duncan, E.D. Wachsman, and F. Ebrahimi, “Effects of Reduction Treatment on Fracture Properties of Cerium Oxide,” *J. Am. Ceram. Soc.*, **3914** (2007).
- ⁷ M. Taya, S. Hayashi, A.S. Kobayashi, and H.S. Yoon, “Toughening of a Particulate-Reinforced Ceramic-Matrix Composite by Thermal Residual Stress,” *J. Am. Ceram. Soc.*, **73** [5] 1382–1391 (1990).
- ⁸ G.L. Messing and A.J. Stevenson, “Toward Pore-Free Ceramics,” *Science (80-.)*, **322** [October] 383–384 (2008).
- ⁹ A. Krell, J. Klimke, and T. Hutzler, “Transparent compact ceramics: Inherent physical issues,” *Opt. Mater. (Amst.)*, **31** [8] 1144–1150 (2009).
- ¹⁰ A. Ghosh, R. Sarkar, B. Mukherjee, and S.K. Das, “Effect of spinel content on the properties of magnesia-spinel composite refractory,” *J. Eur. Ceram. Soc.*, **24** [7] 2079–

- 2085 (2004).
- 11 R. Sarkar, A. Ghosh, and S.K. Das, "Reaction sintered magnesia rich magnesium aluminate spinel: Effect of alumina reactivity," *Ceram. Int.*, **29** [4] 407–411 (2003).
 - 12 M. Rubat Du Merac, H.J. Kleebe, M.M. Muller, and I.E. Reimanis, "Fifty years of research and development coming to fruition; Unraveling the complex interactions during processing of transparent magnesium aluminate (MgAl_2O_4) spinel," *J. Am. Ceram. Soc.*, **96** [11] 3341–3365 (2013).
 - 13 I. Ganesh, "A review on magnesium aluminate (MgAl_2O_4) spinel: synthesis, processing and applications," *Int. Mater. Rev.*, **58** [2] 63–112 (2012).
 - 14 A. Goldstein, "Correlation between MgAl_2O_4 -spinel structure, processing factors and functional properties of transparent parts (progress review)," *J. Eur. Ceram. Soc.*, **32** [11] 2869–2886 (2012).
 - 15 A.A. DiGiovanni, L. Fehrenbacher, and D.W. Roy, "Hard Domes and Windows from Magnesium Aluminate Spinel;" pp. 56–63 in *Wind. Dome Technol. Mater.* Edited by R.W. Tustison. SPIE- The International Society for Optical Engineering, Orlando, 2005.
 - 16 D.C. Harris, "History and development of polycrystalline optical spinel in the U.S.;" pp. 1–22 in *Wind. Dome Technol. Mater.* Edited by R.W. Tustison. SPIE- The International Society for Optical Engineering, Orlando, 2005.
 - 17 N. Benameur, G. Bernard-Granger, A. Addad, S. Raffy, and C. Guizard, "Sintering Analysis of a Fine-Grained Alumina-Magnesia Spinel Powder," *J. Am. Ceram. Soc.*, **94** [5] 1388–1396 (2011).
 - 18 A. Krell, J. Klimke, and T. Hutzler, "Advanced spinel and sub- μm Al_2O_3 for transparent armour applications," *J. Eur. Ceram. Soc.*, **29** [2] 275–281 (2009).
 - 19 J.A. Salem, "Transparent armor ceramics as spacecraft windows," *J. Am. Ceram. Soc.*, **96** [1] 281–289 (2013).
 - 20 M. Shimada, T. Endo, T. Saito, and T. Sato, "Fabrication of transparent spinel polycrystalline materials," *Mater. Lett.*, **28** [October] 413–415 (1996).
 - 21 O. Tokariev, L. Schnetter, T. Beck, and J. Malzbender, "Grain size effect on the mechanical properties of transparent spinel ceramics," *J. Eur. Ceram. Soc.*, **33** [4] 749–757 (2013).
 - 22 R. Apetz and M.P.B. Bruggen, "Transparent Alumina: A Light-Scattering Model," *J. Am. Ceram. Soc.*, **86** [3] 480–486 (2003).
 - 23 I. Yamashita, H. Nagayama, and K. Tsukuma, "Transmission Properties of Translucent

- Polycrystalline Alumina,” *J. Am. Ceram. Soc.*, **91** [8] 2611–2616 (2008).
- 24 B. Hallstedt, “Thermodynamic Assessment of the System MgO-Al₂O₃,” *J. Am. Ceram. Soc.*, **75** [6] 1497–1507 (1992).
- 25 W.T. Donlon, T.E. Mitchell, and A.H. Heuer, “Precipitation in non-stoichiometric spinel,” *J. Mater. Sci.*, **17** 1389–1397 (1982).
- 26 S.T. Murphy, C.A. Gilbert, R. Smith, T.E. Mitchell, and R.W. Grimes, “Non-stoichiometry in MgAl₂O₄ spinel,” *Philos. Mag.*, **90** [10] 1297–1305 (2010).
- 27 V. Erukhimovitch, Y. Mordekoviz, and S. Hayun, “Spectroscopic study of ordering in non-stoichiometric magnesium aluminate spinel,” *Am. Mineral.*, **100** 1744–1751 (2015).
- 28 M.H. Lewis, “Precipitation in non-stoichiometric spinel crystals,” *Philos. Mag.*, **20** 958–998 (1969).
- 29 P.C. Panda and R. Raj, “Kinetics of Precipitation of α -Al₂O₃ in Polycrystalline Supersaturated MgO•2Al₂O₃ Spinel Solid Solution,” *J. Am. Ceram. Soc.*, **69** [5] 365–73 (1986).
- 30 A.C. Sutorik, G. Gilde, J.J. Swab, C. Cooper, R. Gamble, and E. Shanholtz, “Transparent Solid Solution Magnesium Aluminate Spinel Polycrystalline Ceramic with the Alumina-Rich Composition MgO•1.2 Al₂O₃,” *J. Am. Ceram. Soc.*, **95** [2] 636–643 (2012).
- 31 A.C. Sutorik, G. Gilde, C. Cooper, J. Wright, and C. Hilton, “The Effect of Varied Amounts of LiF Sintering Aid on the Transparency of Alumina Rich Spinel Ceramic with the Composition MgO • 1.5Al₂O₃,” *J. Am. Ceram. Soc.*, **95** [6] 1807–1810 (2012).
- 32 K. Waetzig and A. Krell, “The Effect of Composition on the Optical Properties and Hardness of Transparent Al-rich MgO•nAl₂O₃ Spinel Ceramics,” *J. Am. Ceram. Soc.*, **99** [3] 946–953 (2016).
- 33 A.F. Dericoglu, A.R. Boccaccini, I. Dlouhy, and Y. Kagawa, “Effect of Chemical Composition on the Optical Properties and Fracture Toughness of Transparent Magnesium Aluminate Spinel Ceramics,” *Mater. Trans.*, **46** [5] 996–1003 (2005).
- 34 J.A. Miller, I.E. Reimanis, W. Miao, and A.C. Sutorik, “Diffusion limited precipitation of alumina in magnesium aluminate spinel,” *J. Am. Ceram. Soc.*, **1** [6] To Be Published (2016).
- 35 J.A. Miller, I.E. Reimanis, W. Miao, A.C. Sutorik, and J.A. Salem, “Mechanical and Optical Properties in Precipitated Regions of Alumina-Rich Magnesium Aluminate Spinel,” *Int. J. Appl. Ceram. Technol.*, To Be Published (n.d.).
- 36 G.R. Anstis, P. Chantikul, B.R. Lawn, and D.B. Marshall, “A Critical Evaluation of

- Indentation Techniques for Measuring Fracture Toughness: I, Direct Crack Measurements,” *J. Am. Ceram. Soc.*, **64** [September] 533–538 (1981).
- 37 F.W. DYNYS and J.W. HALLORAN, “Alpha Alumina Formation in Alum-Derived Gamma Alumina,” *J. Am. Ceram. Soc.*, **65** [9] 442–448 (1982).
- 38 Y. Chiang and D. Kingery, “Grain-Boundary Migration in Nonstoichiometric Solid Solutions of Magnesium Aluminate Spinel: I, Grain Growth Studies,” *J. Am. Ceram. Soc.*, **77** 271–277 (1989).
- 39 G. Leroy, J.D. Embury, G. Edwards, and M.F. Ashby, “A MODEL OF DUCTILE FRACTURE BASED ON THE NUCLEATION AND GROWTH OF VOIDS,” *Acta Metall.*, **29** 1509–1522 (1981).
- 40 T.H. Nielsen and M.H. Leipold, “Thermal Expansion in Air of Ceramic Oxides at 2200°C,” *J. Am. Ceram. Soc.*, **46** [8] 381–387 (1963).
- 41 D.C. Harris, *Materials for Infrared Windows and Domes: Properties and Performance*. SPIE- The International Society for Optical Engineering, Bellingham, Washington, 1999.
- 42 J.S. Browder, S.S. Ballard, and P. Klocek, “Physical Properties of Infrared Optical Materials;” pp. 402–405 in *Handb. Infrared Opt. Mater.*, First. Edited by P. Klocek. Marcel Dekker Inc., New York, NY, 1991.

CHAPTER 6

SUMMARY AND CONCLUSIONS

Magnesium aluminate spinel is among a short list of potential materials to be considered for transparent armor applications; the relatively low fracture toughness of spinel presents the largest obstacle preventing its wide scale use. This thesis demonstrates that not only is it possible to introduce second phase Al_2O_3 to enhance the toughness of spinel, but that the structure of the composite can be altered through processing routines achievable in industrial manufacturing processes. Such structural manipulation can be utilized to minimize light scattering caused by the second phase particles used to enhance the toughness, and ultimately create a toughened, transparent material for armor applications.

In chapter 3, the ability to precipitate second phase Al_2O_3 from Al-rich spinel was demonstrated. The study determined that densification in reducing environments, a routine commonly used to produce transparent spinel, stabilizes single phase, Al-rich spinel until oxygen is reintroduced. As a result, controlling the process by which oxygen is restored can lead to selective precipitation at the surface or in the core of the densified part. In addition, the kinetics of surface precipitation were investigated, revealing a linear rate of oxygen diffusion that could be delayed by introducing a barrier between the surface of the part and the furnace atmosphere. The work in this chapter demonstrates that precipitation is diffusion limited in this case, but changing the environment during densification will result the reaction limited kinetics observed in other studies. Together, such revelations establish a framework in which the microstructure can be customized for specific applications.

Once it was established that the location and evolution of second phase Al_2O_3 could be controlled, the effects of the second phase on the mechanical and optical properties of the

composite material were investigated. Chapter 4 demonstrates the toughness in precipitated regions is improved compared to the single phase, Al-rich material due to increased crack tortuosity along phase boundaries. However, microhardness and nanohardness measurements revealed regions of tensile stress immediately adjacent to the precipitated regions because of volume contraction that occurs during precipitation. Such contraction led to porosity, decreasing the transmission with increased precipitation. However, this chapter demonstrated that impact resistant surfaces could be created and loss in transmission would be minimal if the precipitation layer remained thin.

The observation of residual tensile stresses from the precipitation process alluded to the theory that reversing the process might lead to desirable compressive stresses. Chapter 5 therefore explores the toughness of composite Al_2O_3 -spinel material where second phase Al_2O_3 is present initially and dissolves into the matrix during densification. Experimental data followed trends proposed by existing models for crack deflection in composite ceramic systems. However, these models failed to explain the magnitude of the increase observed in this study, indicating additional compressive stresses were present within the material as a result of volume expansion during dissolution. Calculating the residual stresses through an adaptation of Taya's residual stress model determined the stresses to be less than expected from the volume expansion produced, indicating that a large portion of the stress was relieved through creep at the high processing temperatures.

When these separate chapters are examined together as a single thesis, the work contained within demonstrates that magnesium aluminate spinel can be toughened by the introduction of second phase Al_2O_3 . However, the resulting toughness is dependent upon the processing route.

6.1 Toughened magnesium aluminate spinel

Whether starting with a single phase and precipitating Al_2O_3 out or starting with a composite and dissolving Al_2O_3 into the spinel matrix, the work in this thesis determined the second phase that crack deflection and increased crack tortuosity are active mechanisms in both systems and account for a portion of the increased toughness observed. Additional toughening mechanisms are activated if second phase Al_2O_3 is present initially and dissolved into the spinel matrix; compressive stresses form as the more dense second phase particles dissolve into the less dense matrix.

6.2 Controlled evolution of second phase particles

Not only does this thesis elucidate the toughening mechanisms responsible for the increased toughness observed in non-stoichiometric spinel, but the ability to control the location and magnitude of these particles is also demonstrated. Using parameters available in industrial processing, it is possible to control the location and morphology of second phase particles. The most straight-forward approach is to introduce second phase Al_2O_3 particles at desired locations prior to densification; for example, uniform dispersion of second phase particles will result in uniform toughness at the expense of introducing light-scattering bodies throughout the bulk material, provided the material is densified above the solvus temperatures. Densification at these elevated temperatures can reduce the size of second phase particles to decrease light scattering while maintaining a portion of the residual compressive stresses created. Such a routine lends itself to applications that prioritize uniform toughness and can be satisfied with windows of simple shapes. Flat vehicle windows might be made in this fashion, but this process may lead to over-engineered missile radomes. Because radomes are designed to defend against much smaller dust and water particulates, a toughened surface may provide adequate protection with minimal

light scattering. However, the curvature of radomes greatly complicates the process of introducing second phase Al_2O_3 uniformly across the entire surface of the part, making surface precipitation an attractive route. In comparison to the previous processing route for dissolution, precipitation requires a subsequent heat treatment in air after densification. The processes to achieve varied microstructures from precipitation are shown schematically in Figure 6.1.

Both surface and core precipitation were demonstrated in this thesis. While not directly applicable to missile radome applications, the ability to create uniform precipitation, or precipitation only at the core of the material provided valuable insight into the mechanisms controlling precipitation and how the rates of such mechanism can be tailored for missile radome applications. Furthermore, the revelations of this study serve as a model for controlled precipitation in other oxide ceramic systems.

6.3 Future research

As with many scientific endeavors, the undertaking of this project has not only provided new knowledge but exposed new questions that had yet to be asked. In order to begin to understand the complicated precipitation and dissolution mechanisms at work, a simplified system was investigated. Now that this system is better understood, further research of varied processing conditions and the use of densification agents may lead to further improvements upon the results presented here.

6.3.1 Varied processing conditions

This project emphasized microstructural control using processes achievable in industrial manufacturing, but only a small portion of the available parameter space has been investigated thus far. For example, only stoichiometric ($n = 1$) or Al-rich ($n = 2$) compositions are presented

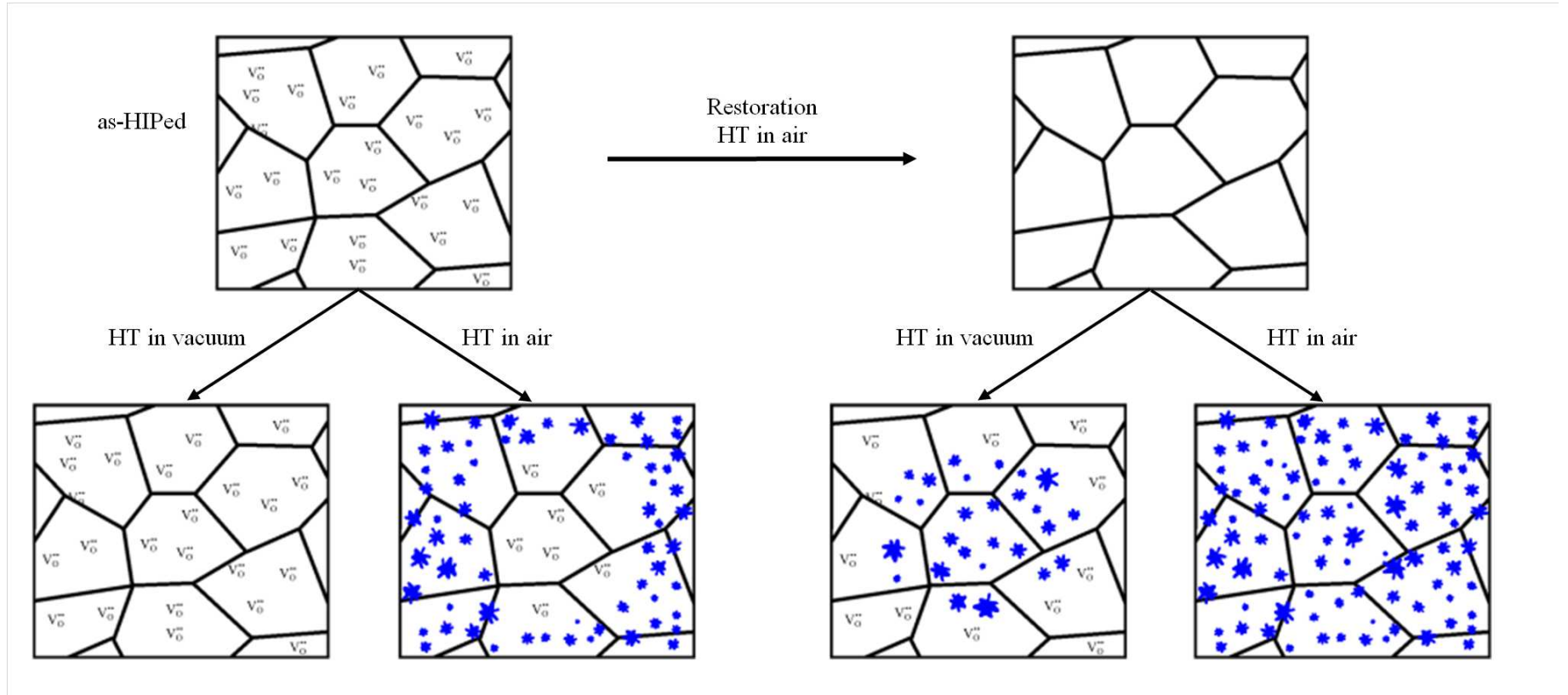


Figure 6.1. The varied microstructures possible through precipitation of Al_2O_3 are shown schematically. Oxygen vacancies are present after HIPing in reducing environments, stabilizing the single phase structure. Heat treatment in vacuum will not result in precipitation. Heat treatment in air below the solvus temperature promotes precipitation as oxygen diffuses from the atmosphere into the surface. Heat treatment in air above the solvus temperature also results in diffusion of oxygen and restores oxygen vacancies, but no precipitation occurs. Subsequent heat treatment of this restored structure will result in uniform precipitation if the material is heat treated in air. If the material is heat treated in vacuum instead, oxygen vacancies are again created at the surface, stabilizing the single phase spinel as precipitation occurs in the bulk.

in this thesis. While sufficient to provide a proof of concept, further optimization may be realized with different compositions; the effect of Al_2O_3 concentration on the precipitation or dissolution driving force, or the optimal concentration to uniformly distribute particles without clustering are both projects worth investigating, albeit time consuming. It should also be mentioned that Mg-rich compositions have scarcely been investigated in existing literature at all, although this is likely due, in part, to the limited solubility of MgO in spinel compared to Al_2O_3 .

Similar to varied stoichiometries, varying the PO_2 levels during processing is possible in industrial manufacturing, but not explored in depth here. It was proven that vacuum levels typical of densification routines are sufficient to remove oxygen from the spinel structure and that atmosphere is sufficient to allow oxygen to be reincorporated, but diffusion rates and equilibrium oxygen concentrations might be further optimized by exploring intermediate PO_2 levels.

6.3.2 Controlling impurities and porosity

In viewing this project in its completion, the biggest obstacle remaining in implementing second phase Al_2O_3 to toughen spinel is the detriment to transparency caused by light scattering at pores, impurities, and phase boundaries. In other studies, the addition of densification aids such as LiF have been shown to dramatically improve transparency in spinel by removing porosity and impurity elements, but the mechanism controlling such densification aids are not well understood and initial work in this project revealed that their presence greatly complicated the mechanisms controlling densification, grain growth, precipitation or dissolution, and oxygen diffusion. Now that these mechanisms are better understood for stoichiometric and Al-spinel, a systematic study of including material with LiF would be beneficial.

The work presented in this thesis provides the framework necessary to pursue the answers to such enquiries. While optimal processing conditions or acceptable transmission levels may be application dependent and require case-by-case analysis, this thesis demonstrates that it is possible to customize the microstructure of Al_2O_3 -spinel composites to satisfy these individual requirements. Such flexibility within a single material system may not only lend magnesium aluminate spinel to the applications presented here, but also to other applications yet to be discovered.

APPENDIX A

THEORETICAL DENSITY OF AL-RICH MAGNESIUM ALUMINATE SPINEL

During the execution of experiments for this thesis, the formation of porosity was observed during precipitation, as discussed in chapters 3 and 4. It is clear that the porosity is the result of volume contraction as the more dense $\alpha\text{-Al}_2\text{O}_3$ precipitated from the spinel. However, because the theoretical density of Al-rich spinel is dependent on the stoichiometry of the material, exact values are not presented in literature and thus calculations were necessary to demonstrate the amount of porosity to be expected. Such calculations are presented here, based on the assumption that one mol of al-rich spinel ($n = 2$), precipitates completely and uniformly into one mole of stoichiometric spinel ($n = 1$) and one mol of $\alpha\text{-Al}_2\text{O}_3$. For simplicity, it is also assumed that there is no inversion of the cation sites in the spinel.

A.1 Lattice parameters

The first step in determining the theoretical density of compound is to determine the lattice parameters that define the unit cell. Chiang and Kingery¹, among others, have demonstrated the lattice parameter for cubic, stoichiometric spinel to be 8.083 Å, and that the lattice parameter decreases with increasing Al_2O_3 content. Works by Viertel^{2,3} discovered a linear relationship between the lattice parameter and n for non-stoichiometric spinel of the overall composition $\text{MgO}\cdot n\text{Al}_2\text{O}_3$ as defined by

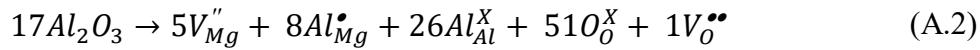
$$n = \frac{0.86109 - a_o}{3a_o - 2.37195} \quad (\text{A.1})$$

resulting in a calculated lattice parameter of 8.0826 Å and 8.0071 Å for $n = 1$ and $n = 2$ compositions, respectively. Using this value of 8.026 Å for stoichiometric spinel, the theoretical

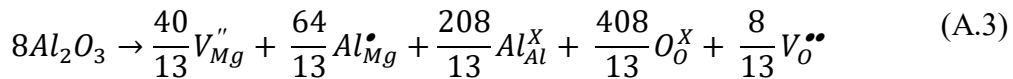
density is calculated to be 3.58 g/cm³, matching the measured densities for spinel achieving near 100% density⁴.

A.2 Unit cells of constituent phases

Both the unit cells for stoichiometric spinel⁵ and α -Al₂O₃⁶ are well known; meaning that the final density of the composite material is easily determined. However, the unit cell of non-stoichiometric spinel is dependent upon the assumed defect reaction to describe the incorporation of excess Al₂O₃ into the spinel structure. Okuyama⁷ proposes that 17 units of Al₂O₃ can be restructured to form 13 units of the spinel structure by creating 5 vacancies on Mg sites and a single vacancy on an O site



Because one unit cell of stoichiometric spinel contains 8 molecular units (56 atoms in total), 8 units of Al₂O₃ must be added to the unit cell to create an overall composition of n = 2. These 8 units of Al₂O₃ will form ⁸/₁₃ of the 13 units proposed by Okuyama, so the above equation is modified to express the sites created when 8 mols of Al₂O₃ are restructured

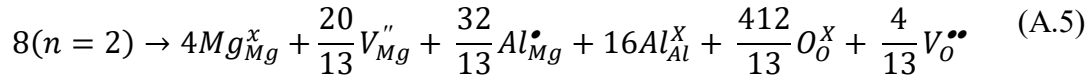


Combining the above defected structure with 8 mols of stoichiometric spinel to form 16 units of n = 2 material results in the following defect reaction



Reducing the above equation by a factor of 2 results in 8 molecular units of n = 2 spinel, which is

one unit cell



The spinel structure is maintained, as a total of 8 Mg sites, 16 Al sites, and 32 O sites are present. From the above defect reaction for a single unit cell of $n = 2$ spinel, the molecular weight was calculated to be 1102.4 g/mol (compared to 1138.0 for stoichiometric spinel). Applying the calculated lattice parameter of 8.0071 Å determined earlier, the theoretical density of $n = 2$ spinel is determined to be 3.56 g/cm³. This value is in good agreement another study⁸, in which a linear expansion of 5 % was determined for the dissolution of MgO and Al₂O₃ into stoichiometric spinel. This study concluded theoretical densities of 3.578 and 3.512 g/cm³ for $n = 1$ and $n = 2$ compositions, but was based on a defect structure for the dissolution of Al₂O₃ into MgO rather than into spinel.

A.3 Molecular volumes and theoretical densities

The theoretical densities calculated according to the Okuyama defect reaction are used to determine molar volumes. Al-rich, $n = 2$ spinel has a molecular weight of 244.23 g/mol and a theoretical density of 3.56 g/cm³. Therefore 1 mol of $n = 2$ spinel has a volume of 68.47 cm³. By similar calculations, 1 mol of $n = 1$ spinel and 1 mol of α -Al₂O₃ have volumes of 39.74 cm³ and 25.62 cm³, respectively, for a combined volume of 65.36 cm³. For the reaction where precipitation from 1 mole of $n = 2$ spinel results in 1 mol of $n = 1$ spinel and 1 mol α -Al₂O₃, a change in volume from 68.47 to 65.36 cm³ is expected. The difference, 3.11 cm³, results in 4.54 % porosity.

A.4 References

- ¹ Y.M. Chiang and W.D. Kingery, “Grain-boundary migration in nonstoichiometric solid solutions of magnesium aluminate spinel: I, grain growth studies,” *J. Am. Ceram. Soc.*, **72** [2] 271–277 (1989).
- ² H.U. Viertel and F. Seifert, “Thermal Stability of defect spinels in the system $\text{MgAl}_2\text{O}_4\text{-Al}_2\text{O}_3$,” *N. Jb. Miner. Abh.*, **140** [1] 89–101 (1980).
- ³ H.U. Viertel and F. Seifert, “Physical properties of defect spinels in the system $\text{MgAl}_2\text{O}_4\text{-Al}_2\text{O}_3$,” *N. Jb. Miner. Abh.*, **134** [2] 167–182 (1979).
- ⁴ C. Baudin, R. Martinez, and P. Pena, “High-Temperature Mechanical Behavior of Stoichiometric Magnesium Spinel,” *J. Am. Ceram. Soc.*, **78** [7] 1857–62 (1995).
- ⁵ K. Sickafus and J. Wills, “Structure of spinel,” *J. Am. Ceram. Soc.*, **82** [12] 3279–3292 (1999).
- ⁶ V.G. Tsirelson, M. Yu. Antipin, R.G. Gerr, R.P. Ozerov, and Y.T. Struchkov, “Ruby structure peculiarities derived from X-ray diffraction data localization of chromium atoms and electron deformation density,” *Phys. status solidi*, **87** [2] 425–433 (1985).
- ⁷ Y. Okuyama, N. Kurita, and N. Fukatsu, “Defect structure of alumina-rich nonstoichiometric magnesium aluminate spinel,” *Solid State Ionics*, **177** [1–2] 59–64 (2006).
- ⁸ I. Ganesh, “A review on magnesium aluminate (MgAl_2O_4) spinel: synthesis, processing and applications,” *Int. Mater. Rev.*, **58** [2] 63–112 (2012).

APPENDIX B

INDENTATION DATA

Due to the natural variability inherent in ceramic materials, the toughness values presented in this thesis are an average of individual indentation measurements. In order to present meaningful information, multiple measurements were made on every specimen. Invalid measurements were not considered during the analysis process.

B.1 Precipitation of Al₂O₃

Measurements and the calculated toughness for all indents made in specimens used in the precipitation study discussed in chapters 3 and 4 are presented. An image of every indent was recorded whether or not valid indentation and cracking geometry were observed. The length of the horizontal and vertical diagonal, horizontal and vertical crack, applied load, and calculated fracture toughness are also shown. The hardness values used to calculate indentation fracture toughness for $n = 1$ and $n = 2$ spinel were measured (using a load of 1 kgf) to be 12.8 GPa and 11.4 GPa, respectively. All indents shown here were made using a load of 3 kgf. For some indents, the diagonals of the indent could be measured, but the radial cracking did not meet the acceptable criterion for indentation toughness measurements. For many indents, neither the indent or radial cracks were valid for measurement. A value of “FALSE” indicates the measured diagonal and crack lengths were not valid for indentation toughness calculations.

Table B-1. All measurements of indents used to calculate indentation fracture toughness during the precipitation study are shown.

Table B-1 Continued

Indent	file name	ah (μm)	av (μm)	2ch (μm)	2cv (μm)	H (GPa)	K (MPa $\sqrt{\text{m}}$)
1	n=1.00_HIP_3kgf_5X_indent01-preload	73.6	70.3			10.5	FALSE
2	n=1.00_HIP_3kgf_10X_indent02	63.9	65.5	254.3	317.3	13.0	1.3
3	n=1.00_HIP_3kgf_10X_indent03	66.5	65.7			12.5	FALSE

Table B-1 Continued

Indent	file name	ah (μm)	av (μm)	2ch (μm)	2cv (μm)	H (GPa)	K (MPa $\sqrt{\text{m}}$)
4	n=1.00_HIP_3kgf_10X_indent04	63.2	65.4			13.2	FALSE
5	n=1.00_HIP_3kgf_10X_indent05					FALSE	FALSE
6	n=1.00_HIP_3kgf_10X_indent06					FALSE	FALSE
7	n=1.00_HIP_3kgf_10X_indent07	65.9	64.4	274.2	297.3	12.8	1.3
8	n=1.00_HIP_3kgf_10X_indent08					FALSE	FALSE
9	n=1.00_HIP_3kgf_10X_indent09					FALSE	FALSE
10	n=1.00_HIP_3kgf_10X_indent10					FALSE	FALSE
11	n=1.00_HIP_3kgf_10X_indent11					FALSE	FALSE
12	n=1.00_HIP_3kgf_10X_indent12	64.8	64.4			13.1	FALSE
13	n=1.00_HIP_3kgf_10X_indent13	60.0	63.4	271.0		14.3	1.4
14	n=1.00_HIP_3kgf_10X_indent14	66.6	68.0			12.1	FALSE
15	n=1.00_HIP_3kgf_10X_indent15					FALSE	FALSE
16	n=1.00_HIP_3kgf_10X_indent16	65.8	66.7	280.2	246.6	12.4	1.5
17	n=1.00_HIP_3kgf_10X_indent17	64.9	64.2			13.1	FALSE
18	n=1.00_HIP_3kgf_10X_indent18					FALSE	FALSE
19	n=1.00_HIP_3kgf_10X_indent19	63.9	63.8	264.8	252.5	13.4	1.5
20	n=1.00_HIP_3kgf_10X_indent20	64.3	64.4	252.1	271.9	13.2	1.5
1	n=1.00_1300C_1hr_3kgf_10X_01					FALSE	FALSE
2	n=1.00_1300C_1hr_3kgf_10X_02					FALSE	FALSE
3	n=1.00_1300C_1hr_3kgf_10X_03					FALSE	FALSE
4	n=1.00_1300C_1hr_3kgf_10X_04					FALSE	FALSE
5	n=1.00_1300C_1hr_3kgf_10X_05					FALSE	FALSE
6	n=1.00_1300C_1hr_3kgf_10X_06					FALSE	FALSE
7	n=1.00_1300C_1hr_3kgf_10X_07	65.9	64.6			12.8	FALSE
8	n=1.00_1300C_1hr_3kgf_10X_08	65.2	64.0			13.1	FALSE
9	n=1.00_1300C_1hr_3kgf_10X_09	64.0	63.4			13.4	FALSE
10	n=1.00_1300C_1hr_3kgf_10X_10					FALSE	FALSE
11	n=1.00_1300C_1hr_3kgf_10X_11					FALSE	FALSE
12	n=1.00_1300C_1hr_3kgf_10X_12					FALSE	FALSE
13	n=1.00_1300C_1hr_3kgf_10X_13					FALSE	FALSE
14	n=1.00_1300C_1hr_3kgf_10X_14					FALSE	FALSE
15	n=1.00_1300C_1hr_3kgf_10X_15					FALSE	FALSE
16	n=1.00_1300C_1hr_3kgf_10X_16					FALSE	FALSE
17	n=1.00_1300C_1hr_3kgf_10X_17					FALSE	FALSE
18	n=1.00_1300C_1hr_3kgf_10X_18	64.2	64.7	234.7	235.1	13.1	1.8
19	n=1.00_1300C_1hr_3kgf_10X_19					FALSE	FALSE
20	n=1.00_1300C_1hr_3kgf_10X_20	64.1	63.9			13.3	FALSE
21	n=1.00_1300C_1hr_3kgf_10X_21	65.2	63.6			13.2	FALSE
22	n=1.00_1300C_1hr_3kgf_10X_22	63.1	63.6			13.6	FALSE
23	n=1.00_1300C_1hr_3kgf_10X_23					FALSE	FALSE
24	n=1.00_1300C_1hr_3kgf_10X_24	63.7	63.2			13.6	FALSE
25	n=1.00_1300C_1hr_3kgf_10X_25	64.8	63.9	284.9	286.7	13.2	1.3
26	n=1.00_1300C_1hr_3kgf_10X_26	65.2	64.0	296.4	261.1	13.1	1.4

Table B-1 Continued

Indent	file name	ah (μm)	av (μm)	2ch (μm)	2cv (μm)	H (GPa)	K (MPa $\sqrt{\text{m}}$)
27	n=1.00_1300C_1hr_3kgf_10X_27	63.7	63.0			13.6	FALSE
28	n=1.00_1300C_1hr_3kgf_10X_28	62.8	63.1			13.8	FALSE
29	n=1.00_1300C_1hr_3kgf_10X_29	63.2	64.1			13.5	FALSE
30	n=1.00_1300C_1hr_3kgf_10X_30	65.7	64.1	287.9	299.7	13.0	1.3
1	n=2.00_HIP_3kgf_10X_01	67.8	69.9	243.5	260.2	11.5	1.8
2	n=2.00_HIP_3kgf_10X_02	68.4	68.7			11.6	FALSE
3	n=2.00_HIP_3kgf_10X_03	67.5	67.5	259.5	268.1	12.0	1.6
4	n=2.00_HIP_3kgf_10X_04	67.0	67.1	228.5	246.6	12.1	1.9
5	n=2.00_HIP_3kgf_10X_05	68.9	70.0			11.3	FALSE
6	n=2.00_HIP_3kgf_10X_06					FALSE	FALSE
7	n=2.00_HIP_3kgf_10X_07	67.2	67.5	220.8	268.4	12.0	1.8
8	n=2.00_HIP_3kgf_10X_08	67.1	67.4			12.1	FALSE
9	n=2.00_HIP_3kgf_10X_09	63.2	68.6	209.8	268.8	12.6	1.9
10	n=2.00_HIP_3kgf_10X_10					FALSE	FALSE
11	n=2.00_HIP_3kgf_10X_11					FALSE	FALSE
12	n=2.00_HIP_3kgf_10X_12					FALSE	FALSE
13	n=2.00_HIP_3kgf_10X_13	67.3	70.8	271.1	304.6	11.5	1.5
14	n=2.00_HIP_3kgf_10X_14					FALSE	FALSE
15	n=2.00_HIP_3kgf_10X_15					FALSE	FALSE
16	n=2.00_HIP_3kgf_10X_16					FALSE	FALSE
17	n=2.00_HIP_3kgf_10X_17					FALSE	FALSE
18	n=2.00_HIP_3kgf_10X_18					FALSE	FALSE
19	n=2.00_HIP_3kgf_10X_19					FALSE	FALSE
20	n=2.00_HIP_3kgf_10X_20					FALSE	FALSE
21	n=2.00_HIP_3kgf_10X_21					FALSE	FALSE
22	n=2.00_HIP_3kgf_10X_22					FALSE	FALSE
23	n=2.00_HIP_3kgf_10X_23					FALSE	FALSE
24	n=2.00_HIP_3kgf_10X_24					FALSE	FALSE
25	n=2.00_HIP_3kgf_10X_25					FALSE	FALSE
26	n=2.00_HIP_3kgf_10X_26					FALSE	FALSE
27	n=2.00_HIP_3kgf_10X_27					FALSE	FALSE
28	n=2.00_HIP_3kgf_10X_28	70.7	65.5	270.1	251.0	11.8	1.7
29	n=2.00_HIP_3kgf_10X_29					FALSE	FALSE
30	n=2.00_HIP_3kgf_10X_30					FALSE	FALSE
1	n=2.00_1300C_1hr_3kgf_10X_01	67.0	67.8			12.0	FALSE
2	n=2.00_1300C_1hr_3kgf_10X_02					FALSE	FALSE
3	n=2.00_1300C_1hr_3kgf_10X_03	66.6	67.8	238.9	269.7	12.1	1.7
4	n=2.00_1300C_1hr_3kgf_10X_04	72.9	69.0			10.8	FALSE
5	n=2.00_1300C_1hr_3kgf_10X_05					FALSE	FALSE
6	n=2.00_1300C_1hr_3kgf_10X_06	68.4	71.9			11.1	FALSE
7	n=2.00_1300C_1hr_3kgf_10X_07					FALSE	FALSE
8	n=2.00_1300C_1hr_3kgf_10X_08	68.4	69.2	257.4	284.9	11.5	1.6

Table B-1 Continued

Indent	file name	ah (μm)	av (μm)	2ch (μm)	2cv (μm)	H (GPa)	K (MPa $\sqrt{\text{m}}$)
9	n=2.00_1300C_1hr_3kgf_10X_09	69.6	69.8			11.2	FALSE
10	n=2.00_1300C_1hr_3kgf_10X_10	67.2	66.8			12.2	FALSE
11	n=2.00_1300C_1hr_3kgf_10X_11					FALSE	FALSE
12	n=2.00_1300C_1hr_3kgf_10X_12					FALSE	FALSE
13	n=2.00_1300C_1hr_3kgf_10X_13	66.5	67.2	276.8	244.9	12.2	1.7
14	n=2.00_1300C_1hr_3kgf_10X_14					FALSE	FALSE
15	n=2.00_1300C_1hr_3kgf_10X_15					FALSE	FALSE
16	n=2.00_1300C_1hr_3kgf_10X_16	68.7	66.2	251.8	243.3	12.0	1.8
17	n=2.00_1300C_1hr_3kgf_10X_17					FALSE	FALSE
18	n=2.00_1300C_1hr_3kgf_10X_18					FALSE	FALSE
19	n=2.00_1300C_1hr_3kgf_10X_19					FALSE	FALSE
20	n=2.00_1300C_1hr_3kgf_10X_20	68.8	69.5	269.4	274.9	11.4	1.6
21	n=2.00_1300C_1hr_3kgf_10X_21					FALSE	FALSE
22	n=2.00_1300C_1hr_3kgf_10X_22					FALSE	FALSE
23	n=2.00_1300C_1hr_3kgf_10X_23					FALSE	FALSE
24	n=2.00_1300C_1hr_3kgf_10X_24					FALSE	FALSE
25	n=2.00_1300C_1hr_3kgf_10X_25					FALSE	FALSE
26	n=2.00_1300C_1hr_3kgf_10X_26					FALSE	FALSE
27	n=2.00_1300C_1hr_3kgf_10X_27					FALSE	FALSE
28	n=2.00_1300C_1hr_3kgf_10X_28					FALSE	FALSE
29	n=2.00_1300C_1hr_3kgf_10X_29					FALSE	FALSE
30	n=2.00_1300C_1hr_3kgf_10X_30					FALSE	FALSE
1	n=2.00_1300C_11hr_3kgf_10X_1					FALSE	FALSE
2	n=2.00_1300C_11hr_3kgf_10X_2					FALSE	FALSE
3	n=2.00_1300C_11hr_3kgf_10X_3					FALSE	FALSE
4	n=2.00_1300C_11hr_3kgf_10X_4	69.4	67.4	271.7	238.9	11.7	1.7
5	n=2.00_1300C_11hr_3kgf_10X_5					FALSE	FALSE
6	n=2.00_1300C_11hr_3kgf_10X_6					FALSE	FALSE
7	n=2.00_1300C_11hr_3kgf_10X_7	67.5	66.0	317.6	255.9	12.3	1.4
8	n=2.00_1300C_11hr_3kgf_10X_8	67.5	67.7			11.9	FALSE
9	n=2.00_1300C_11hr_3kgf_10X_9	68.0	67.5			11.9	FALSE
10	n=2.00_1300C_11hr_3kgf_10X_10					FALSE	FALSE
11	n=2.00_1300C_11hr_3kgf_10X_11	68.0	68.1	257.2	279.5	11.8	1.6
12	n=2.00_1300C_11hr_3kgf_10X_12					FALSE	FALSE
13	n=2.00_1300C_11hr_3kgf_10X_13					FALSE	FALSE
14	n=2.00_1300C_11hr_3kgf_10X_14					FALSE	FALSE
15	n=2.00_1300C_11hr_3kgf_10X_15					FALSE	FALSE
16	n=2.00_1300C_11hr_3kgf_10X_16					FALSE	FALSE
17	n=2.00_1300C_11hr_3kgf_10X_17					FALSE	FALSE
18	n=2.00_1300C_11hr_3kgf_10X_18	69.4	68.6	291.2	250.5	11.5	1.6
19	n=2.00_1300C_11hr_3kgf_10X_19	69.9	67.7	265.0	248.7	11.5	1.7
20	n=2.00_1300C_11hr_3kgf_10X_20					FALSE	FALSE
21	n=2.00_1300C_11hr_3kgf_10X_21					FALSE	FALSE

Table B-1 Continued

Indent	file name	ah (μm)	av (μm)	2ch (μm)	2cv (μm)	H (GPa)	K (MPa $\sqrt{\text{m}}$)
22	n=2.00_1300C_11hr_3kgf_10X_22					FALSE	FALSE
23	n=2.00_1300C_11hr_3kgf_10X_23					FALSE	FALSE
24	n=2.00_1300C_11hr_3kgf_10X_24					FALSE	FALSE
25	n=2.00_1300C_11hr_3kgf_10X_25					FALSE	FALSE
26	n=2.00_1300C_11hr_3kgf_10X_26					FALSE	FALSE
27	n=2.00_1300C_11hr_3kgf_10X_27					FALSE	FALSE
28	n=2.00_1300C_11hr_3kgf_10X_28					FALSE	FALSE
29	n=2.00_1300C_11hr_3kgf_10X_29					FALSE	FALSE
30	n=2.00_1300C_11hr_3kgf_10X_30	68.0	68.6	310.9	293.5	11.7	1.4
31	n=2.00_1300C_11hr_3kgf_10X_31	67.4	70.9	257.7	270.1	11.4	1.7
32	n=2.00_1300C_11hr_3kgf_10X_32					FALSE	FALSE
33	n=2.00_1300C_11hr_3kgf_10X_33					FALSE	FALSE
34	n=2.00_1300C_11hr_3kgf_10X_34					FALSE	FALSE
35	n=2.00_1300C_11hr_3kgf_10X_35					FALSE	FALSE
1	n=2.00_1300C_11hr_3kgf_10X_1	67.4	67.0			12.1	FALSE
2	n=2.00_1300C_11hr_3kgf_10X_2	66.7	67.6	232.3	239.8	12.1	1.9
3	n=2.00_1300C_11hr_3kgf_10X_3					FALSE	FALSE
4	n=2.00_1300C_11hr_3kgf_10X_4	68.7	68.2			11.6	FALSE
5	n=2.00_1300C_11hr_3kgf_10X_5	68.1	70.0	263.1	309.0	11.4	1.5
6	n=2.00_1300C_11hr_3kgf_10X_6	70.1	67.8	300.0	229.4	11.5	1.7
7	n=2.00_1300C_11hr_3kgf_10X_7					FALSE	FALSE
8	n=2.00_1300C_11hr_3kgf_10X_8					FALSE	FALSE
9	n=2.00_1300C_11hr_3kgf_10X_9					FALSE	FALSE
10	n=2.00_1300C_11hr_3kgf_10X_10					FALSE	FALSE
11	n=2.00_1300C_11hr_3kgf_10X_11					FALSE	FALSE
12	n=2.00_1300C_11hr_3kgf_10X_12	68.4	69.2	333.2	223.0	11.5	1.5
13	n=2.00_1300C_11hr_3kgf_10X_13					FALSE	FALSE
14	n=2.00_1300C_11hr_3kgf_10X_14	68.1	67.2	369.0	275.5	11.9	1.2
15	n=2.00_1300C_11hr_3kgf_10X_15					FALSE	FALSE
16	n=2.00_1300C_11hr_3kgf_10X_16					FALSE	FALSE
17	n=2.00_1300C_11hr_3kgf_10X_17					FALSE	FALSE
18	n=2.00_1300C_11hr_3kgf_10X_18					FALSE	FALSE
19	n=2.00_1300C_11hr_3kgf_10X_19					FALSE	FALSE
20	n=2.00_1300C_11hr_3kgf_10X_20	68.6	69.6	234.3	275.6	11.4	1.8
21	n=2.00_1300C_11hr_3kgf_10X_21					FALSE	FALSE
22	n=2.00_1300C_11hr_3kgf_10X_22					FALSE	FALSE
23	n=2.00_1300C_11hr_3kgf_10X_23					FALSE	FALSE
24	n=2.00_1300C_11hr_3kgf_10X_24					FALSE	FALSE
25	n=2.00_1300C_11hr_3kgf_10X_25					FALSE	FALSE
26	n=2.00_1300C_11hr_3kgf_10X_26					FALSE	FALSE
27	n=2.00_1300C_11hr_3kgf_10X_27	69.9	72.9	275.3	305.0	10.7	1.5
28	n=2.00_1300C_11hr_3kgf_10X_28					FALSE	FALSE
29	n=2.00_1300C_11hr_3kgf_10X_29	68.1	68.9	295.1	221.3	11.6	1.7

Table B-1 Continued

Indent	file name	ah (μm)	av (μm)	2ch (μm)	2cv (μm)	H (GPa)	K (MPa $\sqrt{\text{m}}$)
30	n=2.00_1300C_11hr_3kgf_10X_30					FALSE	FALSE
31	n=2.00_1300C_11hr_3kgf_10X_31					FALSE	FALSE
32	n=2.00_1300C_11hr_3kgf_10X_32					FALSE	FALSE
1	n=1.00_1300C_10hrs_atm_3kgf_10X_01					FALSE	FALSE
2	n=1.00_1300C_10hrs_atm_3kgf_10X_02					FALSE	FALSE
3	n=1.00_1300C_10hrs_atm_3kgf_10X_03					FALSE	FALSE
4	n=1.00_1300C_10hrs_atm_3kgf_10X_04					FALSE	FALSE
5	n=1.00_1300C_10hrs_atm_3kgf_10X_05	66.0	66.5			12.4	FALSE
6	n=1.00_1300C_10hrs_atm_3kgf_10X_06	68.3	68.7			11.6	FALSE
7	n=1.00_1300C_10hrs_atm_3kgf_10X_07	64.7	67.1			12.6	FALSE
8	n=1.00_1300C_10hrs_atm_3kgf_10X_08					FALSE	FALSE
9	n=1.00_1300C_10hrs_atm_3kgf_10X_09	66.7	66.3			12.3	FALSE
10	n=1.00_1300C_10hrs_atm_3kgf_10X_10					FALSE	FALSE
11	n=1.00_1300C_10hrs_atm_3kgf_10X_11	66.2	67.8			12.2	FALSE
12	n=1.00_1300C_10hrs_atm_3kgf_10X_12					FALSE	FALSE
13	n=1.00_1300C_10hrs_atm_3kgf_10X_13					FALSE	FALSE
14	n=1.00_1300C_10hrs_atm_3kgf_10X_14	64.5	66.1	248.2	267.6	12.8	1.5
15	n=1.00_1300C_10hrs_atm_3kgf_10X_15	68.2	68.0	258.9	274.7	11.8	1.5
16	n=1.00_1300C_10hrs_atm_3kgf_10X_16	64.9	65.8	275.1	290.0	12.8	1.3
17	n=1.00_1300C_10hrs_atm_3kgf_10X_17					FALSE	FALSE
18	n=1.00_1300C_10hrs_atm_3kgf_10X_18					FALSE	FALSE
19	n=1.00_1300C_10hrs_atm_3kgf_10X_19	62.6	64.7	298.1	259.2	13.5	1.3
20	n=1.00_1300C_10hrs_atm_3kgf_10X_20	65.3	67.9	256.2	243.1	12.3	1.7
21	n=1.00_1300C_10hrs_atm_3kgf_10X_21	64.5	64.9	314.3	245.3	13.0	1.4
22	n=1.00_1300C_10hrs_atm_3kgf_10X_22	64.7	65.1			12.9	FALSE
23	n=1.00_1300C_10hrs_atm_3kgf_10X_23	65.2	67.8	269.0	270.6	12.3	1.5
24	n=1.00_1300C_10hrs_atm_3kgf_10X_24					FALSE	FALSE
25	n=1.00_1300C_10hrs_atm_3kgf_10X_25					FALSE	FALSE
26	n=1.00_1300C_10hrs_atm_3kgf_10X_26	66.3	68.2	353.4	334.6	12.1	1.0
27	n=1.00_1300C_10hrs_atm_3kgf_10X_27	64.2	63.1			13.5	FALSE
28	n=1.00_1300C_10hrs_atm_3kgf_10X_28					FALSE	FALSE
29	n=1.00_1300C_10hrs_atm_3kgf_10X_29					FALSE	FALSE
30	n=1.00_1300C_10hrs_atm_3kgf_10X_30	65.1	65.7	257.8	243.1	12.8	1.6
1	n=1.00_1300C_10hrs_vac_3kgf_10X_01					FALSE	FALSE
2	n=1.00_1300C_10hrs_vac_3kgf_10X_02					FALSE	FALSE
3	n=1.00_1300C_10hrs_vac_3kgf_10X_03	63.6	65.6			13.1	FALSE
4	n=1.00_1300C_10hrs_vac_3kgf_10X_04					FALSE	FALSE
5	n=1.00_1300C_10hrs_vac_3kgf_10X_05					FALSE	FALSE
6	n=1.00_1300C_10hrs_vac_3kgf_10X_06	62.8	63.8			13.6	FALSE
7	n=1.00_1300C_10hrs_vac_3kgf_10X_07	64.5	66.3			12.8	FALSE
8	n=1.00_1300C_10hrs_vac_3kgf_10X_08	65.4	66.4			12.6	FALSE
9	n=1.00_1300C_10hrs_vac_3kgf_10X_09					FALSE	FALSE

Table B-1 Continued

Indent	file name	ah (μm)	av (μm)	2ch (μm)	2cv (μm)	H (GPa)	K (MPa $\sqrt{\text{m}}$)
10	n=1.00_1300C_10hrs_vac_3kgf_10X_10					FALSE	FALSE
11	n=1.00_1300C_10hrs_vac_3kgf_10X_11					FALSE	FALSE
12	n=1.00_1300C_10hrs_vac_3kgf_10X_12					FALSE	FALSE
13	n=1.00_1300C_10hrs_vac_3kgf_10X_13	66.2	67.3	290.7	288.9	12.3	1.3
14	n=1.00_1300C_10hrs_vac_3kgf_10X_14					FALSE	FALSE
15	n=1.00_1300C_10hrs_vac_3kgf_10X_15	64.5	64.9			13.0	FALSE
16	n=1.00_1300C_10hrs_vac_3kgf_10X_16					FALSE	FALSE
17	n=1.00_1300C_10hrs_vac_3kgf_10X_17					FALSE	FALSE
18	n=1.00_1300C_10hrs_vac_3kgf_10X_18	69.1	67.3	340.4	278.0	11.7	1.2
19	n=1.00_1300C_10hrs_vac_3kgf_10X_19					FALSE	FALSE
20	n=1.00_1300C_10hrs_vac_3kgf_10X_20	65.6	67.2	297.5	297.3	12.4	1.3
21	n=1.00_1300C_10hrs_vac_3kgf_10X_21					FALSE	FALSE
22	n=1.00_1300C_10hrs_vac_3kgf_10X_22					FALSE	FALSE
23	n=1.00_1300C_10hrs_vac_3kgf_10X_23					FALSE	FALSE
24	n=1.00_1300C_10hrs_vac_3kgf_10X_24					FALSE	FALSE
25	n=1.00_1300C_10hrs_vac_3kgf_10X_25	64.4	65.1			13.0	FALSE
26	n=1.00_1300C_10hrs_vac_3kgf_10X_26	64.3	66.0	268.9	280.9	12.8	1.4
27	n=1.00_1300C_10hrs_vac_3kgf_10X_27					FALSE	FALSE
28	n=1.00_1300C_10hrs_vac_3kgf_10X_28					FALSE	FALSE
29	n=1.00_1300C_10hrs_vac_3kgf_10X_29	65.0	65.1			12.9	FALSE
30	n=1.00_1300C_10hrs_vac_3kgf_10X_30					FALSE	FALSE
1	n=1.00_1300C_20hrs_atm_3kgf_10X_01	66.0	67.1	337.9	372.4	12.3	1.0
2	n=1.00_1300C_20hrs_atm_3kgf_10X_02					FALSE	FALSE
3	n=1.00_1300C_20hrs_atm_3kgf_10X_03					FALSE	FALSE
4	n=1.00_1300C_20hrs_atm_3kgf_10X_04	65.8	62.9	289.9	257.7	13.2	1.4
5	n=1.00_1300C_20hrs_atm_3kgf_10X_05					FALSE	FALSE
6	n=1.00_1300C_20hrs_atm_3kgf_10X_06					FALSE	FALSE
7	n=1.00_1300C_20hrs_atm_3kgf_10X_07					FALSE	FALSE
8	n=1.00_1300C_20hrs_atm_3kgf_10X_08					FALSE	FALSE
9	n=1.00_1300C_20hrs_atm_3kgf_10X_09					FALSE	FALSE
10	n=1.00_1300C_20hrs_atm_3kgf_10X_10					FALSE	FALSE
11	n=1.00_1300C_20hrs_atm_3kgf_10X_11					FALSE	FALSE
12	n=1.00_1300C_20hrs_atm_3kgf_10X_12					FALSE	FALSE
13	n=1.00_1300C_20hrs_atm_3kgf_10X_13					FALSE	FALSE
14	n=1.00_1300C_20hrs_atm_3kgf_10X_14					FALSE	FALSE
15	n=1.00_1300C_20hrs_atm_3kgf_10X_15	64.7	65.1	297.9	300.3	12.9	1.2
16	n=1.00_1300C_20hrs_atm_3kgf_10X_16					FALSE	FALSE
17	n=1.00_1300C_20hrs_atm_3kgf_10X_17					FALSE	FALSE
18	n=1.00_1300C_20hrs_atm_3kgf_10X_18	64.7	65.1	270.1	360.6	13.0	1.1
19	n=1.00_1300C_20hrs_atm_3kgf_10X_19					FALSE	FALSE
20	n=1.00_1300C_20hrs_atm_3kgf_10X_20					FALSE	FALSE
21	n=1.00_1300C_20hrs_atm_3kgf_10X_21	67.7	64.4	283.1	296.6	12.5	1.3
22	n=1.00_1300C_20hrs_atm_3kgf_10X_22					FALSE	FALSE

Table B-1 Continued

Indent	file name	ah (μm)	av (μm)	2ch (μm)	2cv (μm)	H (GPa)	K (MPa $\sqrt{\text{m}}$)
23	n=1.00_1300C_20hrs_atm_3kgf_10X_23					FALSE	FALSE
24	n=1.00_1300C_20hrs_atm_3kgf_10X_24					FALSE	FALSE
25	n=1.00_1300C_20hrs_atm_3kgf_10X_25					FALSE	FALSE
26	n=1.00_1300C_20hrs_atm_3kgf_10X_26					FALSE	FALSE
27	n=1.00_1300C_20hrs_atm_3kgf_10X_27					FALSE	FALSE
28	n=1.00_1300C_20hrs_atm_3kgf_10X_28					FALSE	FALSE
29	n=1.00_1300C_20hrs_atm_3kgf_10X_29					FALSE	FALSE
30	n=1.00_1300C_20hrs_atm_3kgf_10X_30					FALSE	FALSE
1	n=1.00_1300C_20hrs_vac_3kgf_10X_01					FALSE	FALSE
2	n=1.00_1300C_20hrs_vac_3kgf_10X_02					FALSE	FALSE
3	n=1.00_1300C_20hrs_vac_3kgf_10X_03					FALSE	FALSE
4	n=1.00_1300C_20hrs_vac_3kgf_10X_04	65.4	65.4	280.5	308.2	12.8	1.3
5	n=1.00_1300C_20hrs_vac_3kgf_10X_05					FALSE	FALSE
6	n=1.00_1300C_20hrs_vac_3kgf_10X_06					FALSE	FALSE
7	n=1.00_1300C_20hrs_vac_3kgf_10X_07					FALSE	FALSE
8	n=1.00_1300C_20hrs_vac_3kgf_10X_08					FALSE	FALSE
9	n=1.00_1300C_20hrs_vac_3kgf_10X_09					FALSE	FALSE
10	n=1.00_1300C_20hrs_vac_3kgf_10X_10					FALSE	FALSE
11	n=1.00_1300C_20hrs_vac_3kgf_10X_11					FALSE	FALSE
12	n=1.00_1300C_20hrs_vac_3kgf_10X_12					FALSE	FALSE
13	n=1.00_1300C_20hrs_vac_3kgf_10X_13	63.5	65.2	291.8	281.4	13.2	1.3
14	n=1.00_1300C_20hrs_vac_3kgf_10X_14					FALSE	FALSE
15	n=1.00_1300C_20hrs_vac_3kgf_10X_15					FALSE	FALSE
16	n=1.00_1300C_20hrs_vac_3kgf_10X_16					FALSE	FALSE
17	n=1.00_1300C_20hrs_vac_3kgf_10X_17	69.8	69.1	283.7	258.5	11.3	1.5
18	n=1.00_1300C_20hrs_vac_3kgf_10X_18					FALSE	FALSE
19	n=1.00_1300C_20hrs_vac_3kgf_10X_19					FALSE	FALSE
20	n=1.00_1300C_20hrs_vac_3kgf_10X_20					FALSE	FALSE
21	n=1.00_1300C_20hrs_vac_3kgf_10X_21					FALSE	FALSE
22	n=1.00_1300C_20hrs_vac_3kgf_10X_22					FALSE	FALSE
23	n=1.00_1300C_20hrs_vac_3kgf_10X_23					FALSE	FALSE
24	n=1.00_1300C_20hrs_vac_3kgf_10X_24					FALSE	FALSE
25	n=1.00_1300C_20hrs_vac_3kgf_10X_25					FALSE	FALSE
26	n=1.00_1300C_20hrs_vac_3kgf_10X_26					FALSE	FALSE
27	n=1.00_1300C_20hrs_vac_3kgf_10X_27					FALSE	FALSE
28	n=1.00_1300C_20hrs_vac_3kgf_10X_28					FALSE	FALSE
29	n=1.00_1300C_20hrs_vac_3kgf_10X_29					FALSE	FALSE
30	n=1.00_1300C_20hrs_vac_3kgf_10X_30					FALSE	FALSE
1	n=2.00_1300C_20hr_atm_3kgf_10X_1	70.0	68.3			11.4	FALSE
2	n=2.00_1300C_20hr_atm_3kgf_10X_2					FALSE	FALSE
3	n=2.00_1300C_20hr_atm_3kgf_10X_3					FALSE	FALSE
4	n=2.00_1300C_20hr_atm_3kgf_10X_4	68.3	68.7	614.2	262.3	11.6	0.8

Table B-1 Continued

Indent	file name	ah (μm)	av (μm)	2ch (μm)	2cv (μm)	H (GPa)	K (MPa $\sqrt{\text{m}}$)
5	n=2.00_1300C_20hr_atm_3kgf_10X_5					FALSE	FALSE
6	n=2.00_1300C_20hr_atm_3kgf_10X_6	72.5	68.2			11.0	FALSE
7	n=2.00_1300C_20hr_atm_3kgf_10X_7	69.0	70.7	252.8	244.4	11.2	1.9
8	n=2.00_1300C_20hr_atm_3kgf_10X_8	71.5	68.2			11.2	FALSE
9	n=2.00_1300C_20hr_atm_3kgf_10X_9	70.1	70.9			11.0	FALSE
10	n=2.00_1300C_20hr_atm_3kgf_10X_10	69.0	66.1			12.0	FALSE
11	n=2.00_1300C_20hr_atm_3kgf_10X_11					FALSE	FALSE
12	n=2.00_1300C_20hr_atm_3kgf_10X_12	68.9	69.3	243.8	202.2	11.4	2.2
13	n=2.00_1300C_20hr_atm_3kgf_10X_13	68.2	67.0	478.4	338.4	11.9	0.9
14	n=2.00_1300C_20hr_atm_3kgf_10X_14	69.4	69.4			11.3	FALSE
15	n=2.00_1300C_20hr_atm_3kgf_10X_15	67.2	71.8	296.5	221.0	11.3	1.7
16	n=2.00_1300C_20hr_atm_3kgf_10X_16	73.0	68.5			10.9	FALSE
17	n=2.00_1300C_20hr_atm_3kgf_10X_17	72.5	71.4	276.2	213.3	10.5	2.0
18	n=2.00_1300C_20hr_atm_3kgf_10X_18					FALSE	FALSE
19	n=2.00_1300C_20hr_atm_3kgf_10X_19	68.0	73.4			10.9	FALSE
20	n=2.00_1300C_20hr_atm_3kgf_10X_20	71.7	71.9	222.5	481.4	10.6	1.1
21	n=2.00_1300C_20hr_atm_3kgf_10X_21	70.4	67.0	221.9	192.5	11.6	2.4
22	n=2.00_1300C_20hr_atm_3kgf_10X_22	73.4	71.1	432.8	219.8	10.5	1.3
23	n=2.00_1300C_20hr_atm_3kgf_10X_23	71.0	72.1			10.7	FALSE
24	n=2.00_1300C_20hr_atm_3kgf_10X_24					FALSE	FALSE
25	n=2.00_1300C_20hr_atm_3kgf_10X_25	68.6	68.8			11.6	FALSE
26	n=2.00_1300C_20hr_atm_3kgf_10X_26	68.8	67.5	466.7	470.6	11.8	0.7
27	n=2.00_1300C_20hr_atm_3kgf_10X_27	70.5	70.8	433.9	226.6	10.9	1.2
28	n=2.00_1300C_20hr_atm_3kgf_10X_28	69.3	73.5			10.7	FALSE
29	n=2.00_1300C_20hr_atm_3kgf_10X_29	72.7	69.7	555.6	241.8	10.8	0.9
1	n=2.00_1300C_20hr_vac_3kgf_10X_01	68.0	71.8	278.4	334.5	11.2	1.4
2	n=2.00_1300C_20hr_vac_3kgf_10X_02					FALSE	FALSE
3	n=2.00_1300C_20hr_vac_3kgf_10X_03					FALSE	FALSE
4	n=2.00_1300C_20hr_vac_3kgf_10X_04	72.3	69.8	297.2	334.5	10.8	1.3
5	n=2.00_1300C_20hr_vac_3kgf_10X_05	69.3	65.4	247.1	223.4	12.0	1.9
6	n=2.00_1300C_20hr_vac_3kgf_10X_06					FALSE	FALSE
7	n=2.00_1300C_20hr_vac_3kgf_10X_07					FALSE	FALSE
8	n=2.00_1300C_20hr_vac_3kgf_10X_08					FALSE	FALSE
9	n=2.00_1300C_20hr_vac_3kgf_10X_09					FALSE	FALSE
10	n=2.00_1300C_20hr_vac_3kgf_10X_10					FALSE	FALSE
11	n=2.00_1300C_20hr_vac_3kgf_10X_11					FALSE	FALSE
12	n=2.00_1300C_20hr_vac_3kgf_10X_12					FALSE	FALSE
13	n=2.00_1300C_20hr_vac_3kgf_10X_13	69.0	62.7	236.3	254.1	12.6	1.8
14	n=2.00_1300C_20hr_vac_3kgf_10X_14	70.9	67.5	276.1	244.0	11.4	1.7
15	n=2.00_1300C_20hr_vac_3kgf_10X_15	69.4	68.9	314.1	239.2	11.4	1.6
16	n=2.00_1300C_20hr_vac_3kgf_10X_16					FALSE	FALSE
17	n=2.00_1300C_20hr_vac_3kgf_10X_17	69.6	65.7	269.6	269.5	11.9	1.6
18	n=2.00_1300C_20hr_vac_3kgf_10X_18					FALSE	FALSE

Table B-1 Continued

Indent	file name	ah (μm)	av (μm)	2ch (μm)	2cv (μm)	H (GPa)	K (MPa $\sqrt{\text{m}}$)
19	n=2.00_1300C_20hr_vac_3kgf_10X_19					FALSE	FALSE
20	n=2.00_1300C_20hr_vac_3kgf_10X_20					FALSE	FALSE
21	n=2.00_1300C_20hr_vac_3kgf_10X_21					FALSE	FALSE
22	n=2.00_1300C_20hr_vac_3kgf_10X_22					FALSE	FALSE
23	n=2.00_1300C_20hr_vac_3kgf_10X_23					FALSE	FALSE
24	n=2.00_1300C_20hr_vac_3kgf_10X_24					FALSE	FALSE
25	n=2.00_1300C_20hr_vac_3kgf_10X_25					FALSE	FALSE
26	n=2.00_1300C_20hr_vac_3kgf_10X_26					FALSE	FALSE
27	n=2.00_1300C_20hr_vac_3kgf_10X_27					FALSE	FALSE
28	n=2.00_1300C_20hr_vac_3kgf_10X_28					FALSE	FALSE
29	n=2.00_1300C_20hr_vac_3kgf_10X_29					FALSE	FALSE
30	n=2.00_1300C_20hr_vac_3kgf_10X_30					FALSE	FALSE
1	n=1.00_1300C_HIP_10hrs_3kgf_10X_01	65.7	66.0	279.9	301.3	12.6	1.3
2	n=1.00_1300C_HIP_10hrs_3kgf_10X_02					FALSE	FALSE
3	n=1.00_1300C_HIP_10hrs_3kgf_10X_03					FALSE	FALSE
4	n=1.00_1300C_HIP_10hrs_3kgf_10X_04	64.0	66.2	235.3	298.4	12.9	1.5
5	n=1.00_1300C_HIP_10hrs_3kgf_10X_05	68.1	65.8			12.2	FALSE
6	n=1.00_1300C_HIP_10hrs_3kgf_10X_06	66.3	65.7	245.9	255.7	12.5	1.6
7	n=1.00_1300C_HIP_10hrs_3kgf_10X_07	67.2	66.4			12.2	FALSE
8	n=1.00_1300C_HIP_10hrs_3kgf_10X_08					FALSE	FALSE
9	n=1.00_1300C_HIP_10hrs_3kgf_10X_09					FALSE	FALSE
10	n=1.00_1300C_HIP_10hrs_3kgf_10X_10	64.4	61.7	289.2	309.5	13.7	1.2
11	n=1.00_1300C_HIP_10hrs_3kgf_10X_11					FALSE	FALSE
12	n=1.00_1300C_HIP_10hrs_3kgf_10X_12					FALSE	FALSE
13	n=1.00_1300C_HIP_10hrs_3kgf_10X_13					FALSE	FALSE
14	n=1.00_1300C_HIP_10hrs_3kgf_10X_14					FALSE	FALSE
15	n=1.00_1300C_HIP_10hrs_3kgf_10X_15					FALSE	FALSE
16	n=1.00_1300C_HIP_10hrs_3kgf_10X_16					FALSE	FALSE
17	n=1.00_1300C_HIP_10hrs_3kgf_10X_17	63.9	64.1	241.6	300.0	13.3	1.4
18	n=1.00_1300C_HIP_10hrs_3kgf_10X_18					FALSE	FALSE
19	n=1.00_1300C_HIP_10hrs_3kgf_10X_19	63.0	65.2	327.3	291.1	13.3	1.2
20	n=1.00_1300C_HIP_10hrs_3kgf_10X_20					FALSE	FALSE
21	n=1.00_1300C_HIP_10hrs_3kgf_10X_21					FALSE	FALSE
22	n=1.00_1300C_HIP_10hrs_3kgf_10X_22					FALSE	FALSE
23	n=1.00_1300C_HIP_10hrs_3kgf_10X_23					FALSE	FALSE
24	n=1.00_1300C_HIP_10hrs_3kgf_10X_24					FALSE	FALSE
25	n=1.00_1300C_HIP_10hrs_3kgf_10X_25					FALSE	FALSE
26	n=1.00_1300C_HIP_10hrs_3kgf_10X_26					FALSE	FALSE
27	n=1.00_1300C_HIP_10hrs_3kgf_10X_27					FALSE	FALSE
28	n=1.00_1300C_HIP_10hrs_3kgf_10X_28					FALSE	FALSE
29	n=1.00_1300C_HIP_10hrs_3kgf_10X_29					FALSE	FALSE
30	n=1.00_1300C_HIP_10hrs_3kgf_10X_30	64.9	65.1			12.9	FALSE

Table B-1 Continued

Indent	file name	ah (μm)	av (μm)	2ch (μm)	2cv (μm)	H (GPa)	K (MPa $\sqrt{\text{m}}$)
1	n=2.00_1300C_HIP_10hrs_3kgf_10X_01					FALSE	FALSE
2	n=2.00_1300C_HIP_10hrs_3kgf_10X_02					FALSE	FALSE
3	n=2.00_1300C_HIP_10hrs_3kgf_10X_03	68.8	68.7	254.8	255.2	11.5	1.8
4	n=2.00_1300C_HIP_10hrs_3kgf_10X_04					FALSE	FALSE
5	n=2.00_1300C_HIP_10hrs_3kgf_10X_05					FALSE	FALSE
6	n=2.00_1300C_HIP_10hrs_3kgf_10X_06					FALSE	FALSE
7	n=2.00_1300C_HIP_10hrs_3kgf_10X_07	69.1	69.2	310.0	295.2	11.4	1.4
8	n=2.00_1300C_HIP_10hrs_3kgf_10X_08					FALSE	FALSE
9	n=2.00_1300C_HIP_10hrs_3kgf_10X_09	67.2	67.5	230.1	228.4	12.0	2.0
10	n=2.00_1300C_HIP_10hrs_3kgf_10X_10	69.7	70.8	272.3	217.4	11.1	1.9
11	n=2.00_1300C_HIP_10hrs_3kgf_10X_11					FALSE	FALSE
12	n=2.00_1300C_HIP_10hrs_3kgf_10X_12					FALSE	FALSE
13	n=2.00_1300C_HIP_10hrs_3kgf_10X_13					FALSE	FALSE
14	n=2.00_1300C_HIP_10hrs_3kgf_10X_14	71.9	70.1	309.6	262.3	10.8	1.5
15	n=2.00_1300C_HIP_10hrs_3kgf_10X_15					FALSE	FALSE
16	n=2.00_1300C_HIP_10hrs_3kgf_10X_16	69.1	69.7	325.4	254.2	11.3	1.5
17	n=2.00_1300C_HIP_10hrs_3kgf_10X_17	70.2	67.5	272.9	260.2	11.5	1.7
18	n=2.00_1300C_HIP_10hrs_3kgf_10X_18					FALSE	FALSE
19	n=2.00_1300C_HIP_10hrs_3kgf_10X_19					FALSE	FALSE
20	n=2.00_1300C_HIP_10hrs_3kgf_10X_20					FALSE	FALSE
21	n=2.00_1300C_HIP_10hrs_3kgf_10X_21					FALSE	FALSE
22	n=2.00_1300C_HIP_10hrs_3kgf_10X_22					FALSE	FALSE
23	n=2.00_1300C_HIP_10hrs_3kgf_10X_23					FALSE	FALSE
24	n=2.00_1300C_HIP_10hrs_3kgf_10X_24					FALSE	FALSE
25	n=2.00_1300C_HIP_10hrs_3kgf_10X_25					FALSE	FALSE
26	n=2.00_1300C_HIP_10hrs_3kgf_10X_26					FALSE	FALSE
27	n=2.00_1300C_HIP_10hrs_3kgf_10X_27					FALSE	FALSE
28	n=2.00_1300C_HIP_10hrs_3kgf_10X_28					FALSE	FALSE
29	n=2.00_1300C_HIP_10hrs_3kgf_10X_29					FALSE	FALSE
30	n=2.00_1300C_HIP_10hrs_3kgf_10X_30	67.8	67.6	316.1	200.2	11.9	1.7
1	n=2.00_1300C_05hr_atm_10X_01	74.8	77.2	294.9	265.7	9.4	1.7
2	n=2.00_1300C_05hr_atm_10X_02					FALSE	FALSE
3	n=2.00_1300C_05hr_atm_10X_03	73.8	73.3	289.1	246.5	10.1	1.8
4	n=2.00_1300C_05hr_atm_10X_04					FALSE	FALSE
5	n=2.00_1300C_05hr_atm_10X_05	69.9	70.3	279.6	265.2	11.1	1.6
6	n=2.00_1300C_05hr_atm_10X_06					FALSE	FALSE
7	n=2.00_1300C_05hr_atm_10X_07	68.3	68.3			11.7	FALSE
8	n=2.00_1300C_05hr_atm_10X_08					FALSE	FALSE
9	n=2.00_1300C_05hr_atm_10X_09	70.1	69.7			11.2	FALSE
10	n=2.00_1300C_05hr_atm_10X_10					FALSE	FALSE
11	n=2.00_1300C_05hr_atm_10X_11	68.4	67.8			11.8	FALSE
12	n=2.00_1300C_05hr_atm_10X_12	68.6	66.7			11.9	FALSE
13	n=2.00_1300C_05hr_atm_10X_13					FALSE	FALSE

Table B-1 Continued

Indent	file name	ah (μm)	av (μm)	2ch (μm)	2cv (μm)	H (GPa)	K (MPa $\sqrt{\text{m}}$)
14	n=2.00_1300C_05hr_atm_10X_14					FALSE	FALSE
15	n=2.00_1300C_05hr_atm_10X_15	69.2	69.8	262.2	281.3	11.3	1.6
16	n=2.00_1300C_05hr_atm_10X_16	62.9	66.7	115.5	226.8	13.0	3.0
17	n=2.00_1300C_05hr_atm_10X_17	69.3	67.3	263.5	286.2	11.7	1.6
18	n=2.00_1300C_05hr_atm_10X_18					FALSE	FALSE
19	n=2.00_1300C_05hr_atm_10X_19					FALSE	FALSE
20	n=2.00_1300C_05hr_atm_10X_20					FALSE	FALSE
21	n=2.00_1300C_05hr_atm_10X_21					FALSE	FALSE
22	n=2.00_1300C_05hr_atm_10X_22					FALSE	FALSE
23	n=2.00_1300C_05hr_atm_10X_23					FALSE	FALSE
24	n=2.00_1300C_05hr_atm_10X_24	69.7	67.5	251.7	247.0	11.6	1.8
25	n=2.00_1300C_05hr_atm_10X_25					FALSE	FALSE
26	n=2.00_1300C_05hr_atm_10X_26					FALSE	FALSE
27	n=2.00_1300C_05hr_atm_10X_27					FALSE	FALSE
28	n=2.00_1300C_05hr_atm_10X_28					FALSE	FALSE
29	n=2.00_1300C_05hr_atm_10X_29					FALSE	FALSE
30	n=2.00_1300C_05hr_atm_10X_30					FALSE	FALSE
31	n=2.00_1300C_05hr_atm_10X_31	72.2	67.5	214.0	238.3	11.2	2.1
10	n=2.00_1300C_05hr_vac_10X_10					FALSE	FALSE
11	n=2.00_1300C_05hr_vac_10X_11					FALSE	FALSE
12	n=2.00_1300C_05hr_vac_10X_12	70.9	70.8	272.7	261.7	10.9	1.7
13	n=2.00_1300C_05hr_vac_10X_13	72.6	70.3			10.7	FALSE
14	n=2.00_1300C_05hr_vac_10X_14					FALSE	FALSE
15	n=2.00_1300C_05hr_vac_10X_15					FALSE	FALSE
16	n=2.00_1300C_05hr_vac_10X_16	70.8	71.2			10.8	FALSE
17	n=2.00_1300C_05hr_vac_10X_17					FALSE	FALSE
18	n=2.00_1300C_05hr_vac_10X_18	69.1	67.3			11.7	FALSE
19	n=2.00_1300C_05hr_vac_10X_19	69.3	68.9	295.7	255.8	11.4	1.6
19.1	n=2.00_1300C_05hr_vac_10X_19.1					FALSE	FALSE
19.2	n=2.00_1300C_05hr_vac_10X_19.2	69.3	69.6			11.3	FALSE
19.3	n=2.00_1300C_05hr_vac_10X_19.3					FALSE	FALSE
20	n=2.00_1300C_05hr_vac_10X_20	67.3	68.9	302.5	252.9	11.8	1.5
21	n=2.00_1300C_05hr_vac_10X_21					FALSE	FALSE
22	n=2.00_1300C_05hr_vac_10X_22	69.6	68.9	324.0	294.9	11.4	1.3
23	n=2.00_1300C_05hr_vac_10X_23	70.5	69.3			11.2	FALSE
24	n=2.00_1300C_05hr_vac_10X_24					FALSE	FALSE
25	n=2.00_1300C_05hr_vac_10X_25					FALSE	FALSE
26	n=2.00_1300C_05hr_vac_10X_26	67.5	66.8			12.1	FALSE
27	n=2.00_1300C_05hr_vac_10X_27	68.5	69.1	308.5	282.2	11.5	1.4
28	n=2.00_1300C_05hr_vac_10X_28	68.7	68.5	303.1	227.1	11.6	1.7
29	n=2.00_1300C_05hr_vac_10X_29	69.7	70.3	284.7	247.2	11.1	1.7
30	n=2.00_1300C_05hr_vac_10X_30					FALSE	FALSE
31	n=2.00_1300C_05hr_vac_10X_31					FALSE	FALSE

Table B-1 Continued

Indent	file name	ah (μm)	av (μm)	2ch (μm)	2cv (μm)	H (GPa)	K (MPa $\sqrt{\text{m}}$)
32	n=2.00_1300C_05hr_vac_10X_32					FALSE	FALSE
33	n=2.00_1300C_05hr_vac_10X_33					FALSE	FALSE
34	n=2.00_1300C_05hr_vac_10X_34					FALSE	FALSE
35	n=2.00_1300C_05hr_vac_10X_35	70.8	69.5	267.9	252.6	11.1	1.7
36	n=2.00_1300C_05hr_vac_10X_36	71.1	69.7			11.0	FALSE
37	n=2.00_1300C_05hr_vac_10X_37					FALSE	FALSE
38	n=2.00_1300C_05hr_vac_10X_38					FALSE	FALSE
39	n=2.00_1300C_05hr_vac_10X_39					FALSE	FALSE
10	n=2.00_1300C_15hr_vac_10X_10	66.1	67.1			12.3	FALSE
11	n=2.00_1300C_15hr_vac_10X_11	69.1	68.0	263.3	281.2	11.6	1.6
12	n=2.00_1300C_15hr_vac_10X_12					FALSE	FALSE
13	n=2.00_1300C_15hr_vac_10X_13					FALSE	FALSE
14	n=2.00_1300C_15hr_vac_10X_14					FALSE	FALSE
15	n=2.00_1300C_15hr_vac_10X_15	70.3	68.8	239.6	274.2	11.3	1.8
16	n=2.00_1300C_15hr_vac_10X_16					FALSE	FALSE
17	n=2.00_1300C_15hr_vac_10X_17					FALSE	FALSE
18	n=2.00_1300C_15hr_vac_10X_18	68.6	67.9			11.7	FALSE
19	n=2.00_1300C_15hr_vac_10X_19	67.2	69.0			11.8	FALSE
20	n=2.00_1300C_15hr_vac_10X_20					FALSE	FALSE
21	n=2.00_1300C_15hr_vac_10X_21					FALSE	FALSE
22	n=2.00_1300C_15hr_vac_10X_22	69.4	68.5	259.6	263.9	11.5	1.7
23	n=2.00_1300C_15hr_vac_10X_23					FALSE	FALSE
24	n=2.00_1300C_15hr_vac_10X_24					FALSE	FALSE
25	n=2.00_1300C_15hr_vac_10X_25	72.3	71.4	255.2	280.0	10.6	1.7
26	n=2.00_1300C_15hr_vac_10X_26					FALSE	FALSE
27	n=2.00_1300C_15hr_vac_10X_27					FALSE	FALSE
28	n=2.00_1300C_15hr_vac_10X_28	68.0	67.4			11.9	FALSE
29	n=2.00_1300C_15hr_vac_10X_29	67.8	66.6	263.7	231.3	12.1	1.8
30	n=2.00_1300C_15hr_vac_10X_30					FALSE	FALSE
31	n=2.00_1300C_15hr_vac_10X_31					FALSE	FALSE
32	n=2.00_1300C_15hr_vac_10X_32	68.0	70.7	220.5	233.9	11.4	2.1
33	n=2.00_1300C_15hr_vac_10X_33	68.2	67.5	270.1	221.1	11.8	1.8
34	n=2.00_1300C_15hr_vac_10X_34					FALSE	FALSE
35	n=2.00_1300C_15hr_vac_10X_35					FALSE	FALSE
36	n=2.00_1300C_15hr_vac_10X_36	68.5	69.2			11.5	FALSE
37	n=2.00_1300C_15hr_vac_10X_37	69.4	70.3			11.2	FALSE
38	n=2.00_1300C_15hr_vac_10X_38					FALSE	FALSE
39	n=2.00_1300C_15hr_vac_10X_39					FALSE	FALSE
10	n=2.00_1300C_15hr_air_10X_10					FALSE	FALSE
11	n=2.00_1300C_15hr_air_10X_11					FALSE	FALSE
12	n=2.00_1300C_15hr_air_10X_12					FALSE	FALSE
13	n=2.00_1300C_15hr_air_10X_13					FALSE	FALSE

Table B-1 Continued

Indent	file name	ah (μm)	av (μm)	2ch (μm)	2cv (μm)	H (GPa)	K (MPa $\sqrt{\text{m}}$)
14	n=2.00_1300C_15hr_air_10X_14					FALSE	FALSE
15	n=2.00_1300C_15hr_air_10X_15					FALSE	FALSE
16	n=2.00_1300C_15hr_air_10X_16					FALSE	FALSE
17	n=2.00_1300C_15hr_air_10X_17					FALSE	FALSE
18	n=2.00_1300C_15hr_air_10X_18					FALSE	FALSE
19	n=2.00_1300C_15hr_air_10X_19					FALSE	FALSE
20	n=2.00_1300C_15hr_air_10X_20					FALSE	FALSE
21	n=2.00_1300C_15hr_air_10X_21					FALSE	FALSE
22	n=2.00_1300C_15hr_air_10X_22					FALSE	FALSE
23	n=2.00_1300C_15hr_air_10X_23					FALSE	FALSE
24	n=2.00_1300C_15hr_air_10X_24					FALSE	FALSE
25	n=2.00_1300C_15hr_air_10X_25					FALSE	FALSE
26	n=2.00_1300C_15hr_air_10X_26	69.0	69.5			11.4	FALSE
27	n=2.00_1300C_15hr_air_10X_27					FALSE	FALSE
28	n=2.00_1300C_15hr_air_10X_28					FALSE	FALSE
29	n=2.00_1300C_15hr_air_10X_29					FALSE	FALSE
30	n=2.00_1300C_15hr_air_10X_30					FALSE	FALSE
31	n=2.00_1300C_15hr_air_10X_31					FALSE	FALSE
32	n=2.00_1300C_15hr_air_10X_32					FALSE	FALSE
33	n=2.00_1300C_15hr_air_10X_33					FALSE	FALSE
34	n=2.00_1300C_15hr_air_10X_34	70.8	68.8	238.6	245.5	11.2	1.9
35	n=2.00_1300C_15hr_air_10X_35	70.5	67.4	324.0	320.4	11.5	1.2
36	n=2.00_1300C_15hr_air_10X_36					FALSE	FALSE
37	n=2.00_1300C_15hr_air_10X_37					FALSE	FALSE
38	n=2.00_1300C_15hr_air_10X_38					FALSE	FALSE
39	n=2.00_1300C_15hr_air_10X_39					FALSE	FALSE
40	n=2.00_1300C_15hr_air_10X_40					FALSE	FALSE
41	n=2.00_1300C_15hr_air_10X_41					FALSE	FALSE
42	n=2.00_1300C_15hr_air_10X_42					FALSE	FALSE
43	n=2.00_1300C_15hr_air_10X_43	69.5	70.1	327.5	330.5	11.2	1.2
44	n=2.00_1300C_15hr_air_10X_44					FALSE	FALSE
45	n=2.00_1300C_15hr_air_10X_45					FALSE	FALSE
46	n=2.00_1300C_15hr_air_10X_46					FALSE	FALSE
47	n=2.00_1300C_15hr_air_10X_47					FALSE	FALSE
48	n=2.00_1300C_15hr_air_10X_48	70.5	70.5	351.4	392.0	11.0	1.0
49	n=2.00_1300C_15hr_air_10X_49					FALSE	FALSE

B.2 Dissolution of Al₂O₃

Similar to the data presented for the precipitation study, the data used to calculate the toughness of material used in the dissolution study discussed in chapter 5 is shown in. The length of the horizontal and vertical indent diagonal, horizontal and vertical crack, applied load, and calculated fracture toughness are also shown. The hardness values used to calculate indentation fracture toughness were made using a load of 1 kgf and are shown in Table B-2.

Table B-2. Hardness values determined using a load of 1 kgf are shown for each hot pressing routine investigated. These values were used to calculate the indentation toughness for an applied load of 3 kgf.

Hot Press Temperature (°C)	Hot Press Time (hours)	HV (GPa)
1600	5hr	11.0
1600	10hr	11.6
1600	20hr	12.0
1600	30hr	11.1
1650	10hr	11.2
1700	10hr	11.1

Table B-3. All measurements of indents used to calculate indentation fracture toughness during the dissolution study are shown.

Table B-3 Continued

Indent	file name	ah (µm)	av (µm)	2ch (µm)	2cv (µm)	H (GPa)	K (MPa√m)
1	n=2.00_alpha_1600C_5hr_3kgf_10X_01	72.1	69.8			10.8	FALSE
2	n=2.00_alpha_1600C_5hr_3kgf_10X_02	77.6	69.9			10.0	FALSE
3	n=2.00_alpha_1600C_5hr_3kgf_10X_03					FALSE	FALSE
4	n=2.00_alpha_1600C_5hr_3kgf_10X_04					FALSE	FALSE
5	n=2.00_alpha_1600C_5hr_3kgf_10X_05					FALSE	FALSE
6	n=2.00_alpha_1600C_5hr_3kgf_10X_06					FALSE	FALSE
7	n=2.00_alpha_1600C_5hr_3kgf_10X_07					FALSE	FALSE
8	n=2.00_alpha_1600C_5hr_3kgf_10X_08					FALSE	FALSE

Table B-3 Continued

Indent	file name	ah (μm)	av (μm)	2ch (μm)	2cv (μm)	H (GPa)	K (MPa $\sqrt{\text{m}}$)
9	n=2.00_alpha_1600C_5hr_3kgf_10X_09					FALSE	FALSE
10	n=2.00_alpha_1600C_5hr_3kgf_10X_10					FALSE	FALSE
11	n=2.00_alpha_1600C_5hr_3kgf_10X_11	77.7	72.3			9.7	FALSE
12	n=2.00_alpha_1600C_5hr_3kgf_10X_12					FALSE	FALSE
13	n=2.00_alpha_1600C_5hr_3kgf_10X_13					FALSE	FALSE
14	n=2.00_alpha_1600C_5hr_3kgf_10X_14	72.4	67.5			11.2	FALSE
15	n=2.00_alpha_1600C_5hr_3kgf_10X_15	71.3	74.2	154.1	134.0	10.3	4.4
16	n=2.00_alpha_1600C_5hr_3kgf_10X_16	70.7	67.1			11.5	FALSE
17	n=2.00_alpha_1600C_5hr_3kgf_10X_17	77.1	71.9			9.8	FALSE
18	n=2.00_alpha_1600C_5hr_3kgf_10X_18					FALSE	FALSE
19	n=2.00_alpha_1600C_5hr_3kgf_10X_19					FALSE	FALSE
20	n=2.00_alpha_1600C_5hr_3kgf_10X_20					FALSE	FALSE
21	n=2.00_alpha_1600C_5hr_3kgf_10X_21					FALSE	FALSE
22	n=2.00_alpha_1600C_5hr_3kgf_10X_22					FALSE	FALSE
23	n=2.00_alpha_1600C_5hr_3kgf_10X_23					FALSE	FALSE
24	n=2.00_alpha_1600C_5hr_3kgf_10X_24					FALSE	FALSE
25	n=2.00_alpha_1600C_5hr_3kgf_10X_25					FALSE	FALSE
26	n=2.00_alpha_1600C_5hr_3kgf_10X_26					FALSE	FALSE
27	n=2.00_alpha_1600C_5hr_3kgf_10X_27	69.9	58.2	124.5	150.1	13.3	4.8
28	n=2.00_alpha_1600C_5hr_3kgf_10X_28	70.6	68.4	125.2	193.4	11.3	3.8
29	n=2.00_alpha_1600C_5hr_3kgf_10X_29					FALSE	FALSE
30	n=2.00_alpha_1600C_5hr_3kgf_10X_30					FALSE	FALSE
31	n=2.00_alpha_1600C_5hr_3kgf_10X_31					FALSE	FALSE
32	n=2.00_alpha_1600C_5hr_3kgf_10X_32					FALSE	FALSE
33	n=2.00_alpha_1600C_5hr_3kgf_10X_33					FALSE	FALSE
34	n=2.00_alpha_1600C_5hr_3kgf_10X_34					FALSE	FALSE
35	n=2.00_alpha_1600C_5hr_3kgf_10X_35					FALSE	FALSE
36	n=2.00_alpha_1600C_5hr_3kgf_10X_36					FALSE	FALSE
37	n=2.00_alpha_1600C_5hr_3kgf_10X_37					FALSE	FALSE
38	n=2.00_alpha_1600C_5hr_3kgf_10X_38					FALSE	FALSE
39	n=2.00_alpha_1600C_5hr_3kgf_10X_39					FALSE	FALSE
0	n=2.00_alpha_1600C_5hr_3kgf_10X_00	69.1	66.7	144.0	146.1	11.8	4.4
1	n=2.00_alpha_1600C_10hr_3kgf_10X_01					FALSE	FALSE
2	n=2.00_alpha_1600C_10hr_3kgf_10X_02	70.1	73.0			10.7	FALSE
3	n=2.00_alpha_1600C_10hr_3kgf_10X_03	68.3	70.3			11.4	FALSE
4	n=2.00_alpha_1600C_10hr_3kgf_10X_04	70.6	65.6	193.1	151.8	11.8	3.3
5	n=2.00_alpha_1600C_10hr_3kgf_10X_05	65.9	62.0	166.0	147.8	13.4	3.8
6	n=2.00_alpha_1600C_10hr_3kgf_10X_06					FALSE	FALSE
7	n=2.00_alpha_1600C_10hr_3kgf_10X_07					FALSE	FALSE
8	n=2.00_alpha_1600C_10hr_3kgf_10X_08					FALSE	FALSE
9	n=2.00_alpha_1600C_10hr_3kgf_10X_09					FALSE	FALSE
10	n=2.00_alpha_1600C_10hr_3kgf_10X_10	65.2	66.8			12.5	FALSE

Table B-3 Continued

Indent	file name	ah (μm)	av (μm)	2ch (μm)	2cv (μm)	H (GPa)	K (MPa $\sqrt{\text{m}}$)
11	n=2.00_alpha_1600C_10hr_3kgf_10X_11	68.1	68.6			11.7	FALSE
12	n=2.00_alpha_1600C_10hr_3kgf_10X_12	68.0	69.5			11.6	FALSE
13	n=2.00_alpha_1600C_10hr_3kgf_10X_13					FALSE	FALSE
14	n=2.00_alpha_1600C_10hr_3kgf_10X_14					FALSE	FALSE
15	n=2.00_alpha_1600C_10hr_3kgf_10X_15					FALSE	FALSE
16	n=2.00_alpha_1600C_10hr_3kgf_10X_16					FALSE	FALSE
17	n=2.00_alpha_1600C_10hr_3kgf_10X_17	70.2	69.3			11.2	FALSE
18	n=2.00_alpha_1600C_10hr_3kgf_10X_18	69.9	69.8	209.1	186.2	11.2	2.7
19	n=2.00_alpha_1600C_10hr_3kgf_10X_19	71.5	72.7	134.9	183.1	10.5	3.7
20	n=2.00_alpha_1600C_10hr_3kgf_10X_20					FALSE	FALSE
21	n=2.00_alpha_1600C_10hr_3kgf_10X_21					FALSE	FALSE
22	n=2.00_alpha_1600C_10hr_3kgf_10X_22	69.8	70.7	212.8	177.1	11.1	2.7
23	n=2.00_alpha_1600C_10hr_3kgf_10X_23					FALSE	FALSE
24	n=2.00_alpha_1600C_10hr_3kgf_10X_24	67.5	73.7	152.4	145.8	11.0	4.1
25	n=2.00_alpha_1600C_10hr_3kgf_10X_25					FALSE	FALSE
26	n=2.00_alpha_1600C_10hr_3kgf_10X_26	68.5	66.5			12.0	FALSE
27	n=2.00_alpha_1600C_10hr_3kgf_10X_27					FALSE	FALSE
28	n=2.00_alpha_1600C_10hr_3kgf_10X_28					FALSE	FALSE
29	n=2.00_alpha_1600C_10hr_3kgf_10X_29	68.5	66.2	133.0	172.3	12.0	3.9
30	n=2.00_alpha_1600C_10hr_3kgf_10X_30					FALSE	FALSE
31	n=2.00_alpha_1600C_10hr_3kgf_10X_31					FALSE	FALSE
32	n=2.00_alpha_1600C_10hr_3kgf_10X_32					FALSE	FALSE
33	n=2.00_alpha_1600C_10hr_3kgf_10X_33					FALSE	FALSE
34	n=2.00_alpha_1600C_10hr_3kgf_10X_34					FALSE	FALSE
35	n=2.00_alpha_1600C_10hr_3kgf_10X_35					FALSE	FALSE
36	n=2.00_alpha_1600C_10hr_3kgf_10X_36					FALSE	FALSE
37	n=2.00_alpha_1600C_10hr_3kgf_10X_37					FALSE	FALSE
38	n=2.00_alpha_1600C_10hr_3kgf_10X_38					FALSE	FALSE
39	n=2.00_alpha_1600C_10hr_3kgf_10X_39					FALSE	FALSE
40	n=2.00_alpha_1600C_10hr_3kgf_10X_40					FALSE	FALSE
1	n=2.00_alpha_1600C_20hr_3kgf_10X_01					FALSE	FALSE
2	n=2.00_alpha_1600C_20hr_3kgf_10X_02					FALSE	FALSE
3	n=2.00_alpha_1600C_20hr_3kgf_10X_03					FALSE	FALSE
4	n=2.00_alpha_1600C_20hr_3kgf_10X_04					FALSE	FALSE
5	n=2.00_alpha_1600C_20hr_3kgf_10X_05					FALSE	FALSE
6	n=2.00_alpha_1600C_20hr_3kgf_10X_06					FALSE	FALSE
7	n=2.00_alpha_1600C_20hr_3kgf_10X_07					FALSE	FALSE
8	n=2.00_alpha_1600C_20hr_3kgf_10X_08					FALSE	FALSE
9	n=2.00_alpha_1600C_20hr_3kgf_10X_09					FALSE	FALSE
10	n=2.00_alpha_1600C_20hr_3kgf_10X_10					FALSE	FALSE
11	n=2.00_alpha_1600C_20hr_3kgf_10X_11					FALSE	FALSE
12	n=2.00_alpha_1600C_20hr_3kgf_10X_12					FALSE	FALSE

Table B-3 Continued

Indent	file name	ah (μm)	av (μm)	2ch (μm)	2cv (μm)	H (GPa)	K (MPa $\sqrt{\text{m}}$)
13	n=2.00_alpha_1600C_20hr_3kgf_10X_13					FALSE	FALSE
14	n=2.00_alpha_1600C_20hr_3kgf_10X_14	69.6	72.3	177.5	159.3	10.8	3.3
15	n=2.00_alpha_1600C_20hr_3kgf_10X_15					FALSE	FALSE
16	n=2.00_alpha_1600C_20hr_3kgf_10X_16					FALSE	FALSE
17	n=2.00_alpha_1600C_20hr_3kgf_10X_17					FALSE	FALSE
18	n=2.00_alpha_1600C_20hr_3kgf_10X_18	66.4	57.7	159.1	156.0	14.2	3.7
19	n=2.00_alpha_1600C_20hr_3kgf_10X_19					FALSE	FALSE
20	n=2.00_alpha_1600C_20hr_3kgf_10X_20					FALSE	FALSE
21	n=2.00_alpha_1600C_20hr_3kgf_10X_21					FALSE	FALSE
22	n=2.00_alpha_1600C_20hr_3kgf_10X_22					FALSE	FALSE
23	n=2.00_alpha_1600C_20hr_3kgf_10X_23					FALSE	FALSE
24	n=2.00_alpha_1600C_20hr_3kgf_10X_24					FALSE	FALSE
25	n=2.00_alpha_1600C_20hr_3kgf_10X_25	68.3	69.4			11.5	FALSE
26	n=2.00_alpha_1600C_20hr_3kgf_10X_26	66.4	67.8	218.0	147.2	12.1	3.0
27	n=2.00_alpha_1600C_20hr_3kgf_10X_27	67.2	70.8	248.7	141.8	11.5	2.7
28	n=2.00_alpha_1600C_20hr_3kgf_10X_28					FALSE	FALSE
29	n=2.00_alpha_1600C_20hr_3kgf_10X_29					FALSE	FALSE
30	n=2.00_alpha_1600C_20hr_3kgf_10X_30					FALSE	FALSE
31	n=2.00_alpha_1600C_20hr_3kgf_10X_31					FALSE	FALSE
32	n=2.00_alpha_1600C_20hr_3kgf_10X_32					FALSE	FALSE
33	n=2.00_alpha_1600C_20hr_3kgf_10X_33					FALSE	FALSE
34	n=2.00_alpha_1600C_20hr_3kgf_10X_34					FALSE	FALSE
35	n=2.00_alpha_1600C_20hr_3kgf_10X_35					FALSE	FALSE
36	n=2.00_alpha_1600C_20hr_3kgf_10X_36					FALSE	FALSE
37	n=2.00_alpha_1600C_20hr_3kgf_10X_37					FALSE	FALSE
38	n=2.00_alpha_1600C_20hr_3kgf_10X_38					FALSE	FALSE
39	n=2.00_alpha_1600C_20hr_3kgf_10X_39					FALSE	FALSE
40	n=2.00_alpha_1600C_20hr_3kgf_10X_40					FALSE	FALSE
1	n=2.00_gamma_1600C_5hr_3kgf_10X_01	68.5	66.4			12.0	FALSE
2	n=2.00_gamma_1600C_5hr_3kgf_10X_02	70.7	72.3			10.7	FALSE
3	n=2.00_gamma_1600C_5hr_3kgf_10X_03	68.0	68.4			11.7	FALSE
4	n=2.00_gamma_1600C_5hr_3kgf_10X_04					FALSE	FALSE
5	n=2.00_gamma_1600C_5hr_3kgf_10X_05					FALSE	FALSE
6	n=2.00_gamma_1600C_5hr_3kgf_10X_06					FALSE	FALSE
7	n=2.00_gamma_1600C_5hr_3kgf_10X_07					FALSE	FALSE
8	n=2.00_gamma_1600C_5hr_3kgf_10X_08					FALSE	FALSE
9	n=2.00_gamma_1600C_5hr_3kgf_10X_09					FALSE	FALSE
10	n=2.00_gamma_1600C_5hr_3kgf_10X_10					FALSE	FALSE
11	n=2.00_gamma_1600C_5hr_3kgf_10X_11					FALSE	FALSE
12	n=2.00_gamma_1600C_5hr_3kgf_10X_12					FALSE	FALSE
13	n=2.00_gamma_1600C_5hr_3kgf_10X_13					FALSE	FALSE
14	n=2.00_gamma_1600C_5hr_3kgf_10X_14					FALSE	FALSE

Table B-3 Continued

Indent	file name	ah (μm)	av (μm)	2ch (μm)	2cv (μm)	H (GPa)	K (MPa $\sqrt{\text{m}}$)
15	n=2.00_gamma_1600C_5hr_3kgf_10X_15					FALSE	FALSE
16	n=2.00_gamma_1600C_5hr_3kgf_10X_16	67.6	66.5	149.8	187.2	12.1	3.3
17	n=2.00_gamma_1600C_5hr_3kgf_10X_17					FALSE	FALSE
18	n=2.00_gamma_1600C_5hr_3kgf_10X_18	67.1	66.0			12.3	FALSE
19	n=2.00_gamma_1600C_5hr_3kgf_10X_19					FALSE	FALSE
20	n=2.00_gamma_1600C_5hr_3kgf_10X_20					FALSE	FALSE
21	n=2.00_gamma_1600C_5hr_3kgf_10X_21					FALSE	FALSE
22	n=2.00_gamma_1600C_5hr_3kgf_10X_22					FALSE	FALSE
23	n=2.00_gamma_1600C_5hr_3kgf_10X_23	68.1	68.2	170.4	172.6	11.7	3.2
24	n=2.00_gamma_1600C_5hr_3kgf_10X_24					FALSE	FALSE
25	n=2.00_gamma_1600C_5hr_3kgf_10X_25					FALSE	FALSE
26	n=2.00_gamma_1600C_5hr_3kgf_10X_26					FALSE	FALSE
27	n=2.00_gamma_1600C_5hr_3kgf_10X_27					FALSE	FALSE
28	n=2.00_gamma_1600C_5hr_3kgf_10X_28					FALSE	FALSE
29	n=2.00_gamma_1600C_5hr_3kgf_10X_29					FALSE	FALSE
30	n=2.00_gamma_1600C_5hr_3kgf_10X_30					FALSE	FALSE
31	n=2.00_gamma_1600C_5hr_3kgf_10X_31					FALSE	FALSE
32	n=2.00_gamma_1600C_5hr_3kgf_10X_32	70.4	69.3	184.7	170.7	11.2	3.0
33	n=2.00_gamma_1600C_5hr_3kgf_10X_33					FALSE	FALSE
34	n=2.00_gamma_1600C_5hr_3kgf_10X_34					FALSE	FALSE
35	n=2.00_gamma_1600C_5hr_3kgf_10X_35					FALSE	FALSE
36	n=2.00_gamma_1600C_5hr_3kgf_10X_36					FALSE	FALSE
37	n=2.00_gamma_1600C_5hr_3kgf_10X_37					FALSE	FALSE
38	n=2.00_gamma_1600C_5hr_3kgf_10X_38					FALSE	FALSE
39	n=2.00_gamma_1600C_5hr_3kgf_10X_39	68.0	68.5	172.5	139.0	11.7	3.7
40	n=2.00_gamma_1600C_5hr_3kgf_10X_40					FALSE	FALSE
10	n=2.00_alpha_1600C_30hr_3kgf_10X_10	68.5	73.4			10.8	FALSE
11	n=2.00_alpha_1600C_30hr_3kgf_10X_11					FALSE	FALSE
12	n=2.00_alpha_1600C_30hr_3kgf_10X_12					FALSE	FALSE
13	n=2.00_alpha_1600C_30hr_3kgf_10X_13	66.7	71.4			11.4	FALSE
14	n=2.00_alpha_1600C_30hr_3kgf_10X_14	67.7	70.3	193.7	167.1	11.5	3.1
15	n=2.00_alpha_1600C_30hr_3kgf_10X_15					FALSE	FALSE
16	n=2.00_alpha_1600C_30hr_3kgf_10X_16	68.1	69.9			11.5	FALSE
17	n=2.00_alpha_1600C_30hr_3kgf_10X_17	71.8	72.6			10.5	FALSE
18	n=2.00_alpha_1600C_30hr_3kgf_10X_18					FALSE	FALSE
19	n=2.00_alpha_1600C_30hr_3kgf_10X_19					FALSE	FALSE
20	n=2.00_alpha_1600C_30hr_3kgf_10X_20	74.2	71.7	190.1	143.3	10.2	3.5
21	n=2.00_alpha_1600C_30hr_3kgf_10X_21					FALSE	FALSE
22	n=2.00_alpha_1600C_30hr_3kgf_10X_22	68.8	72.8			10.9	FALSE
23	n=2.00_alpha_1600C_30hr_3kgf_10X_23	69.1	71.4			11.1	FALSE
24	n=2.00_alpha_1600C_30hr_3kgf_10X_24	69.4	70.0			11.2	FALSE
25	n=2.00_alpha_1600C_30hr_3kgf_10X_25					FALSE	FALSE

Table B-3 Continued

Indent	file name	ah (μm)	av (μm)	2ch (μm)	2cv (μm)	H (GPa)	K (MPa $\sqrt{\text{m}}$)
26	n=2.00_alpha_1600C_30hr_3kgf_10X_26	71.4	73.8	182.9	175.8	10.4	3.2
27	n=2.00_alpha_1600C_30hr_3kgf_10X_27	70.2	73.0			10.7	FALSE
28	n=2.00_alpha_1600C_30hr_3kgf_10X_28					FALSE	FALSE
29	n=2.00_alpha_1600C_30hr_3kgf_10X_29					FALSE	FALSE
30	n=2.00_alpha_1600C_30hr_3kgf_10X_30					FALSE	FALSE
31	n=2.00_alpha_1600C_30hr_3kgf_10X_31					FALSE	FALSE
32	n=2.00_alpha_1600C_30hr_3kgf_10X_32	66.2	68.5	188.6	215.5	12.0	2.7
33	n=2.00_alpha_1600C_30hr_3kgf_10X_33	69.8	70.3	186.0	187.4	11.1	3.0
34	n=2.00_alpha_1600C_30hr_3kgf_10X_34					FALSE	FALSE
35	n=2.00_alpha_1600C_30hr_3kgf_10X_35					FALSE	FALSE
36	n=2.00_alpha_1600C_30hr_3kgf_10X_36					FALSE	FALSE
37	n=2.00_alpha_1600C_30hr_3kgf_10X_37	67.8	67.4	226.3	189.8	11.9	2.5
38	n=2.00_alpha_1600C_30hr_3kgf_10X_38					FALSE	FALSE
39	n=2.00_alpha_1600C_30hr_3kgf_10X_39					FALSE	FALSE
40	n=2.00_alpha_1600C_30hr_3kgf_10X_40					FALSE	FALSE
41	n=2.00_alpha_1600C_30hr_3kgf_10X_41					FALSE	FALSE
42	n=2.00_alpha_1600C_30hr_3kgf_10X_42					FALSE	FALSE
43	n=2.00_alpha_1600C_30hr_3kgf_10X_43					FALSE	FALSE
44	n=2.00_alpha_1600C_30hr_3kgf_10X_44					FALSE	FALSE
45	n=2.00_alpha_1600C_30hr_3kgf_10X_45					FALSE	FALSE
46	n=2.00_alpha_1600C_30hr_3kgf_10X_46					FALSE	FALSE
47	n=2.00_alpha_1600C_30hr_3kgf_10X_47					FALSE	FALSE
48	n=2.00_alpha_1600C_30hr_3kgf_10X_48					FALSE	FALSE
49	n=2.00_alpha_1600C_30hr_3kgf_10X_49					FALSE	FALSE
50	n=2.00_alpha_1600C_30hr_3kgf_10X_50					FALSE	FALSE
0	n=2_1650_3kgf_10X_00	70.5	69.1	261.7	197.7	11.2	2.2
1	n=2_1650_3kgf_10X_01	68.3	68.8			11.6	FALSE
2	n=2_1650_3kgf_10X_02	68.2	66.4			12.0	FALSE
3	n=2_1650_3kgf_10X_03					FALSE	FALSE
4	n=2_1650_3kgf_10X_04					FALSE	FALSE
5	n=2_1650_3kgf_10X_05	69.8	67.9	274.7	210.8	11.5	2.0
6	n=2_1650_3kgf_10X_06	69.3	68.9	250.6	153.6	11.4	2.6
7	n=2_1650_3kgf_10X_07					FALSE	FALSE
8	n=2_1650_3kgf_10X_08	69.1	69.4			11.4	FALSE
9	n=2_1650_3kgf_10X_09					FALSE	FALSE
10	n=2_1650_3kgf_10X_10					FALSE	FALSE
11	n=2_1650_3kgf_10X_11					FALSE	FALSE
12	n=2_1650_3kgf_10X_12					FALSE	FALSE
13	n=2_1650_3kgf_10X_13					FALSE	FALSE
14	n=2_1650_3kgf_10X_14					FALSE	FALSE
15	n=2_1650_3kgf_10X_15					FALSE	FALSE
16	n=2_1650_3kgf_10X_16	74.5	71.7	258.5	164.3	10.2	2.5

Table B-3 Continued

Indent	file name	ah (μm)	av (μm)	2ch (μm)	2cv (μm)	H (GPa)	K (MPa $\sqrt{\text{m}}$)
17	n=2_1650_3kgf_10X_17					FALSE	FALSE
18	n=2_1650_3kgf_10X_18					FALSE	FALSE
19	n=2_1650_3kgf_10X_19					FALSE	FALSE
20	n=2_1650_3kgf_10X_20					FALSE	FALSE
21	n=2_1650_3kgf_10X_21	73.5	70.9	245.4	224.2	10.5	2.1
22	n=2_1650_3kgf_10X_22					FALSE	FALSE
23	n=2_1650_3kgf_10X_23					FALSE	FALSE
24	n=2_1650_3kgf_10X_24					FALSE	FALSE
25	n=2_1650_3kgf_10X_25					FALSE	FALSE
26	n=2_1650_3kgf_10X_26					FALSE	FALSE
27	n=2_1650_3kgf_10X_27					FALSE	FALSE
28	n=2_1650_3kgf_10X_28	72.8	72.1			10.4	FALSE
29	n=2_1650_3kgf_10X_29	68.7	69.2	178.1	208.7	11.5	2.8
30	n=2_1650_3kgf_10X_30					FALSE	FALSE
31	n=2_1650_3kgf_10X_31					FALSE	FALSE
32	n=2_1650_3kgf_10X_32					FALSE	FALSE
33	n=2_1650_3kgf_10X_33					FALSE	FALSE
34	n=2_1650_3kgf_10X_34	73.1	72.1			10.4	FALSE
35	n=2_1650_3kgf_10X_35					FALSE	FALSE
36	n=2_1650_3kgf_10X_36					FALSE	FALSE
37	n=2_1650_3kgf_10X_37					FALSE	FALSE
38	n=2_1650_3kgf_10X_38					FALSE	FALSE
39	n=2_1650_3kgf_10X_39	69.1	70.2			11.3	FALSE
40	n=2_1650_3kgf_10X_40					FALSE	FALSE
41	n=2_1650_3kgf_10X_41					FALSE	FALSE
42	n=2_1650_3kgf_10X_42					FALSE	FALSE
43	n=2_1650_3kgf_10X_43	67.6	68.5			11.8	FALSE
44	n=2_1650_3kgf_10X_44					FALSE	FALSE
45	n=2_1650_3kgf_10X_45	69.1	70.5			11.2	FALSE
46	n=2_1650_3kgf_10X_46					FALSE	FALSE
47	n=2_1650_3kgf_10X_47					FALSE	FALSE
48	n=2_1650_3kgf_10X_48					FALSE	FALSE
49	n=2_1650_3kgf_10X_49					FALSE	FALSE
0	n=2_1700_3kgf_10X_01					FALSE	FALSE
1	n=2_1700_3kgf_10X_02					FALSE	FALSE
2	n=2_1700_3kgf_10X_03					FALSE	FALSE
3	n=2_1700_3kgf_10X_04					FALSE	FALSE
4	n=2_1700_3kgf_10X_05					FALSE	FALSE
5	n=2_1700_3kgf_10X_06	67.3	68.4	202.2	197.7	11.9	2.6
6	n=2_1700_3kgf_10X_07					FALSE	FALSE
7	n=2_1700_3kgf_10X_08	69.4	71.3			11.0	FALSE
8	n=2_1700_3kgf_10X_09					FALSE	FALSE

Table B-3 Continued

Indent	file name	ah (μm)	av (μm)	2ch (μm)	2cv (μm)	H (GPa)	K (MPa $\sqrt{\text{m}}$)
9	n=2_1700_3kgf_10X_10	67.1	69.1			11.8	FALSE
10	n=2_1700_3kgf_10X_11	70.5	73.6	229.6	182.2	10.5	2.5
11	n=2_1700_3kgf_10X_12	70.9	69.7			11.0	FALSE
12	n=2_1700_3kgf_10X_13					FALSE	FALSE
13	n=2_1700_3kgf_10X_14	69.4	70.1			11.2	FALSE
14	n=2_1700_3kgf_10X_15	68.2	68.2	211.8	184.8	11.7	2.6
15	n=2_1700_3kgf_10X_16					FALSE	FALSE
16	n=2_1700_3kgf_10X_17	68.3	69.4			11.5	FALSE
17	n=2_1700_3kgf_10X_18	72.4	72.5			10.4	FALSE
18	n=2_1700_3kgf_10X_19					FALSE	FALSE
19	n=2_1700_3kgf_10X_20					FALSE	FALSE
20	n=2_1700_3kgf_10X_21					FALSE	FALSE
21	n=2_1700_3kgf_10X_22					FALSE	FALSE
22	n=2_1700_3kgf_10X_23					FALSE	FALSE
23	n=2_1700_3kgf_10X_24					FALSE	FALSE
24	n=2_1700_3kgf_10X_25	70.2	68.8	217.2	162.5	11.3	2.8
25	n=2_1700_3kgf_10X_26					FALSE	FALSE
26	n=2_1700_3kgf_10X_27					FALSE	FALSE
27	n=2_1700_3kgf_10X_28	75.0	74.3	280.6	223.0	9.8	1.8
28	n=2_1700_3kgf_10X_29					FALSE	FALSE
29	n=2_1700_3kgf_10X_30					FALSE	FALSE
30	n=2_1700_3kgf_10X_31					FALSE	FALSE
31	n=2_1700_3kgf_10X_32					FALSE	FALSE
32	n=2_1700_3kgf_10X_33					FALSE	FALSE
33	n=2_1700_3kgf_10X_34	69.4	72.2	241.9	226.9	10.9	2.0
34	n=2_1700_3kgf_10X_35					FALSE	FALSE
35	n=2_1700_3kgf_10X_36					FALSE	FALSE
36	n=2_1700_3kgf_10X_37					FALSE	FALSE
37	n=2_1700_3kgf_10X_38					FALSE	FALSE
38	n=2_1700_3kgf_10X_39	71.8	69.9	260.7	287.8	10.9	1.6